SANDIA REPORT
SAND2008-6355
Unlimited Release
September, 2008

Interface Physics in Microporous Media: LDRD Final Report

David R. Noble, Chad E. Knutson, Carlton F. Brooks, Ken S. Chen, Melissa A. Yaklin, Alicia R. Aragon, Yihong Liu, Laura J. Pyrak-Nolte and Nicholas J. Giordano

Prepared by
Sandia National Laboratories
Albuquerque, New Mexico 87185 and Livermore, California 94550

Sandia is a multiprogram laboratory operated by Sandia Corporation,
a Lockheed Martin Company, for the United States Department of Energy's
National Nuclear Security Administration under Contract DE-AC04-94AL85000.

Issued by Sandia National Laboratories, operated for the United States Department of Energy by Sandia Corporation.

Available to DOE and DOE contractors from
U.S. Department of Energy
Office of Scientific and Technical Information
P.O. Box 62
Oak Ridge, TN 37831

Telephone: (865) 576-8401
Facsimile: (865) 576-5728
E-Mail: reports@adonis.osti.gov
Online ordering: http://www.osti.gov/bridge

Available to the public from
U.S. Department of Commerce
National Technical Information Service
5285 Port Royal Rd.
Springfield, VA 22161

Telephone: (800) 553-6847
Facsimile: (703) 605-6900
E-Mail: orders@ntis.fedworld.gov
Online order: http://www.ntis.gov/help/ordermethods.asp?loc=7-4-0#online

SAND2008-6355
Unlimited Release
Printed September 2008

Interface Physics in Microporous Media: LDRD Final Report

David R. Noble, Chad E. Knutson
Thermal Fluid Processes

Carlton F. Brooks
Microscale Science and Technology

Ken S. Chen
Nanoscale and Reactive Processes

Melissa A. Yaklin
Fuels and Energy Transitions

Alicia R. Aragon
Geomechanics

Sandia National Laboratories
P.O. Box 5800
Albuquerque, New Mexico 87185-MS0836

Yihong Liu, Laura J. Pyrak-Nolte and Nicholas J. Giordano
Purdue University
Department of Physics
525 Northwestern Avenue
West Lafayette, Indiana 47907-2036 USA

Abstract

This document contains a summary of the work performed under the LDRD project entitled "Interface Physics in Microporous Media". The presence of fluid-fluid interfaces, which can carry non-zero stresses, distinguishes multiphase flows from more readily understood single-phase flows. In this work the physics active at these interfaces has been examined via a combined experimental and computational approach. One of the major difficulties of examining true microporous systems of the type found in filters, membranes, geologic media, etc. is the geometric uncertainty. To help facilitate the examination of transport at the pore-scale without this

complication, a significant effort has been made in the area of fabrication of both two-dimensional and three-dimensional micromodels. Using these micromodels, multiphase flow experiments have been performed for liquid-liquid and liquid-gas systems. Laser scanning confocal microscopy has been utilized to provide high resolution, three-dimensional reconstructions as well as time resolved, two-dimensional reconstructions. Computational work has focused on extending lattice Boltzmann (LB) and finite element methods for probing the interface physics at the pore scale. A new LB technique has been developed that provides over 100x speed up for steady flows in complex geometries. A new LB model has been developed that allows for arbitrary density ratios, which has been a significant obstacle in applying LB to air-water flows. A new reduced order model has been developed and implemented in finite element code for examining non-equilibrium wetting in microchannel systems. These advances will enhance Sandia's ability to quantitatively probe the rich interfacial physics present in microporous systems.

ACKNOWLEDGMENTS

We would like to acknowledge the contributions of Joanne Fredrich who proposed this project and stewarded it during her time at Sandia. We would also like to acknowledge the work of both Mike Hickner and David Holdych who contributed to this work while at Sandia. We would also like to thank Raymond O. Cote for fabricating the cartridge for the micromodels and Brian Wroblewski and David J. Saiz for performing the photolithography work.

CONTENTS

FIGURES

TABLES

NOMENCLATURE

2PP	two-photon polymerization
ALE	Arbitrary Lagrangian-Eulerian
CDFEM	Conformal Decomposition Finite Element Method
CLSM	Confocal Laser Scanning Microscopy
DOE	Department of Energy
FEM	Finite Element Method
GBL	gamma butyrolactone
IAV	interfacial area per volume
LB	Lattice Boltzmann
LBGK	Lattice BGK (Bhatnager-Gross-Krook)
LS	Level Set
MEMS	micro-electrical mechanical systems
PDMS	Polydimethylsiloxane
PECVD	plasma enhanced chemical vapor deposition
SAMS	self-assembled monolayers
SNL	Sandia National Laboratories
TPA	Two-Photon Absorption
UV	ultraviolet
VOF	volume-of-fluid
WTC	Washington Technology Center

1. INTRODUCTION

1.1. Motivation

A fundamental understanding of multiphase transport through microporous media is central to many problems in the chemical, earth, engineering, and biological sciences. These include oil, gas and water production in the geosciences, ground water protection and contamination remediation in environmental science, chemical mixing and processing in chemical engineering, and in porous tissue applications of biology and bioengineering, among others. The presence of fluid-fluid interfaces, that can carry non-zero stresses, distinguishes multiphase flows from more readily understood single-phase flows. In multiphase systems, the fluid-fluid and fluid-solid interface geometries have a primary effect on the macroscopic system behavior. Conventional treatments of multiphase flow that are premised upon specification of phase saturation ignore the pore-scale fluid dynamics and consequently fail to predict macroscopic behavior.

1.2. Technical Approach

We have developed and applied novel experimental techniques including multi-channel laser scanning microscopy, micro- and nano-tomography, and two-photon lithographic fabrication techniques to examine the interfacial physics of three-dimensional multiphase flows in microporous systems. The experimental program has been complemented by the development of new Lattice Boltzmann (LB) and Finite Element Method (FEM) simulation methods that implement sharp interface technology developed in the context of level set methods. This synergistic development of advanced experimental and numerical simulation capabilities has significantly enhanced Sandia's ability to quantitatively predict multiphase flows in microporous media that are dominated by interfacial physics. Considerable progress has been made in each of the areas of micromodel fabrication, microscale, multiphase flow visualization, and pore-scale multiphase flow simulations via LB and FEM as described in the remainder of this report. A summary of the project accomplishments is given in the next section. The remaining chapters give more details about the accomplishments.

1.3. Summary of Accomplishments

1.3.1. Micromodel Fabrication Accomplishments

The focus of this work has been to develop the technology needed to fabricate three-dimensional (3D) micromodels of microporous media. Team members at the Department of Physics at Purdue University (Professors Laura Pyrak-Nolte and Nick Giordano) have developed techniques for fabricating both 2D and 3D micromodels. This work is discussed in detail in chapter 2 of this report. Noteworthy accomplishments include:

- 2D micromodel fabrication (FY 06). Two-dimensional (2D) micromodels were fabricated using projection photolithography for Sandia. Three micromodels were fabricated, each with complex geometrical features, for modeling single phase flow, miscible fluid flow, and multiphase flow.

- 3D micromodel demonstration (FY 06). Demonstration of proof-of-concept for fabricating 3D micromodels using a Two-Photon Absorption (TPA) technique was performed in a campus user facility. Based on success of demonstration, a dedicated TPA system was designed for this project and initial testing performed. Issues that arose from the initial testing were (1) establishing exposure times, beam widths and laser power for control and reproducibility of grain shape, (2) accurately locating the focal point that determines location of written feature, and (3) sealing of 3D micromodels for fluid displacement experiments.
- 3D micromodel fabrication development (FY07). The two-photon absorption (TPA) system was re-designed to address the technical issues that arose in FY06. The objective lens was replaced with a new objective that has a larger entrance pupil for capturing a larger portion of the laser beam. A single expander lens is used to expand the beam to fill the entrance pupil to reduce the beam waist on the focal plane. A confocal alignment system was added to the system to determine the focal point of the laser beam on the sample, ensuring attachment of the exposed volumes to the glass support. In the confocal alignment path, a beam splitter sends a portion of the beam that is reflected from the sample through a confocal pinhole to a photodetector. Partial reflections from the interfaces of the sample (top photoresist surface, photoresist-glass interface, and bottom glass surface) produce maximum photocurrent in the alignment photodetector when the interfaces are at the focal plane of the objective lens. This confocal alignment arm and protocol has increased the yield of device fabrication nearly to 100%.
- 3D micromodel fabrication theory development and validation (FY07-FY08). A theoretical study of the exposure volume in the photo-resist was performed to determine the laser parameters that control exposure volumes that form the walls of the flow structure. This analysis enabled the reproducibility of exposure volumes and control of the exposure volume shape, again contributing to nearly 100% device yield. Numerous experiments were performed to quantify the experimental performance of the TPA system based on the theoretical study. Individual grains as well as walls were made with the TPA system using different beam widths, exposure times, laser power, etc. The resulting grains and walls were characterized to determine the exposure volumes and write times.
- Microchannel fabrication (FY07-FY08). Several microchannel structures were fabricated and sent to Sandia for imaging with laser confocal microscopy. A protocol for sealing 2D channels as well as 3D micromodels was developed.

1.3.2. Microporous, Multiphase Flow Visualization Accomplishments

In FY07 Sandia team members Mike Hickner (6338) worked with post-doc Alicia Aragon (6316) on the visualization of multiphase flow in microchannels using laser scanning confocal microscopy. In FY08 this responsibility was assumed by Carlton Brooks (1513) and Melissa Yaklin (6338). Their work fabricating micromodels for microchannel studies is discussed in detail in chapter 3. The transient, two phase flow experiments using these micromodels are discussed in chapter 4. Noteworthy accomplishments in the area include:

- Two phase gas-liquid flows in a microchannel (FY07). Two-phase flow in rectangular microchannels with dimensions of approximately 80μm wide and 40μm high were

imaged using laser scanning confocal microscopy. Due to the long collection times (minutes to hours) for acquiring 3D data, the confocal images are collected at pseudo-steady state where the interface between the fluids appears at rest.

- Two-phase liquid-liquid flows in a microchannel (FY07). Decane-water flows were imaged in a slightly more complicated microchannel geometry. In this instance, the micromodel was originally saturated with decane and then imbibed sequentially with water. In Figures 1.1-1.2, the decane is shown as the green phase, while the water appears as the purple phase. This visualization shows that even under the conditions of very slow imbibition, there are still places where the decane phase appears trapped by the imbibed water phase. The 3D rendering in Figure 1.2 allows the flow morphology, such as curvature of interfaces, to be investigated in more detail.
- Transient microchannel imbibition imaging (FY08). Laser scanning confocal microscopy has been employed for real time imaging of the imbibition process in microchannel geometries. Scanning rates limit these images to 2D slices centered along the midplane of the microchannels. Comparisons have been made with the finite element modeling results to help in the development and implementation of wetting line models for multiphase flow in micropores.

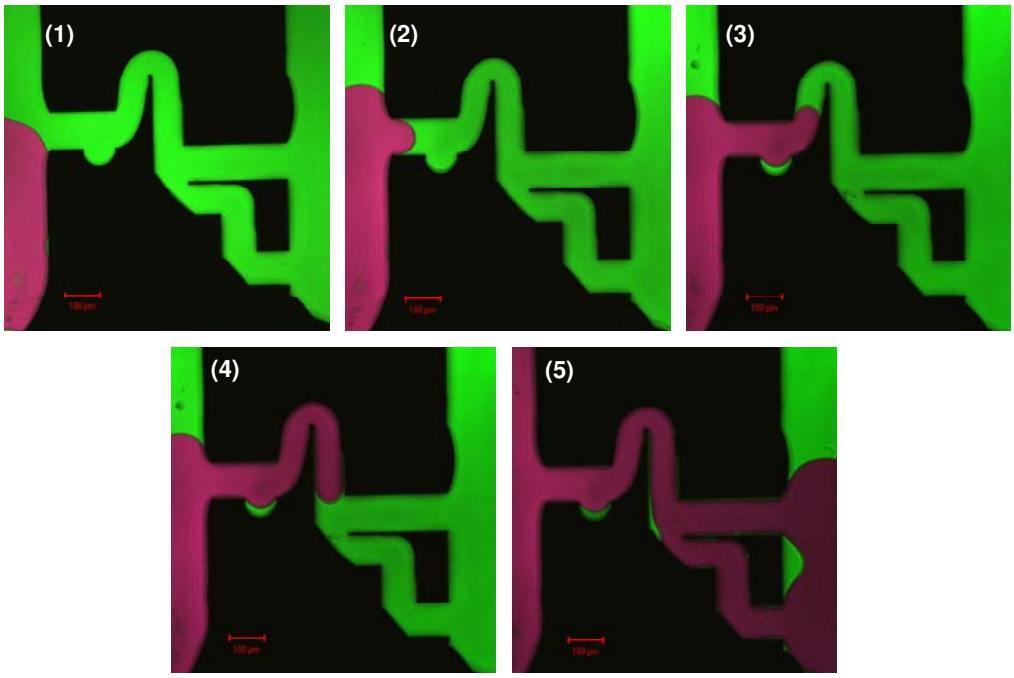

Figure 1.1. 2D rendering of water-decane two-phase flow in microchannels. Water is depicted as the purple phase and decane is the green phase.

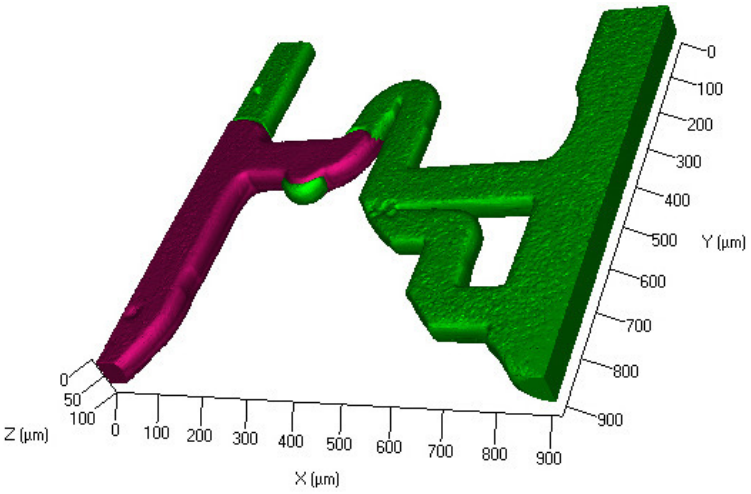

Figure 1.2. 3D rendering of water-decane imbibed microchannel.

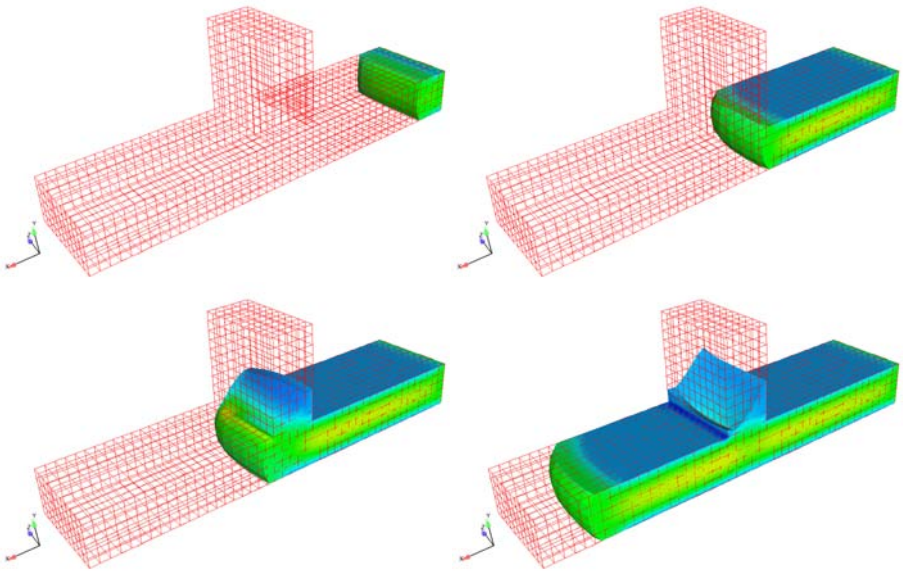

Figure 1.3. ARIA simulation results for imbibition of a viscous liquid into an initially air-filled microchannel. Color indicates the magnitude of the streamwise velocity.

1.3.3. Finite Element Modeling Accomplishments

Ken Chen (1516) has worked with Carlton Brooks (1513) to verify finite element simulations of a drop wetting a surface. This work is presented in chapter 5. David Noble (1514) has worked with Chad Knutson (1514) to advance Sandia simulation capabilities of multiphase flow in microporous geometries using finite element methods. A new reduced order model has been developed for non-equilibrium wetting in microchannels. This work is presented in chapter 6. Noteworthy accomplishments in this area include:

- Simulations of 3D microchannel flows using FEM (FY07). SIERRA code ARIA was used to simulate the imbibition of a highly viscous fluid into an initially air-filled microchannel. The results of one simulation are shown in Figure 1.3. Ongoing comparisons with experiments show that quantitative agreement is only possible if the wetting line motion is correctly captured. This is a challenge because the continuum transport equations are not respected along this wetting line.
- Simulations of 3D microchannel flows using a reduced order model via FEM (FY08). A 2D model has been developed for simulating flow in thin geometries. This model accounts for the non-equilibrium effects according to the Blake wetting model. By avoiding the cost of simulating the full 3D flow, the cost is reduced significantly. The model has been validated against theory and compared against experimental results. The model has been shown to capture the critical phenomena in thin microchannels. This work has suggested possible methods to design microchannel experiments that are able to accurately measure the wetting properties of a system that cannot be readily measured using a macroscopic apparatus.
- Verification of dynamic wetting of an axisymmetric drop (FY08). Careful comparisons have been made between finite element simulation predictions and those predicted by the Blake wetting model. This work has shown the need for enhanced level set renormalization methods for quantitative simulations of wetting for fluids that exhibit static contact angles significantly different than 90˚.

1.3.4. Lattice Boltzmann Modeling Accomplishments

In the original LDRD proposal, we planned to use lattice Boltzmann methods (LB) for the multiphase flow simulations. However, LB lacked the constitutive flexibility to model these fluids of interest to Sandia. Therefore the finite element methods described above were pursued. Nonetheless significant enhancements to LB were developed in the first two years of this work. Sandia Principle Investigator David Noble (1514) has worked with post-docs, David Holdych (1513) and Chad Knutson (1514), to advance Sandia simulation capabilities of multiphase flow in microporous geometries using lattice Boltzmann (LB) methods. The work on steady LB methods is presented in detail in chapter 7. The work on sharp interface LB methods is presented in chapter 8. Noteworthy accomplishments include:

- 100x speedup for steady LB simulations of single phase-flow (FY06). While typical LB formulations operate by evolving the flow in time, there is no apparent reason why this approach should be taken in solving steady flows. Instead we have developed a much more efficient technique based on Newton's method for solving the system of nonlinear equations. The linear system of equations that are formed at each Newton iteration is solved using a general direct solver designed for sparse, banded matrices. The cost of the simulations is shown to scale super-linearly with the number of unknowns as compared to quadratically for the standard LB scheme. These results show that the time-steady LB equations can be solved efficiently using a "black box" direct solver. These methods are applicable to arbitrary geometries, in contrast to the nested mesh requirement of multigrid solvers used previously. Thus, standard linear solver packages may be employed to

improve the efficiency of time-steady LB simulations by multiple orders of magnitude. For the specific case of Stokes flow with resolution 251x251, the method performs more than 100 times faster than a standard implementation, which involves evolving the fully explicit algorithm to steady-state.

- Embedding arbitrary strength discontinuities in LB (FY07). The accuracy of LB models substantially degrades when the scale of the interface width approaches that of pore throat widths through which the interface passes. Additionally, the density ratio for the two fluids is rather limited, so that accurate modeling of water and air, for example, is not possible. In FY07, we developed an approach to capture sharp interfaces between fluids with unbounded density ratios using techniques motivated by the ghost fluid method for finite difference models. This issue of sharp interface capturing in LB is critical if the method is to provide a predictive capability for multiphase flows in micropores.

The experimental discoveries in this work, combined with algorithm development, significantly advance our ability to model interfacial physics in microporous media. This will enable us to provide critical help to our customers in areas ranging from energy with applications in enhanced oil recovery and fuel cell development, to water resources requiring advanced filtration technology, and to weapons systems in need of reliable encapsulation techniques for weapons components.

2. TWO-DIMENSIONAL & THREE DIMENSIONAL MICROMODELS: EXPERIMENTAL STUDY OF FABRICATION AND IMAGING INTERFACIAL GEOMETRY

This chapter describes the work by Purdue collaborators, Yihong Liu, Laura J. Pyrak-Nolte and Nicholas J. Giordano, to produce reliable two-dimensional and three-dimensional micromodels.

2.1. Motivation

In light of the crucial importance of multiple fluids in porous media, it is surprising that current research relies on theoretical work that has seen little improvement over 150 years. In 1856, Henri Darcy [1] developed an empirical law for single-phase flow in a porous medium. A common form of Darcy's law is

$$q = -\frac{kA\Delta P}{\mu L} \qquad (2.1)$$

where q is the volumetric flow rate for a system of length L and cross-sectional area A, ΔP is the pressure difference across the system of length L, μ is the fluid viscosity, and k is the permeability which is a property of the medium. Since its original derivation, Darcy's law has been used in various extended forms to describe the flow of multiple immiscible fluid phases and applied to problems in diverse fields. Traditionally, Darcy's flow equation for the multiphase case is written for each fluid phase in terms of fluid phase pressures and fluid saturations as

$$q_i = -\frac{kk_{ir}}{\mu_i}\nabla p_i \qquad (2.2)$$

where the subscript i denotes a particular fluid phase (e.g., gas or oil), q_i is the flux of the i^{th} phase, ∇p_i is the pressure gradient of phase i, and μ_i is its viscosity. The parameter k is the permeability and depends only on the properties of the porous medium, while k_{ir} is the relative permeability of the i^{th} phase and is assumed to be function of only the volume fraction occupied by that phase (this fraction is also known as the saturation S_i). For the two-phase case, two constitutive equations are used to couple the flow equations for each phase. One of the constitutive equations relates the pressure contrast between the fluid phases to saturation [2]:

$$p_n - p_w = p_c = f(S) \qquad (2.3)$$

where p_c is the capillary pressure, p_w is the wetting phase pressure, and p_n is the nonwetting phase pressure. The other constitutive equation relates the relative permeability of a phase to the saturation of the phase. Saturation of each phase is the parameter that is common to both

constitutive relations. While these constitutive equations are very appealing, such descriptions of multiphase flow are not based on fundamental fluid dynamics, and are known to fail in many cases [3-6].

The failure of this and other extensions of Darcy's Law to multiple phases indicates that knowledge of the saturation of each phase is not sufficient to describe the state of the system. While several investigators [7-15] have recognized that an accurate description of multiphase flow in a porous medium must account for the thermodynamics and the geometry of the interfaces between the fluids (and between the fluids and the solid phase), these are properties that have eluded direct experimental measurement. Interfaces are hard to measure in a porous medium because they represent microscopic features at a small scale and usually are hidden from view. The physics of the interfaces enters as an interfacial area per volume (IAV), which when combined with capillary pressure and saturation is hypothesized [4] to lead to a unique description of the thermodynamic energy state. If this approach is correct, the hysteretic relationship universally observed between capillary pressure and saturation for equilibrium conditions should be a unique and invertible relationship when IAV is included as a third variable.

The theoretical motivation for including IAV in the capillary pressure - saturation relationship is based on the way capillary pressures are defined on the pore scale and how they relate to the macroscale measurements of capillary pressures and saturations. On the pore scale, capillary pressure between a wetting phase fluid and a non-wetting phase fluid is given by

$$p_c = \gamma^{wn}\left(\frac{1}{R_1} + \frac{1}{R_2}\right) = \gamma^{wn} J \qquad (2.4)$$

where γ^{wn} is the interfacial tension between the wetting and non-wetting phase and J is the mean curvature of the interfaces based on the principal radii of curvature of the surface, R_1 and R_2. This definition shows how p_c depends on the geometry of the interfaces. Capillary pressure at equilibrium p_{ceq} can also be defined as a balance of forces between the fluids on either side of the interfaces and is defined as

$$p_{ceq} = p_n - p_w \quad . \qquad (2.5)$$

The equation for p_{ceq} is generally assumed to be applicable on the macroscale (core or field scale) as long as p_{ceq} is taken to be a function of the wetting phase saturation, S_w. However, as mentioned earlier, it has been shown by numerous experimental investigations that p_{ceq} has a hysteretic relationship with saturation [6, 16]. Experiments have shown that the capillary pressure - saturation relationship depends on the drainage and imbibition history of the system and is not single valued. Hence, capillary pressure cannot be determined simply from saturation or vice-versa.

Muccino et al. [4] hypothesized that the capillary pressure - saturation relationship is a two-dimensional projection of a more extensive functional dependence, i.e., a third variable is needed to explicitly define the state of the system. They pointed out that the IAV is a parameter that includes the distribution of the fluid phases within the system. For any porous system with wetting and non-wetting phases, three interfacial areas can be defined: between the two fluid phases and between each fluid phase and the solid.

Interfacial areas per volume provide natural descriptions of fundamental physical processes in porous media. For instance, thermodynamic energies are proportional to interfacial areas, and interfacial areas per volume represent a form of energy density. Gradients in energy densities define the dynamical pressures that drive the movement and distribution of phases within a complex topology. Interfacial areas per volume in a porous medium therefore contain information involving a three-dimensional potential energy landscape.

Interfacial areas per volume also provide a natural yardstick for defining the role of scale in multiphase fluid properties. The dimensional unit of IAV is a spatial frequency (inverse length) that breaks scale invariance. Therefore, the interfacial areas between phases define a length scale. Whenever a physical system has an intrinsic length scale, the physics of the system can be divided into two regimes: one where sample sizes are larger than the intrinsic length scale, and the other where information is obtained on scales smaller than the intrinsic length scale. Breaking scale invariance makes it possible to define representative elementary volumes and to apply averaging theorems. Combining the averaging theorems with thermodynamics further constrains the possible types of constitutive equations that can rigorously describe multiphase fluid properties in porous media.

Large values of IAV relate to a finely distributed phase that can block pore throats and seriously affect permeability, while small values of IAV relate to gross separations of phases, with large connected volumes of the phase that can flow unimpeded through the network. Significant numerical studies have been performed to explore the relationships between capillary pressure, saturation and interfacial area. Reeves and Celia [15] developed a numerical model that scans over repetitive imbibition and drainage while tracking the interfacial area for each loop. These studies pointed to a non-unique relationship between interfacial area and partial saturation, although a family of curves did emerge that lies within a localized part of the parameter space defined by area and saturation.

As a consequence of this theoretical framework, it is important to measure and validate, experimentally, whether or not IAV is an essential parameter for describing the energy state of multiple fluids in porous media. IAV is difficult to measure on natural systems, i.e. rock and soil. Measuring pore-scale and sub-pore-scale features requires measurement techniques that can probe interfacial area and pore geometry from the length scale of the pore to the length scale of a representative volume of the porous medium. Experimental methods that have been used to acquire measurements of IAV on natural and synthetic samples include synchrotron-based x-ray micro-tomography [17-19], photoluminescent volumetric imaging [20] and interfacial tracers [21-30].

Previously, we used transparent two-dimensional micromodels and optical imaging with a CCD camera to quantify fluid and interfacial distributions to investigate the robustness of capillary pressure calculations from interfacial information. The admitted disadvantage of using micromodels is that they are inherently two-dimensional systems and the optical images did not provide direct imaging of the entire fluid-fluid interface, i.e. the hidden curvature could not be imaged. In this section, we describe the work performed under this project to obtain direct three-dimensional imaging of the pore space and fluid distributions within two-dimensional micromodels and the development of a two-photon adsorption approach for creating transparent three-dimensional porous systems.

2.2. Experimental Procedure

2.2.1. Sample Preparation

In previous studies [31-34], optical projection and contact lithography on positive photoresist were used to create two-dimensional micromodels. In this work, a pore-structure pattern is transferred under vis-UV (ultraviolet) illumination from a transparent mask to a photosensitive polymer layer called a photoresist ("positive resist") that coats a substrate. The thickness of the photoresist layer determines the depth of the flow channels. When a region of the photoresist is exposed to a sufficiently large integrated intensity of blue light, a photochemical reaction within the photoresist makes the region soluble in a developer solution. The unexposed photoresist is not soluble, so after development the photoresist layer contains a negative image of the original light pattern. Cheng et al. [31] and Chen et al. [35] used Shipley photoresist types 1805 and 1827 with their standard developer [36]. Their micromodels were fabricated with pore networks covering a 600 µm x 600 µm area and the depth of the pores (flow channels) ranged between 1 µm to 2 µm. A general review of two-dimensional micromodels is given in Giordano and Cheng [37].

For this study, we explored the use of SU-8 (a negative resist) and MA-P1275hv (positive resist) for the fabrication of micromodels using a two-photon polymerization (2PP) approach. These two photoresists differ from that used in our previous studies [31-34] in that these resists enable fabrication of micro-fluidic structures that range in thickness from 2 µm to 3 mm. For our study, the thickness of the resist was chosen to range between 20 µm to 40 µm to be compatible with the limitations of the laser confocal microscopy system.

2.2.1.1. SU-8 Sample Preparation

2.2.1.1.1. *Description of SU-8*

Most of the fabricated micromodels for this project were made using the negative photoresist Nano SU-8 (Microchem Co.) to obtain large micro-fluidic flow structures. This type of photoresist is widely used in the fabrication of micro-electrical mechanical systems (MEMS). SU-8 epoxy is multifunctional glycidyl ether derivative of bisphenol-A novolac from Shell Commercial's EPON SU-8 resin [38]. Since there are 8 epoxy groups in each molecule, thus a high aromatic functionality of 8, the resist has high cross-linking performance, allows high-aspect ratio, improves side wall straightness, and improves chemical thermal resistance [39].

Furthermore, because SU-8 has a low molecular weight around 7000, it dissolves in a variety of organic solvents resulting in less developer induced pattern swelling, and thus high resolution [38, 40]. A 190 μm diameter post was reported by Lee et al. in 2004 [41]. Plus, the absorption in the near-UV spectrum is very low so that the light can penetrate thick photoresist layers and thus be used for thick-film applications [42]. A 500 μm thick layer and an aspect ratio of 50:1 were reported by Teh et al. in 2005 [43].

SU-8 epoxy is dissolved in gamma butyrolactone (GBL) to adjust the viscosity and achieve different film thickness ranges. Less GBL and more SU-8 results in higher viscosity and thicker film range, e.g. SU-8/GBL = 7:3, thickness = 30-200 μm; SU-8/GBL = 6:4, thickness = 5-25 μm; with spin speeds from 1000-4000 rpm [44]. The third component is a photoinitiator, triaryl sulfonium salt in propylene carbonate solvent. Under UV exposure, this salt generates catalyzed acid which helps open the ring and gain much higher cross linking efficiency. During the subsequent baking, the photogenerated acid diffuses in the photoresist and catalyzes the cross linking. Because the uncrosslinked resist has low molecular weight, the unexposed resist can be removed by a nonpolar solvent, forming a negative image. The difference of the solubility between the exposed and unexposed resists determines the pattern resolution [40].

2.2.1.1.2. *Micromodel Fabrication Procedure*

2.2.1.1.2.1. Cleaning the Substrates

The micromodels are formed on substrate. The substrates were Corning Square No. 2 cover glass, 190 μm to 250 μm thick. For most studies, 18x18 mm cover slips were used except for the large 2D patterns that were fabricated on the 25x25 mm cover slips (section 2.1.2). Before coating the photoresist onto a cover glass, the cover slip was cleaned in an ultrasonic cleaner (Branson 1510). A plastic sample holder was designed and fabricated to hold 7 cover slips. The holder was placed in a beaker with a fluid and then subsequently placed in the ultrasonic bath. The substrates were cleaned in three steps: (1) in DI water for 5 min, (2) in acetone for 5 min, and (3) in isopropyl alcohol for 5 min. After cleaning, the sample holder is kept in the isopropyl alcohol in a beaker.

2.2.1.1.2.2. Spin Coating

Before spin coating, the cover slip is removed from the isopropyl alcohol with tweezers and dried with nitrogen at 138 kPa. After drying the surface, the substrate is placed on a spinner and a vacuum is used to fix the substrate position. SU-8_50 (Microchem Co.) was used for fabricating samples with thickness from 30 μm to 100 μm. Because SU-8_50 has a high viscosity, a syringe cannot be used to apply the photoresist to the substrate. Instead, a wooden stick is used to apply two drops of SU-8 onto the 18x18 mm cover slip and three drops onto the 25x25 mm cover slips. The photoresist is allowed to spread across the surface for approximately 10 sec. The substrate is then spun at a speed of 3000 rpm to create a 40 μm thick layer or spun with a speed of 3500 rpm to create a 30 μm layer. During spinning, small bubbles may remain on the substrate surface and lower the sample quality. Thus, care is taken during the application of the SU-8 to avoid bubble formation as much as possible to fabricate uniform thin layers. After spinning, the samples remain on a flat surface for approximately 30 min to reduce edge

effects, i.e. non-uniform thickness of the layer on the edge. Edge effects can be significant because of the small sample size of the cover slip compared to size of silicon waffles. We found that letting the samples equilibrate on a flat surface for 30 min before soft baking can reduce edge effects and make the photoresist layer uniform and flat.

2.2.1.1.2.3. Soft Baking

Soft baking is performed to evaporate the solvent and to densify the photoresist layer. A two-step baking procedure is recommended by the manufacturer. The company's data sheet recommends baking the 40 μm layer at 65°C for 5 min and at 95°C for 15 min on the hot plate. The initial low temperature results in a more uniform evaporation of the solvent. From experimentation, the soft bake times were increased to 15 min at 65°C and 30 min at 95°C because a convection oven was used instead of a hot plate. A glass Petri dish provides a smooth, flat surface for the samples during baking. An uneven baking surface results in a non-uniform thickness of the photoresist which affects the sealing of the sample. After baking, the temperature is decreased to the room temperature in 10 min. The gradual decrease in temperature helps avoid stress-induced damage to the sample.

2.2.1.1.2.4. Exposure

SU-8 is a negative photoresist and is insensitive to wavelengths above 400 nm but highly absorptive under 350 nm. SU-8 is optimized for near-UV exposure from 350 nm to 400 nm. For two-photon exposure (described in section 2.2) the laser is adjusted to a central wavelength of 790 nm. The sample is exposed in two steps: (1) with a femtosecond laser, to expose the desired structure in the center of the sample; and (2) with a UV lamp, to expose the inlet and outlet regions for fluid flow experiments. For step (1), the sample is placed on the XYZ motion stage and the stage is moved to direct-write the desired pattern into the photoresist layer on the sample. The exposure position and speed are set by computer.

2.2.1.1.2.4.1. *Two Photon Exposure*

The theoretical and experimental details associated with two-photon adsorption are described in Section 2.2.2. The experimental procedure for performing two-photon exposure includes tasks associated with alignment, interface detection and motion control.

The sample is placed on a motion-controlled XYZ stage that moves the sample under the laser. Before two-photon exposure with the laser, the stage is leveled to ensure that the depth of the laser-writing is consistent with the expanse of the sample. Over a 5 mm travel length, the error is approximately 2 μm in the z-direction. The details of the alignment are described in the optics section. After leveling the XYZ stage, the exposure position is set to lie in the channel between the inlet and outlet reservoirs. The inlet and outlet reservoirs are fabricated using an UV exposure mask and broad illumination method that are described in the next section. The exposure position is found by first finding the edge of the cover glass in the x- and y-directions. Then, the two-photon exposure area is shifted from the edge 8.5 mm to 9.2 mm in the x-direction and 8.5 mm to 9.4 mm in the y-direction. An exposure area of 700 μm x 900 μm in the center of the sample matches the channel area of UV exposure mask. Because SU-8 is a negative

photoresist (i.e., exposed regions remain), development occurs after all exposures, i.e., the exposure areas and channel are matched blindly.

2.2.1.1.2.4.2. *UV Broad Illumination*

Following the two-photon exposure, UV broad illumination is used to fabricate the 3 mm x 3 mm inlet and outlet ports and a 900 µm wide channel connecting the two ports. The mask is shown in Figure 2.1. The substrate and the mask are placed in a chamber and a vacuum is used to keep the mask tightly attached to the photoresist surface on the substrate. The mask is carefully aligned to the right and lower edges of the substrate to match the two-photon exposure area. After a 15 min warm-up, an UV lamp is used for 20 seconds for the 40 µm thick layer, and 15 seconds for the 30 µm layer.

2.2.1.1.2.5. Post Exposure Baking

After exposure, the photoresist is baked for 10 min at 65°C and then for 15min at 95°C to cross-link the SU-8. A two-step post-exposure bake is recommended by the manufacturer to minimize stress and prevent cracking. The sample is gradually cooled to room temperature after baking to avoid additional thermal stress. After cross-linking, the exposed flow pattern in the resist can be observed.

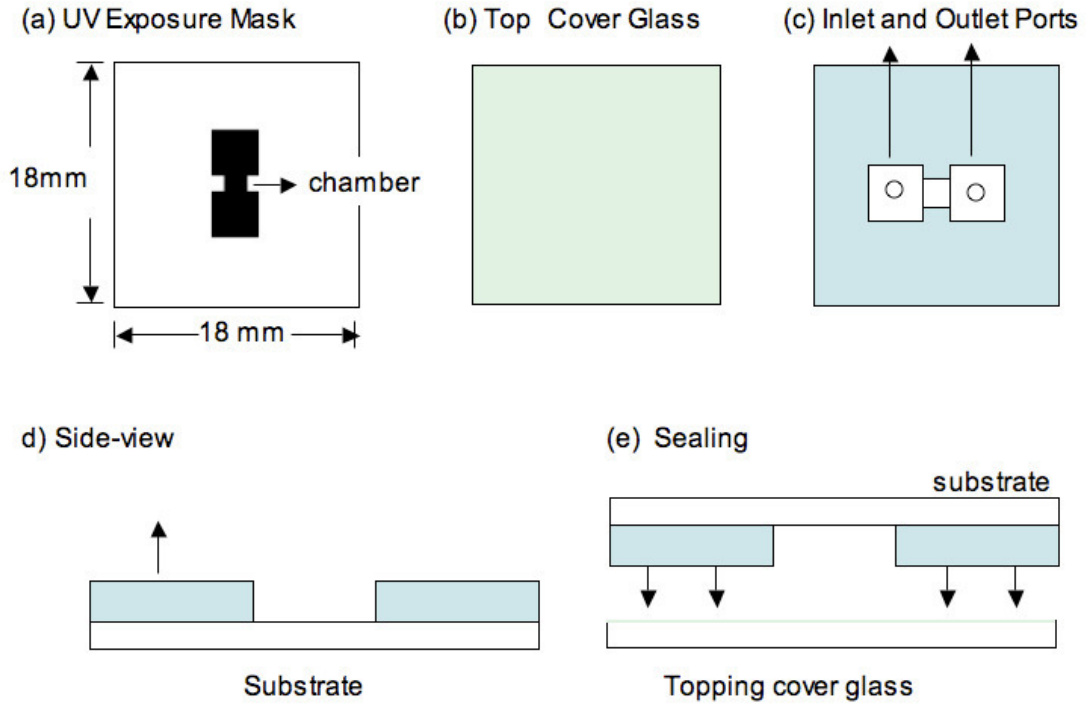

Figure 2.1. SU-8 Fabrication Procedure: a) The UV exposure mask; b) The top cover glass with a 5 µm thin layer of SU-8_5; c) The bottom substrate with 40 µm thick layer of SU-8 and with the location of the inlet and outlet ports; d) The side view of the substrate; e) Sealing the sample.

2.2.1.1.2.6. Fluid Ports

For flow testing, two holes with the diameter of 0.5715 mm (0.0225 in, #74 drill bits) are drilled in the inlet and outlet regions on the substrate before development. The locations of the holes are shown in Figure 2.1. The holes are drilled from the glass side to the photoresist side to reduce the influence of glass dust on the exposed pattern. Care is taken during drilling to achieve smooth ports without cracking the glass. The photoresist that is drilled off is removed during the development process because the SU-8 in the areas of the inlet and outlet is unexposed.

2.2.1.1.2.7. Develop and Rinse

The drilled sample is developed in a commercial developer (Microchem) for 6 min, rinsed in isopropyl alcohol, and then placed on a flat surface to dry. The samples are not blow dried to avoid destruction of the micro structures. The samples are not hard baked because SU-8 has good mechanical properties.

2.2.1.1.2.8. Sealing

The final step in the sample preparation is sealing of the sample for immiscible displacement experiments.

2.2.1.1.2.8.1. *Top Cover Slip*

The sample is sealed using a cover slip with the same dimensions as the substrate. The top cover slip is subjected to the same cleaning procedure as the substrate. After cleaning, a thin layer of SU-8 is spun onto the top cover slip. SU-8_5 is good for fabricating 5 μm to 15 μm thick layers because it has a low viscosity compared to SU-8_50. A 6 ml syringe is used to apply 5 drops of SU-8_5 onto the cover slip during spinning. A 5 μm thick layer is formed on the top cover slip by using a spin rate of 3000 rpm for 60 seconds.

2.2.1.1.2.8.2. *Sealing on the Hot Plate*

Immediately after spin coating the top cover slip, sealing is performed using a hot plate. Two hot plates are used. One hot plate is used to heat the developed substrate to 95°C while the spin coating process is performed on the top cover slip. The second hot plate is set to 65°C and is used to evaporate the solvent from the 5 μm thick layer of SU-8_5 on the cover slip and to densify the layer. This is achieved by placing the cover slip on the 65°C surface for 1 min. The top cover slip is then moved to the 95°C surface. The developed substrate is placed carefully on the top cover slip with the SU-8_5 photoresist facing down as shown in Figure 2.1e. A small force is applied to the top cover slip with a cotton stick to improve bonding between the two surfaces. After baking at 95°C for 3 min, the sealed sample is removed from the hot plate. After cooling down for 5 min, the sample is observed under an optical microscope to determine the quality of the bond (i.e., gaps in the bonded surface that might cause leaks) and the integrity of the flow channels (i.e., no blocking by rogue photoresist). Leaking and blockage of flow channels are two common problems in the sealing procedure. The light pressure from the cotton stick is used to prevent leaking around the borders of the channel. If too much pressure is

applied, the photoresist from the cover slip flows into the channel and blocks the flow channels. From experimental testing, a slight modification to the sealing procedure produced slightly better yields. The modification requires that the cover slip is placed on the 95°C hot plate with the SU-8_5 layer facing upward. Then the developed substrate (flow structure facing downward) is gently pressed onto the top cover slip. This method was found to reduce the blockage of flow channels.

Leakage and blockage are the two main causes of low yield of micromodel samples. More viscous photoresist reduces the occurrence of blockage but makes it more difficult to seal. This conflict makes it hard to improve the sealing step. Thus, another method for sealing the samples was also tested. The second technique uses a clear tape (Hampton Research ClearSeal Film) that is often used to fashion micromodels. The clear tape can be used for optical microscopic imaging and strongly attaches to the photoresist SU-8, but the tape's surface is not compatible with some organic solvents, i.e. the tape dissolves.

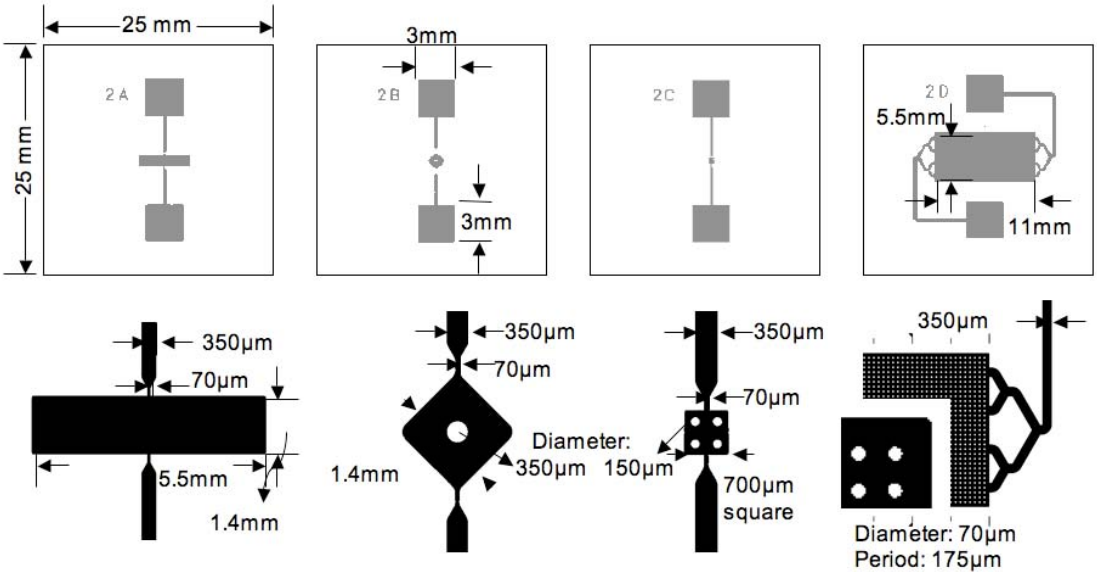

Figure 2.2. Sandia sample masks. All the masks are for 25 mm x 25 mm cover slips. The inlet and outlet are both 3 mm x 3 mm.

2.2.1.1.3. *Fabrication of Micromodels for Fluid Mixing Experiments*

The fluid mixing experiments described in other sections in this report used micromodels fabricated using SU-8. The masks are shown in Figure 2.2. These fluid structures differed from those described above in that the flow channels were longer and required a larger substrate and cover slip. The large patterned 2D samples were fabricated on 25 mm x 25 mm cover glass. The sample preparation is similar to that described above with the exceptions that the channel depth is 30 µm and all surfaces of the flow channel are composed of SU-8. In the smaller samples, the walls of the flow channel were developed and baked SU-8_50, the bottom surface of the channel was glass and the upper surface was either undeveloped but heated SU-8_5 or the clear tape. The large patterns were designed to ensure that all four surfaces of a channel had the same surface properties, i.e., the same material was used. To achieve this, a 5 µm thin layer of SU-8_5

was spun on at 3000 rpm for 30 seconds and soft baked at 65°C (for 5 min) and 95°C (for 10 min). This layer was exposed to the UV lamp for 5 seconds and then baked at 65°C (for 5 min) and 95°C (for 15 min). This thin layer is fabricated as the bottom of the channel. The layer that forms the flow channel was fabricated by spin coating the thin layer with SU-8_50 at 3500 rpm for 30 seconds which creates the 30 µm thick channel layer. For the 30 µm layer, the soft baking time was reduced to 15 min at 65°C and 25 min at 95°C. The post exposure baking times were reduced to 5 min at 65°C and 10 min at 95°C. All exposures were performed using the UV broad spectral exposure because no 3D micro-structures were required.

The large 2D patterns were also difficult to seal. Although the channels are wide enough that blockage does not occur, problems arose with SU-8 attaching to the channel walls and solidifying. When this occurs, the walls of the channel were no longer straight as shown in Figure 2.3.

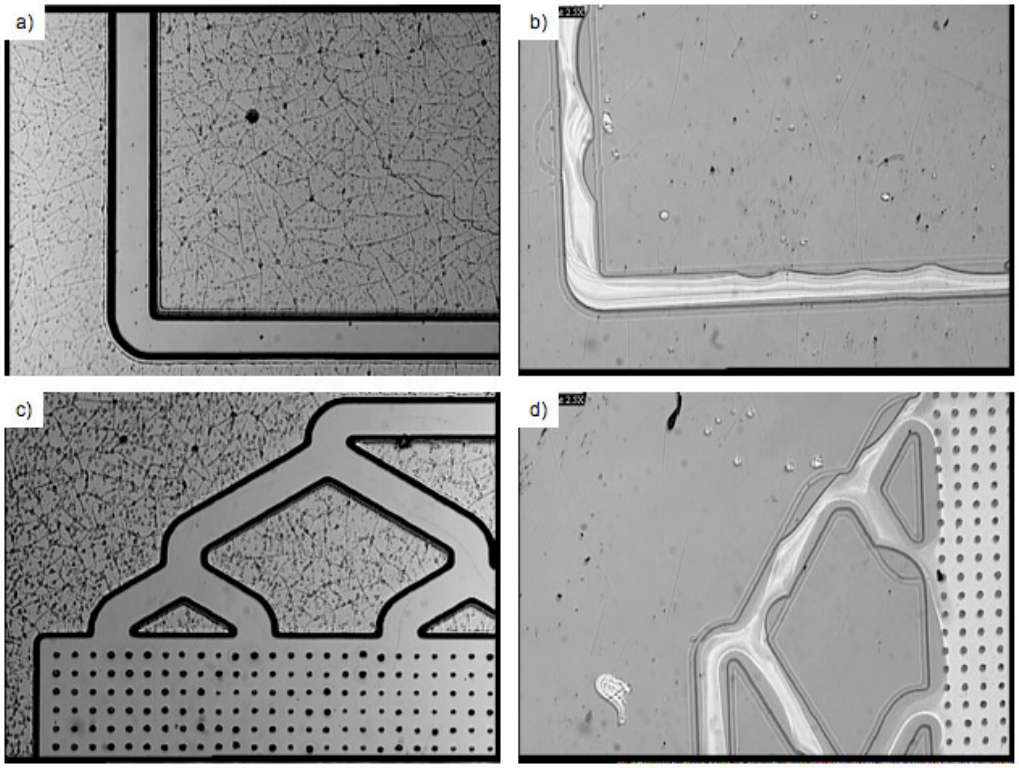

Figure 2.3. Two examples of the channels blocked by SU-8 caused by sealing. Images of before (a & c) and after (b & d) are shown. The photoresist flowed into the channel, solidified on the channel's side wall, and affected the straightness of the wall.

2.2.1.2. Micromodel Fabrication using Ma_P 1275hv

During the final months of the project, we explored the use of a "positive" resist for fabricating micromodels. Ma_P 1275hv is a positive photoresist and differs from negative resist SU-8 in that the exposed portions of Ma_P 1275hv are washed away during development. The advantage of a positive resist is that only the pores or channels of the flow structure need to be exposed either through broad illumination or using the two-photon adsorption approach. Our work using SU-8 (negative resist) found that fabrication of any intricate pattern in 2D or 3D would require

significant write time using the two-photon adsorption approach to write the wall of the pore structure. Thus only simple 2D and 3D structures were fabricated.

At the initiation of the project, a thick (20 μm to 100 μm) positive resist was not commercially readily available. The first "positive resist" was developed by Azoplate Co. in 1962 to avoid swelling the developed pattern in negative resists. Before the epoxy based negative resist, e.g. SU-8, was introduced, the cross linking efficiency decided by the molecular weight difference between the exposed and unexposed resist was low which caused the swelling problem. However, unlike negative resist, the positive resist depends on the molecular polarity change to achieve differential solubility. The basic components of the positive resist are an excellent film-former phenolic-based resin and a solution inhibitor diazoketone derivative. The diazoketone derivative converts to ketenes via Wolff arrangement catalyzed by light and the ketenes react with ambient water to yield carboxylic acid derivatives. Thus the exposed area becomes soluble to alkaline solutions, e.g. aqueous tetra-ammonium hydroxide. Plus, the diazoketone derivatives inhibit the solubility of the phenolic resin in unexposed area [40, 45-47].

Positive resist Ma_P 1275hv was developed from diazo-type photoresist by Micro Resist Technology Corp. The thickness range is from 10 μm to 50 μm with single coating and the exposure dosage is from 300 mJ/cm^2 to 3500 mJ/cm^2 at 365 nm depending on the thickness. Opposite to SU-8, the exposed area will be developed away by 2.38% Tetramethyl-ammonium hydroxide, which makes it convenient to fabricate micro channels or pore structures. Ma_P 1275hv is also sensitive to near-UV spectra (i-line 365 nm and g-line 436 nm) and can be exposed with the same UV lamp as used for SU-8. From experiments, we found that Ma-P 1275hv can be exposed using two-photon exposure by a femtosecond laser. The Ma_P 1275hv sample preparation has similar steps as those of SU-8 described above. After substrate cleaning, we bake the cover slips at 180°C for 20 min to improve the surface properties.

The few fabrications performed on Ma_P 1275hv found that it is potentially a better choice for fabricating 3D micro-structures because only the flow channels are written versus the walls of the channel. This would significantly decrease the laser write time because the porosity of natural systems is typically in the range of 20% of the bulk volume.

2.2.2. Two-Photon Adsorption Approach

2PP initiators for three-dimensional optical data storage and microfabrication are based on two-photon adsorption that depends quadratically on the intensity of light [48-55]. By tightly focusing the writing beam, the absorption is confined at the focus to a volume on the order of the cube of the wavelength of the laser. Thus polymerization (i.e., exposure of the photoresist) is localized in a small volume. In this section, we describe the optical experimental set-up and theoretical constraints of the two-photon approach.

2.2.2.1. Optical Set-Up

The optical setup for the 2PP system to create three-dimensional micromodels is shown in Figure 2.4. The light source is a femtosecond oscillator (Clark-MXR Ninja-4) pumped by a continuous-wave diode-pumped solid-state laser (Coherent Verdi-5) with high power stability ±1% and low

noise <0.03% rms. The pump laser power is 4 Watts with a wavelength of 532 nm. The 2.25 mm diameter beam is introduced into the tunable mode-locked Ti:Sapphire laser through beam steering optics to pump the Ti:Sapphire laser crystal, and a prism pair is used for dispersion compensation. The femtosecond pulse duration is 100 fs, the repetition rate is 100 MHz, and the pulse energy is up to 3.5 nJ/pulse. The center wavelength is adjusted to 790 nm because the photoresist SU-8 is optimized for 350 nm to 400 nm (near-UV) exposure at single-photon absorption, i.e., 700 nm to 800 nm at two-photon absorption. The laser operates most effectively at a wavelength of 800 nm. The half maximum full-width of the frequency spectrum is 36 nm.

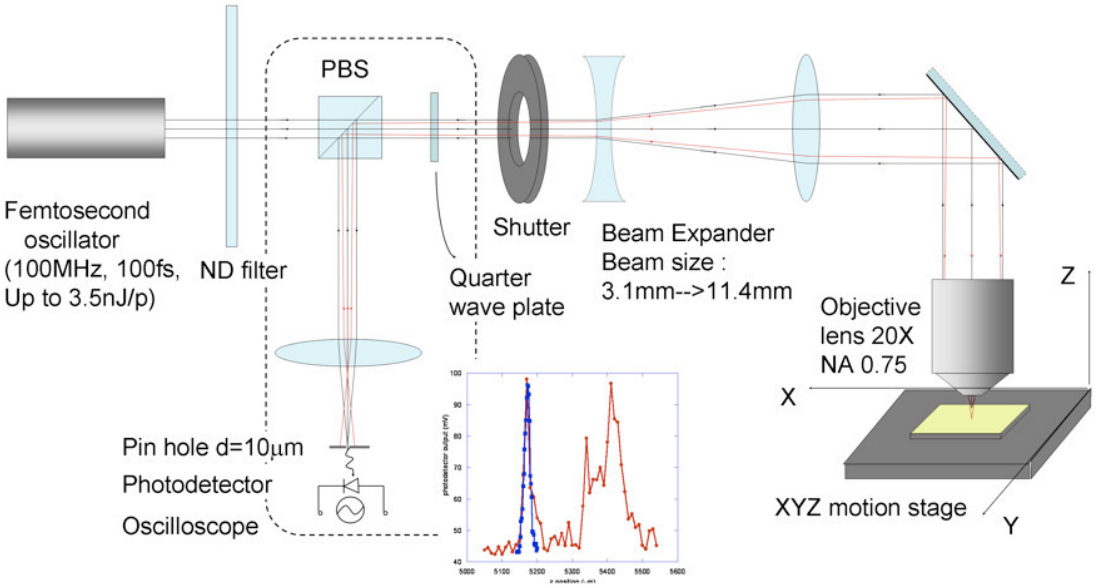

Figure 2.4. The experimental setup for using two-photon polymerization (2PP) to create three-dimensional micromodels. The 100 MHz, 790 nm central wavelength mode-locked femtosecond laser pulses are focused through a 20X, 0.75 NA, objective lens into the SU-8 sample on a XYZ motion stage. The small graph shows the signal output of the photodetector for adjusting the stage level.

The femtosecond pulses are focused through a 20X, 0.75 NA objective lens into the photoresist SU-8 which sits on a XYZ motion-controlled stage. The x and y stages have a minimum increment of 50 nm (Newport Actuator LTA-HL) and 200 nm for the z direction stage (Newport CMA-12CCCL). The motion of the stages is computer-controlled. The main optical path includes a neutral density filter (Circular Variable Metallic Neutral Density Filter) that attenuates the average beam power (optical density gradient 0.05~1), a shutter that sets the exposure time, and a beam expander composed of a concave lens (f=-50mm) and a convex lens (f=150mm) to expand the beam diameter. The average power and exposure time determine the exposed volume. Small focal spot radius caused by the expanded beam determines small height-to-width ratio of the exposure shape. In a branch path we constructed a confocal system to locate the photoresist surface and to determine the z coordinates of the exposure position. Based on the system parameters, the confocal pinhole diameter is half of the Airy unit approximately 10 μm. The pinhole is located behind a convex lens with focal length 50 mm and immediately in front of the photodetector (Thorlabs DET110). A quarter wave plate and a polarization beam splitter are also employed to direct the reflected light to the photodetector to collect and to prevent the reflected light from returning to the laser cavity.

Before exposing a sample, the levelness of the system is checked to ensure that the focal depth is at the same Z coordinate for different X and Y coordinates. First, the Z coordinates of the photoresist surface at the four corners of the sample are determined by using the confocal system. The distance between two corners is 7 mm. Second; the stage is adjusted so all four z coordinates are the same. For each position, only the stage in the z direction is moved with a step length of 10 μm for a total of 50 steps. At each point, the output of the photodetector is recorded. The photoresist surface is determined from a graph of the detector signal plotted against the vertical position z. The procedure is repeated with 2 μm/step and 30 steps to refine the location of the Z coordinate.

2.2.2.2. Theoretical Model and Simulation

We used 2PP to fabricate 2D and 3D microporous structures. The two-photon transition rate is defined by

$$R_{if}^{(2)} = \left| \sum_m \frac{\mu_{fm}\mu_{mi}E^2}{\hbar^2(\omega_{mi}-\omega)} \right|^2 2\pi\rho_f(\omega_{fi}=2\omega) \qquad (2.6)$$

where $\rho_f(\omega_{fi}=2\omega)$ is the density of final state excited by photons of energy $\hbar\omega$, and μ_{fi} is the transition dipole moment. The transition rate varies as $R \propto E^4 \propto I^2$ where I is the light intensity. Thus, the 2PP rate is proportional to the square of the intensity. The rate is also proportional to the duration that the photoresist is exposed by the femtosecond pulses. Therefore, the condition for 2PP is

$$I^2\beta\tau\upsilon t \geq F_{th} \qquad (2.7)$$

where F_{th} is the 2PP threshold of SU-8, I is the peak intensity, β is a constant, τ is the pulse duration, υ is the repetition rate, and t is the exposure time. The intensity profile is Gaussian

$$I(r,z) = I(z)e^{-2(\frac{r}{w(z)})^2} \qquad (2.8)$$

$$I(z) = \frac{2P}{\pi w(z)^2} \qquad (2.9)$$

where $w(z)$ is the spot radius at the z plane and P is the average power. At the focal plane

$$I(r) = I_0 e^{-2(\frac{r}{w_0})^2} \qquad (2.10)$$

where w_0 is focal spot radius and $I_0 = I\ (z=0)$. Substituting the intensity in Eq. (2.7) by the Gaussian profile yields

$$d = w_0\sqrt{\ln(\frac{I_0^2 t}{C_{th}})} \tag{2.11}$$

$$C_{th} = \frac{F_{th}}{\beta\tau\upsilon} \tag{2.12}$$

where d is the diameter of the exposure dose at the focal plane. Considering a Gaussian profile again, the height of the exposed region is

$$H = \frac{2z}{n} = \frac{2z_R}{n}\sqrt{\exp(\frac{1}{2}(\frac{d}{w_0})^2) - 1} \tag{2.13}$$

where $z_R = \pi w_0^2 / \lambda$ is the Rayleigh range and n is the refractive index of SU-8. Because the stage speed is inversely proportional to the exposure time, combining Eq. (2.9) and Eq. (2.11), gives

$$w_{wall} = w_0\sqrt{\ln(\frac{4P^2}{\pi^2 w_0^2 C_{th}^{'} v})} \tag{2.14}$$

$$C_{th}^{'} = \frac{F_{th}^{'}}{\beta\tau\upsilon} \tag{2.15}$$

where w_{wall} is the width of the wall, v is the stage speed, and $C_{th}^{'}$ is a constant.

From Eq. (2.11), (2.13), and (2.14), the width and height of the exposed region is related to the light intensity, exposure time, and the focal spot radius. Smaller exposed volumes are obtained by lowering the intensity and shortening the exposure time. In addition, larger focal spot radiuses produce low ratio of the height-to-width. Therefore, we use the beam expander shown in Figure 2.4 to reduce the focal spot radius and the height-to-width ratio of the exposed region. Without the beam expander, the focal spot radius is 8 μm and the aspect ratio is approximately 30. Adding the beam expander reduces the focal spot radius to 4 μm and the height-to-width ratio to 10. To measure the focal spot radius, we use a very sharp blade cutting the beam in the focal plane, measure the power difference, and fit it with the Gaussian profile to acquire the focal spot radius. The focal spot radiuses in X and Y are measured separately and the mean value is used in our study.

Figure 2.5 shows the simulated axial view with different focal spots according to the equations above. A custom MatLab program was used to draw contours of the same intensity square to show the axial view of the exposure doses. The focal spot of the left graph is 8 μm and that of the right is 4 μm. We can see obvious difference in the aspect ratio so when we fabricate 3D structures, we add the beam expander into the optical system to achieve a small focal spot size and a large width-to-height ratio.

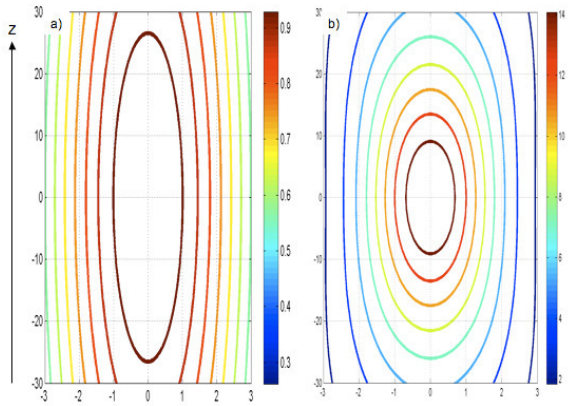

Figure 2.5. Simulations of the axial view of the exposure dose. The scale ratio of the vertical axis, Z-axis, to the horizontal axis is 10:1. The focal spot radiuses are (left) 8 µm and (right) 4 µm.

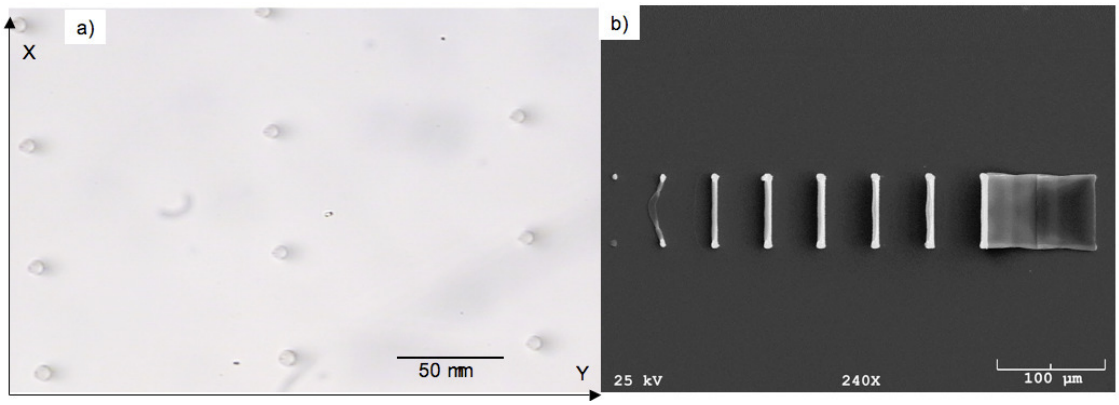

Figure 2.6. a) The optical micrograph of posts at the magnification of 40x exposed at 300 mW and 50 ms. The focal depth became shallower from left to right in the Y direction and remained the same in the X direction; b) The SEM image of straight walls for the wall width measurement as a function of average power and exposure speed (average power 40 mW, speed 20 µm/s, and magnification 240X, and wall length 80 µm).

2.2.2.3. Calibration

With the goal of fabricating microfluidic structures, we started by exposing posts and walls under different experimental conditions and fit the width with the theoretical model. Figure 2.6 shows an example of exposed posts and walls. An optical micrograph of the posts at magnification 40X is shown in Figure 2.6a, and a SEM image of the walls at magnification 240X is shown in Figure 2.6b. The posts or walls were exposed at different focal depths. If the focal depth is deep, the exposure volume is completely buried in the glass, and no photoresist is exposed. On the other hand, if the focal depth is too shallow, the posts or walls do not attach to the substrate, and no structure is left after the development. Thus, a focal depth must be chosen to ensure that the posts and walls attach to the substrate.

In our calibration experiments, we exposed posts and walls at different focal depths. The experimental design is shown in Figure 2.7. We exposed wall by wall in the Y direction with a step length of 50 µm, with the walls oriented in the X direction. As the exposed position Y

varied, the focus position in the Z direction was made deeper from right to left (Figure 2.7) using 3 μm/step. As shown in Figure 2.6b, the wall on the left is focused the deepest in the photoresist and is barely visible on the substrate. The first two walls on the right fell onto the substrate because the focal depths were too shallow for these two walls to remain standing on the cover glass after development. The focal depths of the posts were also changed by stepping in the Y direction and held constant in the X direction. The step lengths for the posts were 100 μm/step along the Y-axis and 1 μm/step along the X-axis.

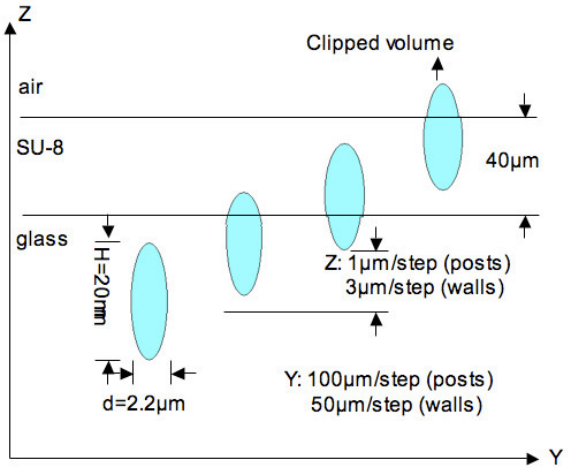

Figure 2.7. Schematic of the experimental design of the calibration approach in the axial section. The focal depth in the Z axis is deeper from right to left along the Y axis and remains the same in the X direction (into the page). The shallowest focal depth (on the right) is clipped by the photoresist layer. The dimensions indicated on the first left exposure volume is the height and width of the exposed wall at 10 mW, 10 μm/sec. The shapes of the exposure volume in air, SU-8, and glass have different dimensions because of differences the refractive index. The step-size in the Y and Z directions are shown in the figure.

To fabricate 3D microporous structures, we studied the wall width in terms of the average power and the stage moving speed using the experimental design described above. In Figure 2.8a, we show the wall widths under different average powers as a function of the stage speed. We exposed walls at an average power of 10 mW, 20 mW, 30 mW, and 40 mW and for each power we varied the stage speed at 5 μm/sec, 10 μm/sec, 20 μm/sec, and 40 μm/sec. Figure 2.8b shows an example of the exposed walls at a power of 30 mW using 4 different speeds. The stage speed was increased from left to right and the focus was decreased from top to bottom with a step length of 2 μm. As observed, some walls at the bottom of the image tipped over onto the substrate because of the shallow focal depth. Similar exposures were taken at the other three average powers.

We measured the widths of the walls from the SEM images at a magnification of 1500x (e.g. Figure 2.8d and fit the width with Eq. (2.14) as shown in Figure 2.8a. The global parameter in the fitting is C'_{th}=5.74±0.86 E-3 $mW^2.s/\mu m^5$, which gives the threshold of the direct writing wall at $w_{wall} = 0$. According to Eq. (2.14), the exposure condition is

$$\frac{4P^2}{\pi^2 w_0^2 C_{th}^{'} v} \geq 1 \qquad (2.16)$$

where P is the average power, v is the stage speed, and w_0 is the focal spot radius. Substitute in the $C_{th}^{'}$ value, gives

$$\frac{P^2}{v} \geq 3.6 \frac{mW^2}{\mu m / \text{sec}} \qquad (2.17)$$

i.e. if Eq. (2.17) is not satisfied, the photoresist will be under exposed and not fully polymerized. An example of the under polymerized wall is shown in Figure 2.9c. The walls are exposed at the power of 10 mW and the speed of 40 μm/sec, thus P^2/v = 2.5 mW^2.s/μm dissatisfying Eq. (2.17). Figure 2.9b shows the walls on the edge of the polymerization threshold at the power of 10 mW and the speed of 20 μm/sec, thus P^2/v = 5 mW^2.s/μm satisfying Eq. (2.17).

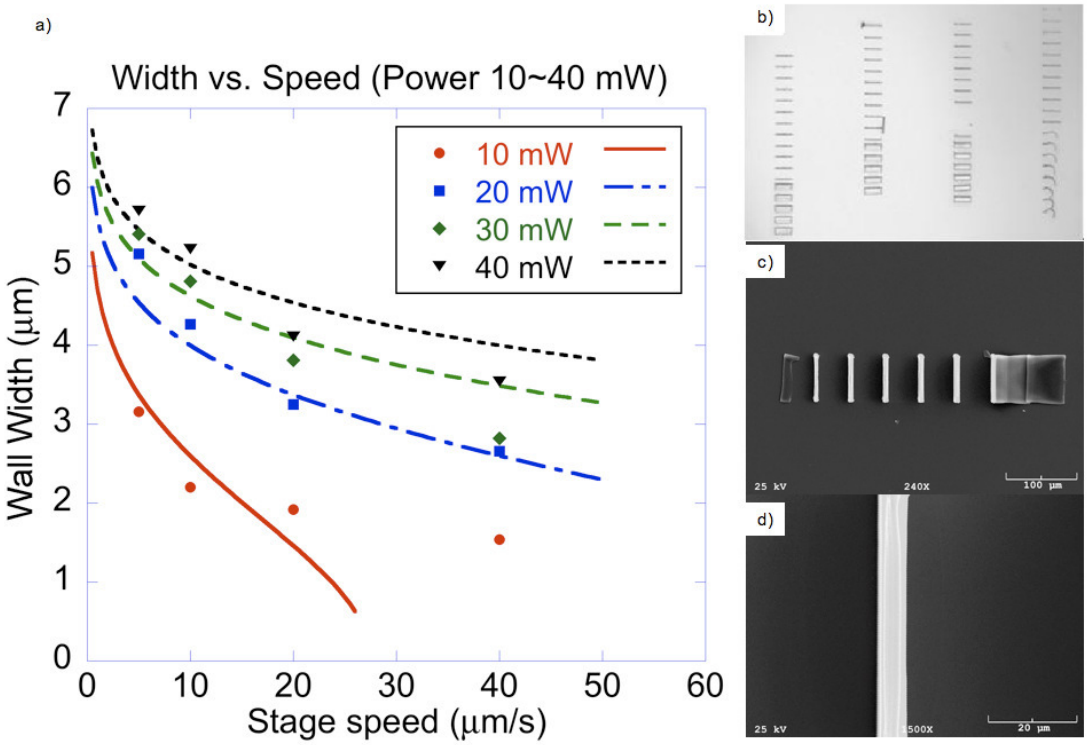

Figure 2.8. a) Wall width under different average powers (10 mW, 20 mW, 30 mW, and 40 mW) as a function of stage speed (5 μm/sec, 10 μm/sec, 20 μm/sec, and 40 μm/sec); b) Optical microscope image of walls exposed under 30 mW and speed from 5 μm/sec to 40 μm/sec from left to right and the focal depth is deeper into photoresist from lower to upper with 2 μm/step; c) SEM image of walls exposed under 40 mW and 5 μm/sec, magnification 240x; d) SEM image of the first standing wall from right in c) magnification 1500x, which is used for wall width measurements and shown in a) as a data point.

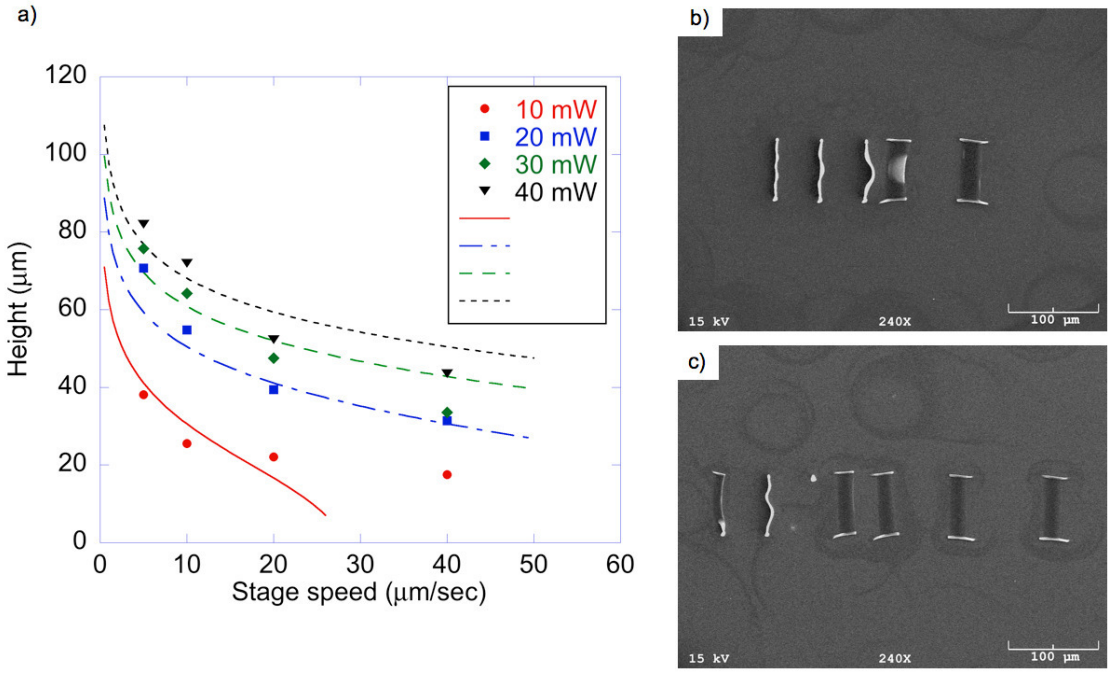

Figure 2.9. a) Exposure volume height for an average power of 10 mW, 20 mW, 30 mW, and 40 mW as a function of stage speed (5 μm/sec, 10 μm/sec, 20 μm/sec, and 40 μm/sec); b) SEM image of walls exposed under 10 mW and 20 μm/sec with a magnification 240x; c) Walls are under exposed and not fully polymerized for average powers under 10 mW and 40 μm/sec, magnification 240x.

According to Eq. (2.13), we calculated the wall heights corresponding to the measured wall width under different powers and speeds shown in Figure 2.9a, if not clipped by the photoresist layer. The curves are acquired by combining Eq. (2.13) and (2.14) and substituting in the C'_{th} value. The point (P = 10 mW, v = 40 μm/sec) in Figure 2.9a is not on the curve same as that in Figure 2.8a is because of the under polymerization according to the exposure condition Eq. (2.17). To fit 3 layers into the 40 μm SU-8 layer, the condition P = 10 mW, v = 10 μm/sec is chosen and the wall width and height are 2.2 μm and 25 μm.

2.3. Two- and Three-Dimensional Micromodels

2.3.1. Two-Dimensional Micromodels

As a first stage in the development of the system to fabricate 3D microporous structures, a single-layer 900 μm x 700 μm maze with a microchannel measuring 100 μm in width and 40 μm in height was fabricated. The channel vertical sidewall was 5.5 μm wide, as shown in Figure 2.9a. The SU-8 maze was fabricated with a pulse energy of 1.6 nJ with a stage scanning speed of 10 μm/s. To achieve a high aspect ratio of height to width, the beam expander shown in Figure 2.4 was not used. The input beam diameter was 3.1 mm and the focal spot radius (w_0) was 8 μm. The larger focal spot radius relative to the smaller beam diameter results in a larger Raleigh range of 250 μm and a higher height-to-width aspect ratio of 30 for the exposed volume. The shape of the simulated exposure dose is close to an ellipse approximately 150 μm long and 5.5 μm wide but the actual exposure dose is limited by the SU-8 thickness in the z direction.

Therefore only the center portion of 40 μm high stands on the substrate whose shape was nearly vertical. The exposure dose was simulated by the contour of equal $I^2(r,z)$ determined by Eq. (2.8). A higher pulse energy was applied as compared to that applied to a 3D model, with an average power of 160 mW, to make strong SU-8 walls.

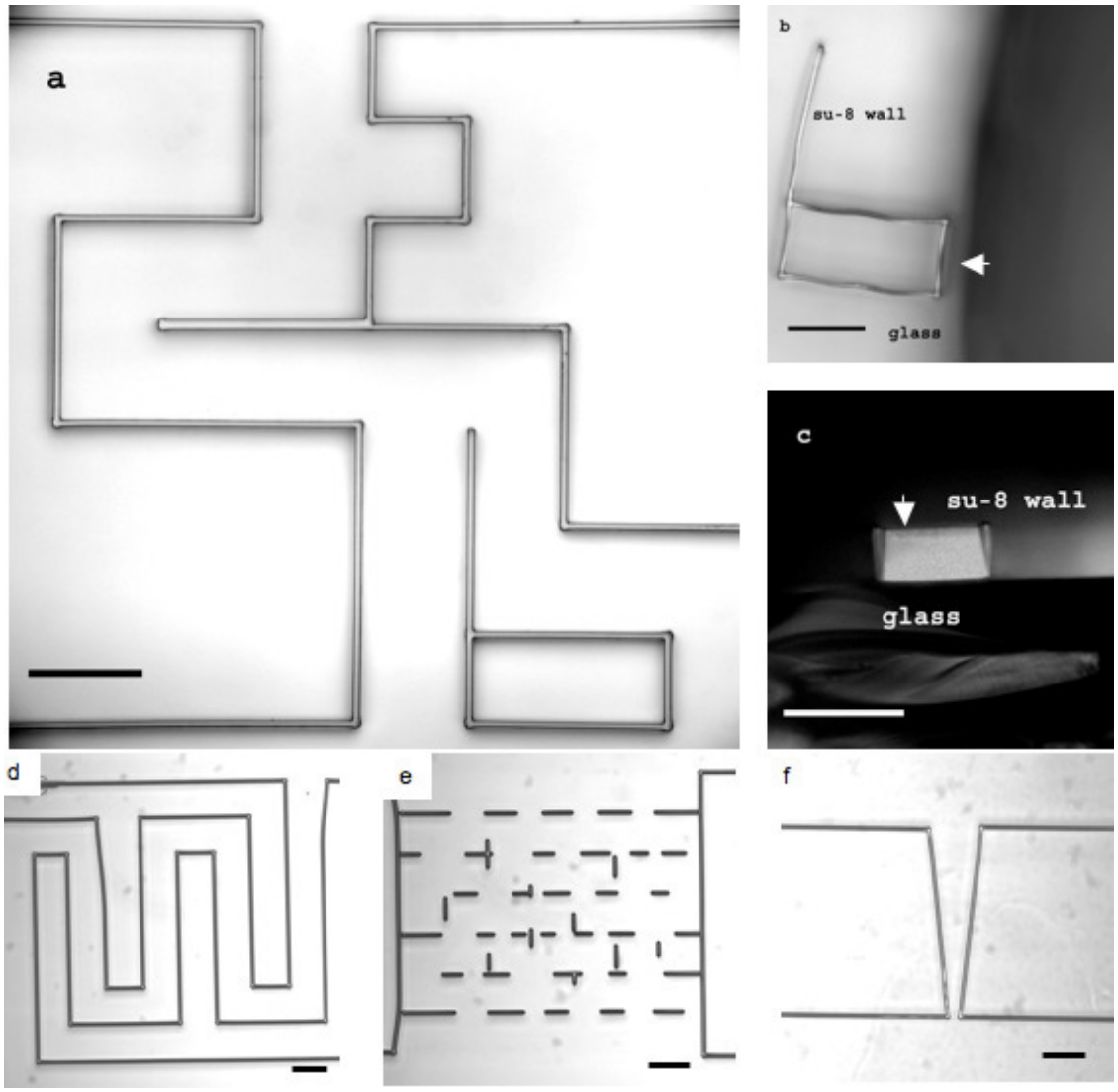

Figure 2.10. Optical microscope images of developed SU-8 microchannels. The bars in the graph are 100 μm. In a) the lateral plane image shows clean fabrication and good attachment at the base. In b) and c) we cut the cover slip to see the lateral and axial image (side view of the wall) and the arrows point out the same wall. The images shown in d)-f) are also patterns fabricated for different microfluidic studies. There are random obstacles in e). f) A wedge shaped channel whose channel width linearly decreases from 100 μm to 20 μm.

Figure 2.10 shows several other 2D micromodel patterns that were fabricated for microfluidic studies. The walls were exposed by controlling the sample stage movement and the wall attributes were controlled by adjusting the average power and stage speed. Figure 2.10a shows an optical image of a micromodel viewed from the top. The wall in the middle of the sample is

twice as wide as the others because it was exposed twice with a separation of 5 μm. Figure 2.10b and 2.10c both show the 'b' shape pattern in Figure 2.10a. The sample was cut from the side of the 'b' shape and an image was acquired with an optical microscope at a magnification of 20x. The side view image is shown in Figure 2.10c from which the wall height was determined to be 40 μm.

The pattern shown in Figure 2.10d was fabricated to observe the motion of fluid-fluid interfaces moving around corners and for measuring interfacial area. Figure 2.10e shows a channel with random horizontal and vertical obstacles. During exposure of the horizontal and vertical walls, the beam was randomly blocked. The blocked beams resulted in open channels. In Figure 2.10f, a channel with a linearly decreasing width, from 100 μm to 20 μm, is shown. It was fabricated by moving x and y directions simultaneously during exposure, and the slope was determined by the ratio of the x and y stage speed.

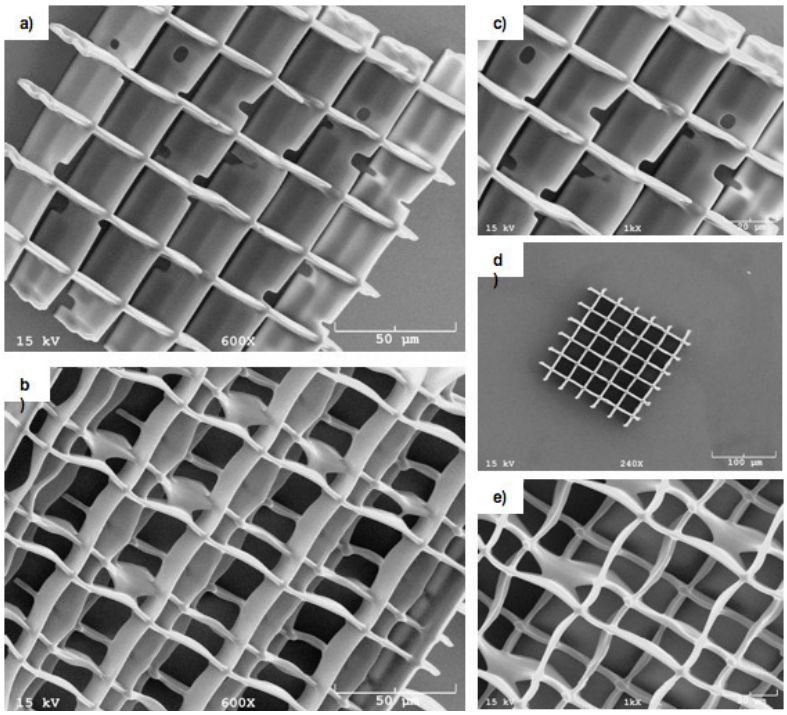

Figure 2.11. SEM images of a) the three-layer pattern with random holes in all layers and an unit-cell size of 30 μm x 30 μm, tilted by 30° for a magnification 600X; b) the three-layer shifted pattern with a unit cell size 45 μm x 45 μm, tilted by 30° for a magnification 600X; c) the same pattern as that in a) but tilted by 30° with a magnification 1000X to examine holes; d) the same pattern as that in a) without tilting, magnification 240X; e) the same pattern as that in b), without tilting, magnification 1000X.

2.3.2. Three-Dimensional Micromodels

Two types of 3-D micro-structures were fabricated to explore fluid distribution as shown in Figure 2.11. The structures in Figure 2.11 are bare structures without inlet and outlet reservoirs. These two structures were made of exposed walls created with an average power of 10 mW and

a stage speed of 10 μm/sec. A pulse energy as low as 0.1 nJ was used and the beam expander was used for a small height-to-width ratio of 10 in order to fit three levels into a 40 μm thick SU-8 micromodel. The Rayleigh range was 60 μm. The appropriate exposure was determined from the exposure curves shown in Figures 2.8a and 2.9a, which showed the relationship between the lateral width of the walls, the pulse energy, and the exposure speed. Using a combination of computer simulation and exposure experiments, we controlled the Rayleigh range to be compatible with the microstructure geometry, which is the most important part of 3D microstructure fabrication.

The first pattern shown in Figure 2.11a is a "grid" pattern with walls that contain holes at random locations in the three levels. We exposed horizontal and vertical walls level-by-level at the same X and Y locations but with 10 μm difference in focal depth in the Z direction. As the laser exposed the wall, the laser beam was blocked to make the gaps. The width of the gap was controlled by the stage speed and beam-block time. The width of the wall is 2.2 μm and the height is about 20 μm for each single wall. The total thickness of the three levels is approximately 40 μm and the overlap between levels is approximately 5 μm. The width of the random gaps in Figure 2.11a ranges from 1.6 μm to 7.5 μm.

The second pattern shown in Figure 2.11b is a shifted 3-level "mesh" pattern forming crossing pores that force fluid to move in three dimensions. On each level we exposed a single-level chessboard pattern with a full size of 45 μm x 45 μm and shifted 15 μm in both X and Y directions and shifted 10 μm in focal depth in the Z direction. The suspended walls in the center level span 45 μm and support the upper-level chessboard pattern. We also fabricated samples with spans of 30 μm and 60 μm. The walls exhibit strains (i.e. "wavy") therefore we studied the mechanical instability of the walls.

2.3.2.1. Mechanical Instability

For large structure three-dimensional micromodels, the mechanical instability of the exposed walls depends on many factors such as the average exposure power, the stage speed, and the wall dimensions. However these factors have complex relationships, e.g. the average power and the stage speed determine the wall width according to the relationship of Eq. (2.14). Therefore, at first we studied the wall length, which has no relationship with other factors. Furthermore, we developed a method to study the instability by extracting the 1D wall shape from the 2D micrograph to determine the spatial frequency spectrum of different lengths of walls.

To study the relationship between mechanical instability and the wall length, we exposed walls at lengths of 50 μm, 100 μm, 200 μm, 400 μm, and 800 μm. For all lengths, we fixed the average exposure power at 10 mW and the stage speed at 10 μm/s, under which condition we fabricated the two 3-D micromodels. The optical and SEM micrographs of the 200 μm wall are shown in Figure 2.12a and 2.12b. The horizontal walls were exposed as the "skeleton" of the vertical suspended walls, at a power of 60 mW and a speed of 10 μm/s without beam expansion. To provide sufficient support to the suspended walls, a higher average power, 60 mW, was used compared with the power of the suspended walls, 10 mW. We exposed the vertical walls as described in the calibration section, with the focal depth becoming shallower from left to right

with a difference of 3 μm/step between steps. The left four walls are attached to the substrate with different heights and the right four walls are suspended between the "skeleton" walls as a bridge.

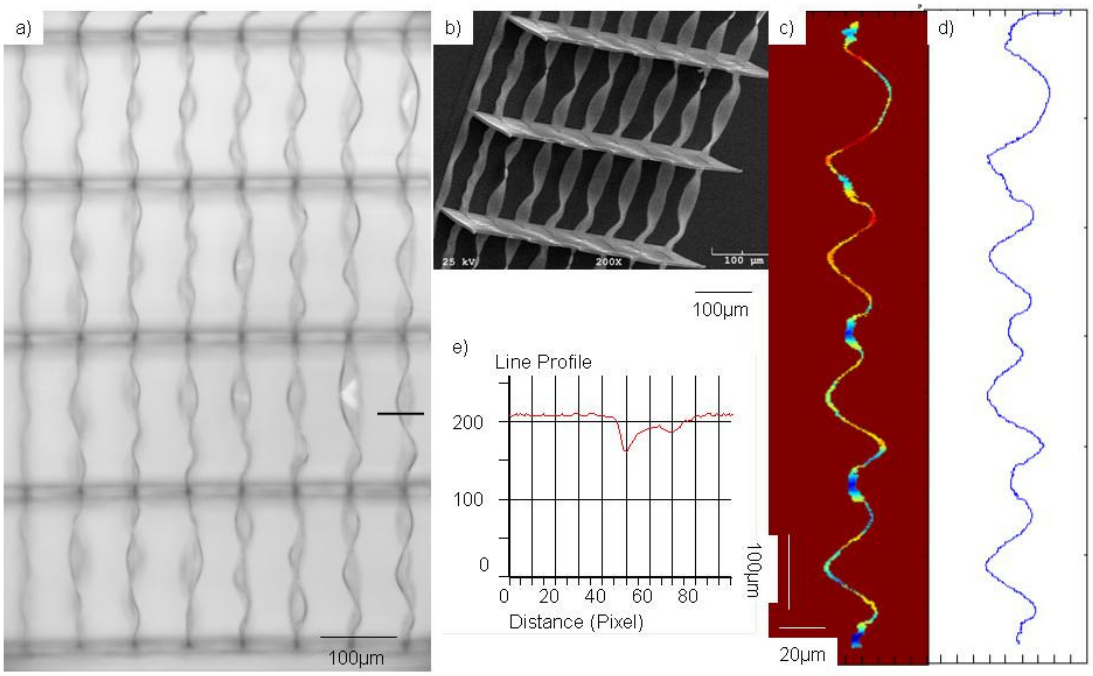

Figure 2.12. a) An optical micrograph of the group of 200 μm wall with the focal depth of the vertical wall deeper from right to left; b) the SEM image of the middle area of the walls in a) but at a magnification of 200x and tilted 45°, showing the focal position changing from the connection part of the "skeleton" wall and the "bridge" wall; c) the intensity profile of the line in a); d) the 1st right wall in a) with the background removed; and e) the extracted 1D wall curve of the 1st right wall in a).

Although the four walls were suspended at different heights caused by exposure at different focal depths, their mechanical instability should be the same because they are suspended regardless of the gap underneath. The gap between two skeleton walls determines the wall length and the gap between two vertical walls was fixed to 70 μm which is far enough to prevent interaction between two walls.

After taking the optical images of the exposed walls, the 1D wall shape was extracted from the 2D image. First, the average value of all the pixels in the image was the background value. The pixels were set to the background if their values were within 10% difference of the average value. Figure 2.12c shows an example of the wall with the background removed. To get the 1D shape from the 2D image, we extracted the wall position from each horizontal line in Figure 2.12c. For each line, the pixel on the walls had a lower value than tmhe background shown in Figure 2.12e. The peak with the minimum value showed the wall position. Thus we set a gate value as 80% of the minimum value plus 20% of the background value. Then we found two points whose values were closest to the gate value and took the mean value of the two points as the wall position. An example of the extracted wall curve is shown in Figure 2.12d. To optimize

the data extraction process, we took an image for every wall. For example, Figure 2.12a was an image especially focused on the 1st right wall.

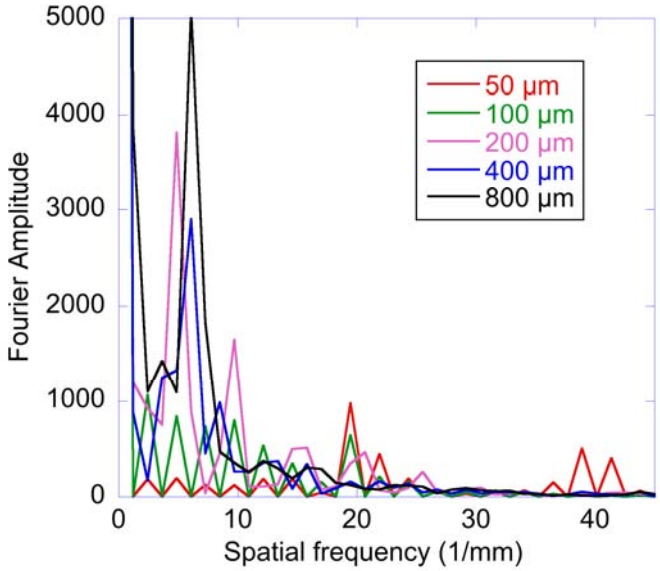

Figure 2.13. The spatial frequency spectra from the Fourier Transforms of the extracted wall curves. Different colors represented different wall lengths as shown in the legend.

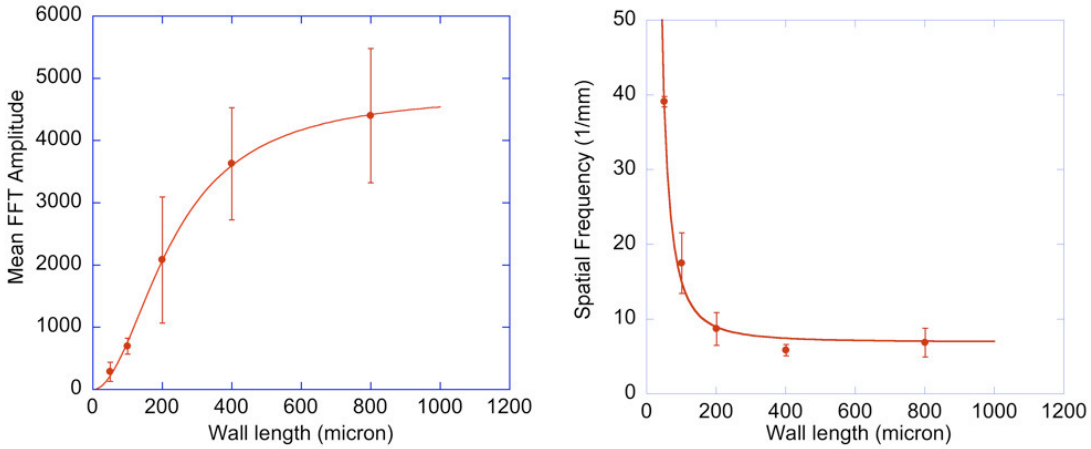

Figure 2.14. The main peak position and amplitude depends on the wall length. The data points are the mean value of the four independent groups of experiments and the error bar is the standard deviation of the four data sets. a) The spectral amplitude in terms of the wall length, and b) the spatial frequency in terms of the wall length. The turning points on two curves occur around 200-300 μm.

A Fourier Transform was performed on the extracted data to determine the spatial frequency of the instability. The analysis was performed four times for each wall length based on four different suspended walls at each length. The four spectra were averaged to emphasize the main peaks on the spectra and to lower the random noise. Figure 2.13 shows an example of the averaged spectra of all five lengths, each color representing one length. From this graph, we recorded the amplitude and the frequency of the highest peak for each wall length excluding the

peaks with frequency lower than 1/length. For example, the frequency spectrum of the 200 μm wall is shown as the magenta curve in Figure 2.13. The maximum peak was located at the frequency of 5 mm^{-1}. This frequency shows that the wall included a signal wave with a period of 200 μm. However, 200 μm was the wall length, not the wave resulting from the mechanical instability. Therefore this false peak gave no instability information. Therefore the peaks located at a frequency lower than or equal to 1/length were excluded.

To reduce the random error during the exposure, baking, developing, and rinsing procedures, we repeated the above experiment four times with all the same conditions. For each group, we plotted two graphs, the spatial frequency in terms of the wall length and the spectral amplitude in terms of the wall length, based on the values of the main peaks. Finally, we averaged the four groups of data shown in Figure 2.14. The error bar in the figure was the standard deviation from the four sets of data. The lines show turning points at 230 μm in Figure 2.14a and 285 μm in Figure 2.14b. When the wall length is smaller than approximate 250 μm (the mean value of the two turning points), the suspended wall is more likely to be mechanically stable.

2.4. Imaging Fluids

The purpose of creating two- and three-dimensional transparent micromodels was to image fluid distributions in channels with known geometries. This section describes fluid displacement experiments, results and analysis from two-dimensional micromodels that are imaged using laser confocal microscopy.

2.4.1. Flow Set-up

At Sandia, a PHD 22/2000 syringe pump (Havard Apparatus Co.) was used to pump Alex Fluor-488 water solution 1% into the flow cell. The syringe was a 500 μl Hamilton Glass Syringe with a diameter of 2 mm. A pressure transducer (Omega Engineering Inc.) was placed between the pump and inlet of the sample to measure the pressure. The transducer signal was indicated on a display meter (DP41 Omega Engineering Inc.). The inlet tubing had an inner diameter of 2 mm. The outlet was open to atmosphere. The Alex Fluor-488 was a fluorescent dye excited by a 15 mW 488 nm laser and emitting 519 nm green light. A Zeiss LSM 510 Laser Scanning Confocal Microscope was used for the imaging fluid distributions within the micromodels.

Three microfluidic structures were image: 2D samples step pattern, 2D wedge channel (Figure 2.10f) and a 3D mesh (Figure 2.11b). All samples were initially filled with water. The syringe pump was used to withdraw the water in 0.0002 ml increments which caused air to invade the sample. While withdrawing, the interface was observed through the optical channel of the microscope. When the interface started to move, withdrawal by the syringe was stopped. The system was allowed to equilibrate for 3-5 min as indicate by the stability of the pressure reading from the pressure transducer. Using laser confocal microscopy, the flow cell was scanned from the bottom to the top. Only drainage experiments were performed. The lateral and axial resolutions are set differently according to different pattern areas. The confocal information for the wedge pattern and the step pattern are given in Tables 2.1 and 2.2. Each scan takes 2-3 min depending on the scan time per frame and the frame numbers per scan. But the resolution and the

scan time are the same for each group of experiments.

Table 2.1. Confocal imaging parameters for step pattern

	x	y	z
resolution (μm/pixel)	0.89	0.89	0.89
pixel/slide number	512	512	80
scan area (μm^2)	454.66	z scan range (μm)	70.15
objective lens	20x		
pinhole diameter	25 μm (0.3 Airy Unit)		
optical slice	<2.6 μm		

Table 2.1. Confocal imaging parameters for wedge pattern.

	x	y	z
resolution (μm/pixel)	1.11	1.11	1.11
pixel/slide number	512	512	59
scan area (μm^2)	568.33	z scan range (μm)	64.38
objective lens	20x		
pinhole diameter	20 μm (0.24 Airy Unit)		
optical slice	<2.6 μm		

2.4.2. Image Processing and Analysis Results

The confocal images of the partially water-saturated samples were analyzed to extract fluid-fluid interface locations within the micromodels as well as interfacial curvature. A median filter was applied to each image to improve the image quality. All the images were filtered by a 3x3 median filter to remove noise while maintaining sufficient detail. To remove the influence of large particles, e.g. a dust in the images, a normalization technique was used. In this approach, the first stack of the scanning images of the sample with only water in the sample is used as the background. The background stack is subtracted from the later image stacks, and then divided by the background. As a result, stationary artifacts associated with fabrication are removed from the images.

The grayscale images were converted to binary images using the 'graythresh' function in Matlab to define a pixel value. This function uses Otsu's method for minimizing the intraclass variance of the black and white pixels. In the images, the white pixels (value 1) indicate fluorescent fluid and the black pixels indicate either SU-8 or air. The 'bwboundaries' function in Matlab was used to determine the boundary between white and black pixels. This extracted boundary included the fluid-photoresist and fluid-air interfaces. The fluid-photoresist interfaces were removed by subtracting the fluid-photoresist interfaces found in the background image stack from the other image stacks. In this manner, the fluid-air interfaces were identified.

The curvature of the fluid-air interfaces is related to the capillary pressure through the surface between air and water. An algorithm was used to find the curvature of the interfaces that finds the point that minimizes the standard deviation of all of the distances from this point to the points on the interface (Figure 2.15). The mean value of the distances is the radius and the point is the center of curvature. The curvature is 1/radius. This method assumes that the interface is circular.

The minimum standard deviation indicates how well the interface fits to a circle. To improve the algorithm efficiency, an initial guess is chosen as shown in Figure 2.15. Three points on the interface are used as well as two lines. The initial estimate of the center is the cross point of the perpendicular lines of the two fit lines, i.e., the red point shown in Figure 2.15.

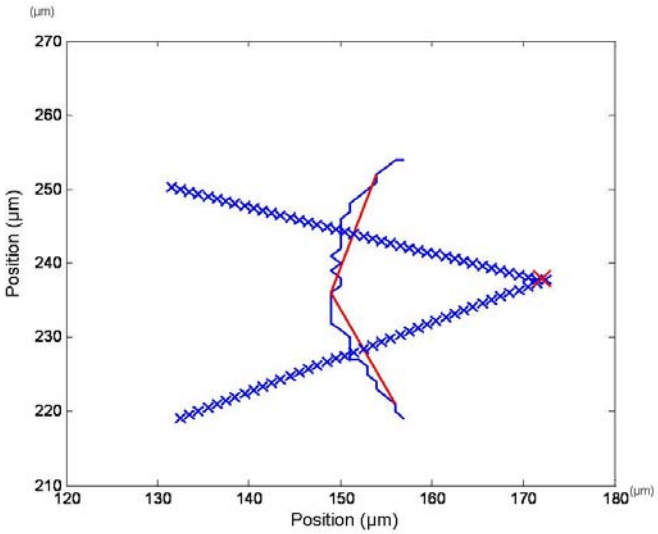

Figure 2.15. The graph shows the algorithm for finding the center of the radius of curvature. The two red lines are fit by three points chosen on the interface. The two blue lines are perpendicular to the red lines respectively. The red "X" point is the cross point of the two blue lines.

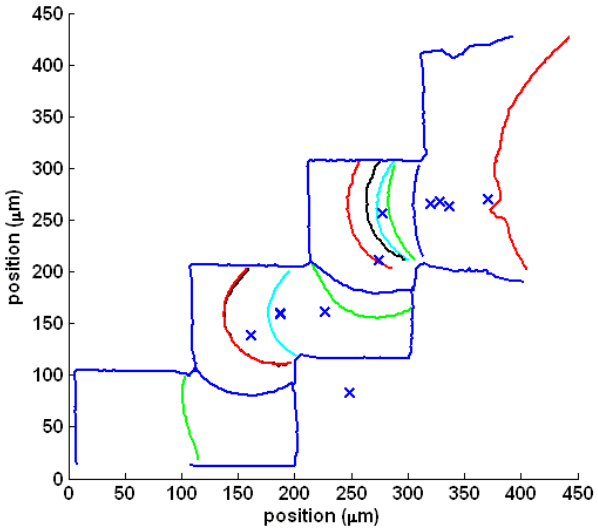

Figure 2.16. The graph shows the extracted photoresist-fluid (blue step pattern) and fluid-air interfaces observed for a series of pressure increments within the step pattern. The blue "x" points represent the centers of the radius of curvatures of the interfaces. The color of the interfaces shows the sequence of the interfaces, red, yellow, blue, green, cyan, and black repeatedly.

Figure 2.16 and Figure 2.17 show the extracted fluid-photoresist, fluid-air interfaces and the corresponding center of the step pattern and the wedge channel. The two plots in Figure 2.17 are acquired from two different data sets.

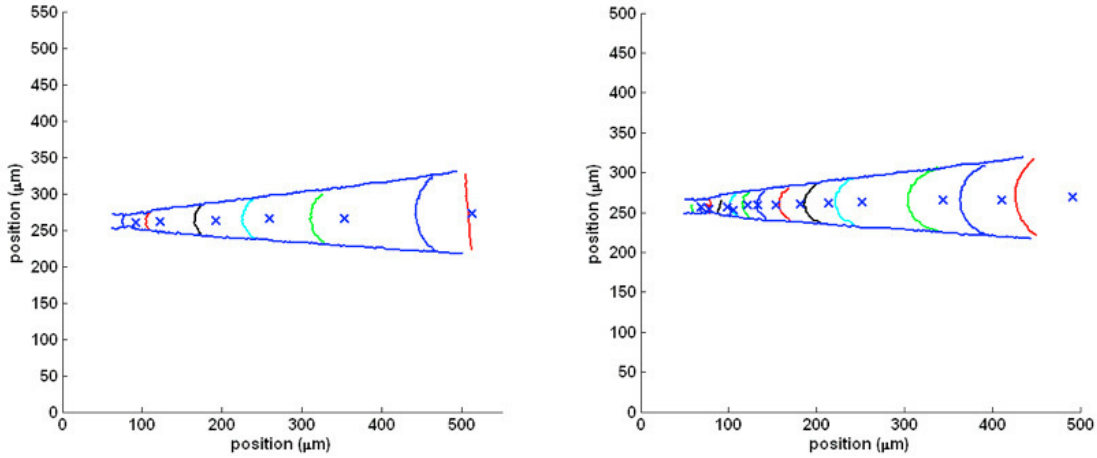

Figure 2.17. The two graphs show the extracted photoresist-fluid and fluid-air interfaces of two independent data sets from the confocal image data sets from the wedge channel. The blue "x" points and the color of the interfaces are described as the previous figure.

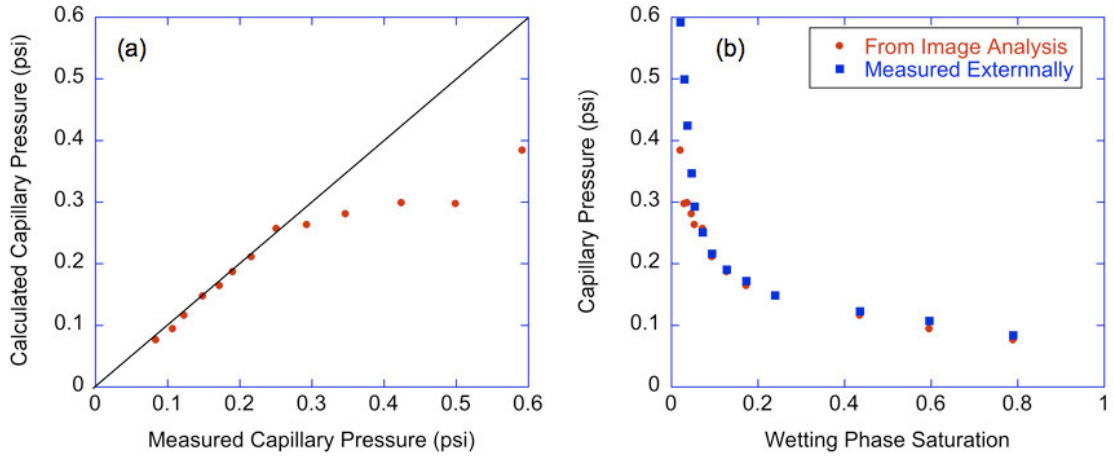

Figure 2.18. *a*) Calculated capillary pressure from curvature extracted from the confocal image stacks of drainage in the wedge pattern as a function of measured capillary pressure. *b*) Wetting phase saturation determined from the confocal images as a function of measured capillary pressure.

The curvature and wetting phase saturation were extracted from the imaging processing (Figure 2.18a and 2.18b). The saturation was calculated by counting the number of pixels representing water and dividing by the total number of pixels that compose the wedge-shaped channel. The curvature of the interface between the wetting and non-wetting phases is proportional to the capillary pressure as described by Eq. (2.4). Using a surface tension of 72.3 x 10^{-3} N/m for the water-air interface, the capillary pressure was calculated (Figure 2.18a). Figure 2.18a gives a comparison of the calculated capillary pressure using the curvatures obtained from image analysis in Eq. (2.4) to the capillary pressure measured with pressure transducers external to the sample. Initially, the calculated and measured values of capillary pressure are equal. An

analysis was performed to determine if the deviation of the calculated pressure arose from error in the image analysis technique, i.e. as the channel narrowed, the number of pixels in the image that compose the interface decreases. From the analysis, for the smallest channel radius (10 pixels), the calculated radius of curvature was 99.7% of the theoretical value. Thus, the source of the deviation is not from image analysis. One hypothesis is that the deviation occurs because of the presence of films. Figure 2.19 contains 13 images of the wedge channel corresponding to the 13 data points in Figure 2.18a and 2.18b. The images are from the mid-plane of each confocal image stack. The first image in the upper left corner represents the lowest capillary pressure. As the pressure increases, two pockets of wetting phase (water) are observed to move down the wedge. Initially, the interface moves at a higher rate than the pockets of water. Additional research is required to determine if film movement and communication with the inlet-outlet reservoirs is affecting the interpretation of capillary pressure.

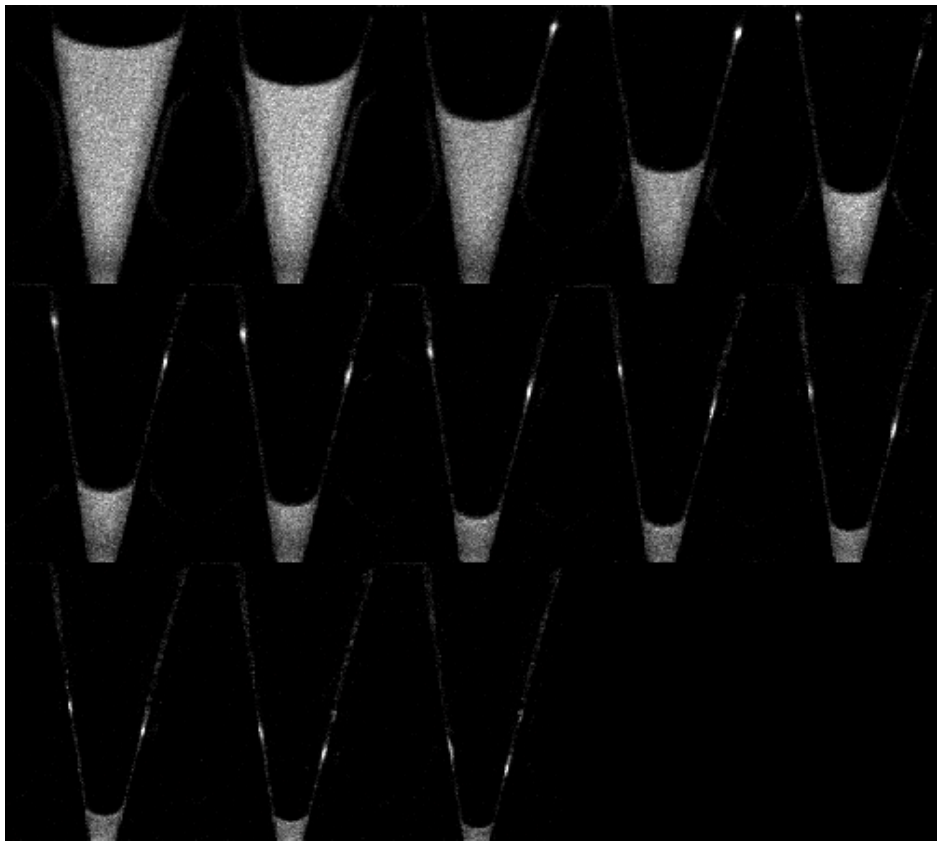

Figure 2.19. Confocal images of the wedge micromodel. Light gray regions represent water. Increasing capillary pressure from upper left to lower right.

2.5. Summary

In summary, we have developed a sample preparation protocol for photoresist SU-8, developed an optical system for two-photon laser machining, studied a 2PP system capable of fabricating arbitrary porous structures in photoresist SU-8, and developed a theoretical model for exposure volumes and calibrated the model for the two-photon exposure. Using low-power two-photon laser machining system, we fabricated several 2D micromodels and two types of 3D micromodels and studied the mechanical instability of the walls. The small fabrication dimension

of 2PP, the flexibility of laser exposure, and the simple fabrication process with the strong bonding support of SU-8 make two-photon laser machining an excellent way to fabricate arbitrary simple 3D pattern microfluidic structures. However, there are several practical drawbacks to this method, i.e. the write time and the trade-off between field-of-view and the Rayleigh range. The two-photon approach for laser writing of 2D and 3D microfluidic structures is a serial approach, i.e., one exposure shot at a time is performed. Thus, any complicated or random 2D or 3D microfluidic structure would take significant time to write. This would not be a drawback if the yield rate after sealing was 100%. Part of the long write time is associated with the field-of-view and Rayleigh range. The two-photon approach exposes an elliptical volume of photoresist. The Rayleigh range links the resolution of the cross-section of the elliptical volume to the length of the ellipse (i.e., the length of the depth that is exposed). A shorter depth results in a narrower exposure volume. Thus for a field-of-view of 500 μm on an edge, a write depth of 0.5 μm would require 1500 exposure elements across the sample. As stated earlier, using a negative resist like SU-8 requires writing all of the no-flow portions of the micromodel. To simulate sandstone, this would require randomly exposing 80% of the volume of resist. For a 500 μm x 500 μm model composed of three shot layers, this would require over 5 million exposure shots and 5 mechanical shutters (each shutter is usually rated at 1 million shuts). Thus, serial laser writing methods are best for simple 2D and 3D micro-fluidic structures or for use with positive resist. A future approach would take advantage of the parallelism of light where multiple regions of the structure are exposed simultaneously at different locations within the volume of photoresist not just at one depth like traditional photolithograpy or as in the serial approach. Recent advances in fabrication of meshes demonstrate the feasibility of parallel exposure of volumes of photoresist [56].

In the next chapter, there is a discussion of the work performed at Sandia National Laboratories to fabricate micromodels in PDMS and glass. Chapter 4 then discusses how confocal microscopy is used to examine the geometry of these micromodels and the multiphase flow in them.

2.6. References

1. Darcy, H., Determination of the laws of flow through sand. Les fontaines publiques de la ville de Dijon, Victor Dalmont, Paris, 1856: p. 590-594.
2. Bear, J., and A. Verruijt, Modeling groundwater flow and pollution. 1987, Dordrecht, The Netherlands: D. Reidel Pub. Co.
3. van Genabeek, O., and D. H. Rothman, Macroscopic manifestations of microscopic flows through porous media: Phenomenology from simulation. Annual Review of Earth and Planetary Sciences, 1996. 24: p. 63-87.
4. Muccino, J.C., W.G. Gray, and L.A. Ferrand, Toward an improved understanding of multiphase flow in porous media. Reviews of Geophysics, 1998. 36(3): p. 401-422.
5. Bear, J., Dynamics of Fluids in Porous Media. 1972, Mineola, New YOrk: Dover.
6. Dullien, F.A.L., Porous Media: Fluid Transport and Pore Structure. 1992, San Diego, CA: Academic.
7. Rapoport, L.A. and W.J. Leas, Relative permeability to liquid in liquid-gas systems. Petroleum Transaction, 1951. 192: p. 83-98.

8. H., G. and P.V. Roberts, Pore scale spatial analysis of two immiscible fluids in porous media. Water Resources Research, 1991. 27(6): p. 1165-1176.
9. Bradford, S.A., and F. J. Leij, Estimating interfacial areas for multi-fluid soil systems. Journal of Contaminant Hydrology, 1997. 27: p. 83-105.
10. Powers, S.E., Loureiro, C. O., Abriola, L. M. and W. J. Weber, Jr., Theoretical study of the significance of nonequilibrium dissolution of nonaqueous phase liquids in subsurface systems. Water Resources Research, 1991. 27(4): p. 463-477.
11. Gray, W.G. and S.M. Hassanizadeh, Averaging Theorems and Averaged Equations for Transport of Interface Properties in Multiphase Systems. International Journal of Multiphase Flow, 1989. 15(1): p. 81-95.
12. Hassanizadeh, S.M. and W.G. Gray, Mechanics and Thermodynamics of Multiphase Flow in Porous-Media Including Interphase Boundaries. Advances in Water Resources, 1990. 13(4): p. 169-186.
13. Gray, W.G. and S.M. Hassanizadeh, Unsaturated Flow Theory Including Interfacial Phenomena. Water Resources Research, 1991. 27(8): p. 1855-1863.
14. Gray, W.G. and S.M. Hassanizadeh, Macroscale continuum mechanics for multiphase porous-media flow including phases, interfaces, common lines and common points. Advances in Water Resources, 1998. 21(4): p. 261-281.
15. Reeves, P.C., and M. A. Celia, A functional relationship between capillary pressure, saturation, and interfacial area as revealed by a pore-scale network model. Water Resources Research, 1996. 32(2345-2358).
16. Bear, J., Hydraulics of Groundwater. 1979, New York: MCGraw-Hill.
17. Culligan, K.A., D. Wildenschild, B.S.B. Christensen, W.G. Gray, and M.L. Rivers, Pore scale characteristics of multiphase flow in porous media: A comparison of air-water and oil-water experiments. Advances in Water Resources, 2006. 29: p. 227-238.
18. Culligan, K.A., D. Wildenschild, B.S.B. Christensen, W.G. Gray, M.L. Rivers, and A.F.B. Tompson, Interfacial area measurements for unsaturated flow through a porous medium. Water Resources Research, 2004. 40(W12413, doi:10.1029/2004WR003278): p. W12413-1 to W12413-12.
19. Brusseau, M.L., S. Peng, G. Schnaar, and A. Murao, Measuring air-water interfacial areas with X-ray microtomography and interfacial partitioning tracer tests. Environmental Science & Technology, 2007. 41(6): p. 1956-1961.
20. Montemagno, C.D. and W.G. Gray, Photoluminescent Volumetric Imaging - a Technique for the Exploration of Multiphase Flow and Transport in Porous-Media. Geophysical Research Letters, 1995. 22(4): p. 425-428.
21. Chen, L. and T.C.G. Kibbey, Measurement of air-water interfacial area for multiple hysteretic drainage curves in an unsaturated fine sand. Langmuir, 2006. 22(16): p. 6874-6880.
22. Rao, P.S.C., Annable, M.D., Kim, H., NAPL source zone characterization and remediation technology performance assessment: recent developments and applications of tracer techniques. Journal of Contaminant Hydrology, 2000. 45: p. 63-78.
23. Saripalli, K.P., Kim, H., Rao, P.S.C., Annable, M.D., Measurement of specific fluid-fluid interfacial areas of immiscible fluids in porous media. Environmental Science and Technology, 1997. 31(3): p. 932-926.

24. Saripalli, K.P., V.L. Freedman, B.P. McGrail, and P.D. Meyer, Characterization of the specific solid-water interfacial area-water saturation relationship and its import to reactive transport. Vadose Zone Journal, 2006. 5(2): p. 777-783.
25. Schaefer, C.E., DiCarolo, D.A., Blunt, M.J., Determination of water-0il interfacial area during 3-phase gravity drainage in porous media. Journal of Colloid and Interface Science, 2000. 221: p. 308-312.
26. Annable, M.D., Jawitz, J.W., Rao, P.S.C., Dai, D.P., Kim, H., Wood, A.L., Field evaluation of interfacial and partitioning tracers for characterization of effective NAPL-water contact areas. Ground Water, 1998. 36(3): p. 495-503.
27. Anwar, A.H.M.F., Bettahar, M., Matsubayashi, U., A method for determining air-water interfacial area in variably saturated porous media. Journal of Contaminant Hydrology, 2000. 43: p. 129-146.
28. Brusseau, M.L., S. Peng, G. Schnaar, and M.S. Costanza-Robinson, Relationships among air-water interfacial area, capillary pressure, and water saturation for a sandy porous medium. Water Resources Research, 2006. 42(3).
29. Costanza-Robinson, M.S., Brusseau., M.L., Air-water interfacial areas in unsaturated soils: Evaluation of interfacial domains. Water Resources Research, 2002. 38(10): p. 1195 doi: 10.1029/2001WR000738.
30. Kim, H., Rao, P.S.C., Annable, M.D., Consistency of the interfacial tracer technique: experimental evaluation. Journal of Contaminant Hydrology, 1999. 40: p. 79-94.
31. Cheng, J.T., Pyrak-Nolte, L. J., Nolte, D. D., and N. J. Giordano, Linking pressure and saturation through interfacial areas in porous media. Geophysical Research Letters, 2004. 31(8).
32. Chen, D., Experimental Investigation of Interfacial Geometry associated with Multiphase Flow within a Porous Medium, in Department of Earth and Atmospheric Sciences. 2006, Purdue University: West Lafayette.
33. Chen, D., L.J. Pyrak-Nolte, J.D. Griffin, and N.J. Giordano, Measurement of interfacial area per volume for drainage and imbibition. to appear in Water Resources Research, 2008. doi:10.1029/2007WR006021(accepted 11 September 2007).
34. Pyrak-Nolte, L.J., D.D. Nolte, D. Chen, and N.J. Giordano, Relating capillary pressure to interfacial area. Water Resources Research, 2008. in press doi:10.1029/2007WR006434.
35. Chen, D.Q., L.J. Pyrak-Nolte, J. Griffin, and N.J. Giordano, Measurement of interfacial area per volume for drainage and imbibition. Water Resources Research, 2007. 43(12).
36. Shipley, Microelectronics Product Guide. 1982, Shipley Co., Newton, MA.
37. Giordano, N. and J.T. Cheng, Microfluid mechanics: progress and opportunities. Journal of Physics-Condensed Matter, 2001. 13(15): p. R271-R295.
38. LaBianca, N.C. and J.D. Gelorme. High-aspect-ratio resist for thick-film applications. in SPIE. 1995. Santa Clara, CA: SPIE.
39. Feng, R. and R.J. Farris, Influence of processing conditions on the thermal and mechanical properties of SU8 negative photoresist coatings. Journal of Micromechanics and Microengineering, 2003. 13: p. 80-88.
40. Shaw, J.M. and J.D. Gelorme, Negative photoresists for optical lithography. IBM Journal of Research & Development, 1997. 41: p. 81.
41. Lee, C.H., T.W. Chang, K.L. Lee, J.Y. Lin, and J. Wang, Fabricating high-aspect-ratio sub-diffraction-limit structures on silicon with two-photon photopolymerization and reactive

ion etching. Applied Physics a-Materials Science & Processing, 2004. A79: p. 2027-2031.
42. Lee, C.H., N.C. LaBianca, S.A. Rishton, S. Zolghamain, J.D. Gelorme, J.M. Shaw, and T.H.P. Chang, Micromachining applications of a high resolution ultrathick photoresist. Journal of Vacuum Science & Technology B, 1995. B 13: p. 3012-3016.
43. Teh, W.H., U. Durig, U. Drechsler, C.G. Smith, and H.J. Guntherodt, Effect of low numerical-aperture femtosecond two-photon absorption on (SU-8) resist for ultrahigh-aspect-ratio microstereolithography. Journal of Applied Physics, 2005. 97(54901-54907).
44. Lorenz, H., M. Despont, N. Fahrni, N.C. LaBianca, P. Renaus, and P. Vettiger, SU-8: a low-cost negative resist for MEMS. Journal of Micromechanics and Microengineering, 1997. 7: p. 121-124.
45. Horibe, H. and T. Kumada, Relationship between resist characteristics and matrix resin composition of chemically amplified three-component positive resist. Japan Part Ii-Electronics, 1997. 80: p. 36-45.
46. Miyagawa, K., K. Naruse, S. Ohnishi, K. Yamaguchi, K. Seko, N. Numa, and N. Iwasawa, Study on thermal crosslinking reaction of o-naphthoquinone diazides and application to electrodeposition positive photoresist. Progress in Organic Coatings, 2001. 42: p. 20-28.
47. Pacansky, J. and J.R. Lyerla, Photochemical Decomposition Mechanisms for AZ-Type Photoresists. IBM Journal of Research & Development, 1979. 23: p. 42.
48. Cumpston, B.H., Ananthavel, S. P., Barlow, S., Dyer, D. L., Ehrlich, J. E., Erskine, L. L., Heikal, A. A., Kuebler, S. M., Lee, I. Y. S., McCord-Maughon, D., Qin, J. Q., Rockel, H., Rumi, M., Wu, X. L., Marder, S. R., and J.W. Perry, Two-photon polymerization initiators for three-dimensional optical data storage and microfabrication. Nature, 1999. 398(6722): p. 51-54.
49. Duan, X.M., Sun, H. B., and Kawata, S., Microfabrication of two and three dimensional structures by two-photon polymerization. Journal of Photopolymer Science and Technology, 2004. 17(3): p. 393-396.
50. Lu, Y.M., Hasegawa, F., Goto, T., Ohkuma, S., Fukuhara, S., Kawazu, Y., Totani, K., Yamashita, T., and T. Watanabe, Highly sensitive two-photon chromophores applied to three-dimensional lithographic microfabrication: design, synthesis and characterization towards two-photon absorption cross section. Journal of Materials Chemistry, 2004. 14(1): p. 75-80.
51. Maruo, S., Nakamura, O., and S. Kawata, Three-dimensional microfabrication with two-photon-absorbed photopolymerization. Optics Letters, 1997. 22(2): p. 132-134.
52. Stute, U., Serbin, J., Kulik, C., and B. N. Chichkov, Three-dimensional micro- and nanostructuring with two-photon polymerisation. International Journal of Materials & Product Technology, 2004. 21(4): p. 273-284.
53. Sun, H.B., Matsuo, S., and Misawa, H., Three-dimensional photonic crystal structures achieved with two-photon-absorption photopolymerization of resin. Applied Physics Letters, 1999. 74(6): p. 786-788.
54. Yang, H.K., Kim, M. S., Kang, S. W., Kim, K. S., Lee, K. S., Park, S. H., Yang, D. Y., Kong, H. J., Sun, H. B., Kawata, S., and Fleitz, P., Recent progress of lithographic micro fabrication by the TPA-induced photopolymerization. Journal of Photopolymer Science and Technology, 2004. 17(3): p. 385-392.

55. Yu, T.Y., Ober, C. K., Zhou, W. H., Kuebler, S. M., Perry, J. W., and S. R. Marder, Two-photon positive tone lithography for 3-D micro fabrication. Abstracts of Papers of the American Chemical Society, 2002. 224: p. U502-U502.
56. Sato, S., H. Matsumura, S. Keino, and S. Shoji, An all SU-8 micro-fluidic chip with built-in 3D fine microstructures. Journal of Micromechanics and Microengineering, 2006. doi:10.1088/0960-1317/16/11/010, 16: p. 2318-2322.

3. SANDIA MICROMODEL FABRICATION

In addition to Purdue's SU-8 fabrication process (discussed in Chap. 2), we also pursued alternative methods for making micromodels. A variety of different approaches to microfluidic device fabrication have been reported in the literature (see Becker 2000 and McDonald 2000 for reviews). In this chapter we report on the channel designs that we fabricated and three approaches we pursued in addition to Purdue's approaches to fabricate micromodels: mold casting of silicone elastomer on microfabricated molds, pressure sealed SU-8 layers, and isotropic etching of glass.

3.1. Micromodel Designs

Figures 3.1 to 3.4 highlight the four designs we made to explore multiphase flow on the microscale. They go from simple, with an open chamber/no-post geometry in design A (Figure 3.1), to complex, with an array of post obstacles with the potential for multiple flow paths in design D (Figure 3.4). In all designs, the inlet/outlet ports for the micromodel are 3mm squares and the channels leading to the central chamber are 250µm wide at the square wells and neck down to 70µm toward the feature.

3.2. Casting of Silicone Elastomer on Microfabricated Molds

The fabrication of microchannels in silicone elastomer is well established [Duffy 1998 and McDonald 2000] and has been further extended to create multilayered structures that exploit the deformable nature of PDMS to create microvalves and micropumps [Unger 2000]. The extensive literature on PDMS microfluidic devices make it a promising candidate for making micromodels for our multiphase flow investigations. The PDMS material, however, is incompatible with many organic solvents [Lee 2003], including simple alkanes like decane, which tend to swell the polymer [Rolland 2004]. Consequently, devices made from PDMS are limited to investigation of air-water multiphase flows.

Figure 3.1: Design A was an open rectangular chamber 1000 µm long and 4000 µm wide (LEFT: overview of the whole device; RIGHT: zoom in on the region where the multiphase flow is observed).

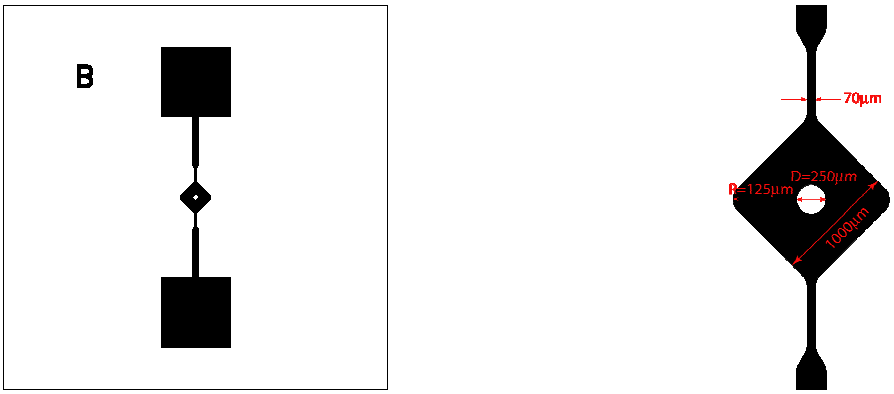

Figure 3.2: Design B was a single post design with a 250 µm diameter post centered in a 1000 µm square (LEFT: overview of the whole device; RIGHT: zoom in on the region where the multiphase flow is observed).

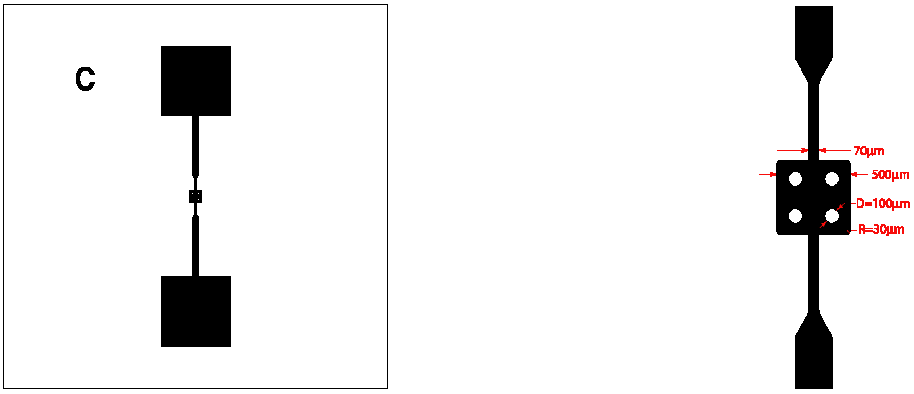

Figure 3.3: Design C was a 4-post design with 100 µm diameter posts arranged in a square pattern (center-to-center distance is 250 µm) inside a 500 µm square (LEFT: overview of the whole device; RIGHT: zoom in on the region where the multiphase flow is observed).

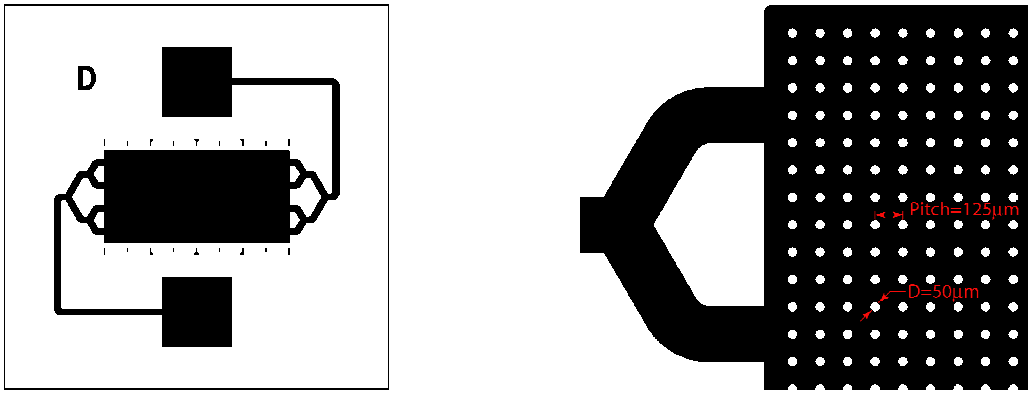

Figure 3.4: Design D was a 63x31 square array of 50 µm posts with a center-to-center distance of 125 µm (i.e. 75µm minimum gap between posts) (LEFT: overview of the whole device; RIGHT: zoom in on the region where the multiphase flow is observed).

An outline of the basic processing steps we used to make PDMS micromodels is provided in Figure 3.5, with details provided in the remaining subsections.

3.2.1. Fabrication of Molds

A master negative pattern (see Figure 3.6) of the microfluidic devices was created using photolithography. A 100 mm diameter silicon wafer was cleaned using the following procedure: rinse in acetone, isopropyl alcohol, and deionized water; dry with a stream of nitrogen gas followed by baking in an oven at 200ºC for at least 15 min; plasma clean using an oxygen plasma in downstream mode for 15 min at 150 W. After cleaning, SU-8 2025 photoresist (Microchem) was spin-coated onto the wafer. The SU-8 2025 is very viscous at room temperature, so to ensure even spreading, 4 mL of photoresist was dispensed during a 30 s period where the wafer was rotating at 150 rpm. At the end of this hold period, the rotation was accelerated from 150 to 500 rpm at 100 rpm/s, and then immediately accelerated from 500 to 3000 rpm at 300 rpm/s. The rotation was held at 3000 rpm for 30 s and then rotation was stopped at a deceleration rate of 1000 rpm/s.

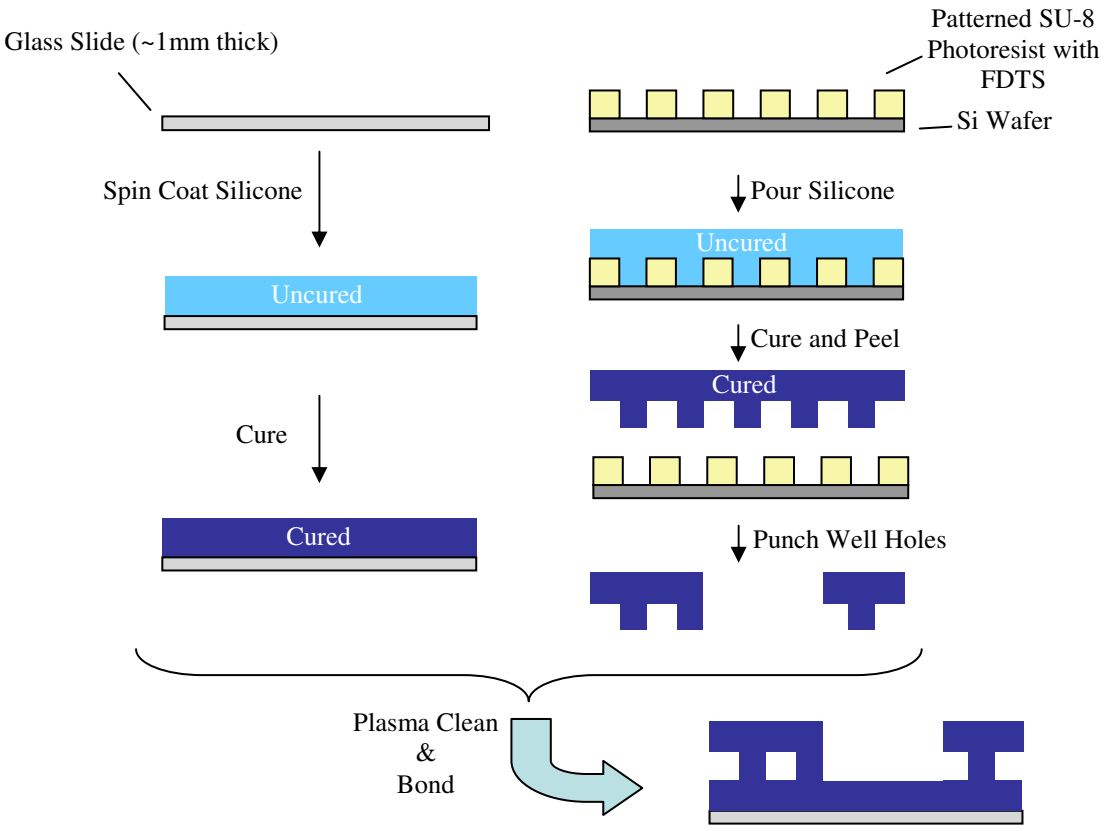

Figure 3.5: Schematic overview of the processing steps for making micromodels by casting of silicone elastomer. The process in the left column outlines the creation of a flat silicone surface and the right column the channel patterns and well holes.

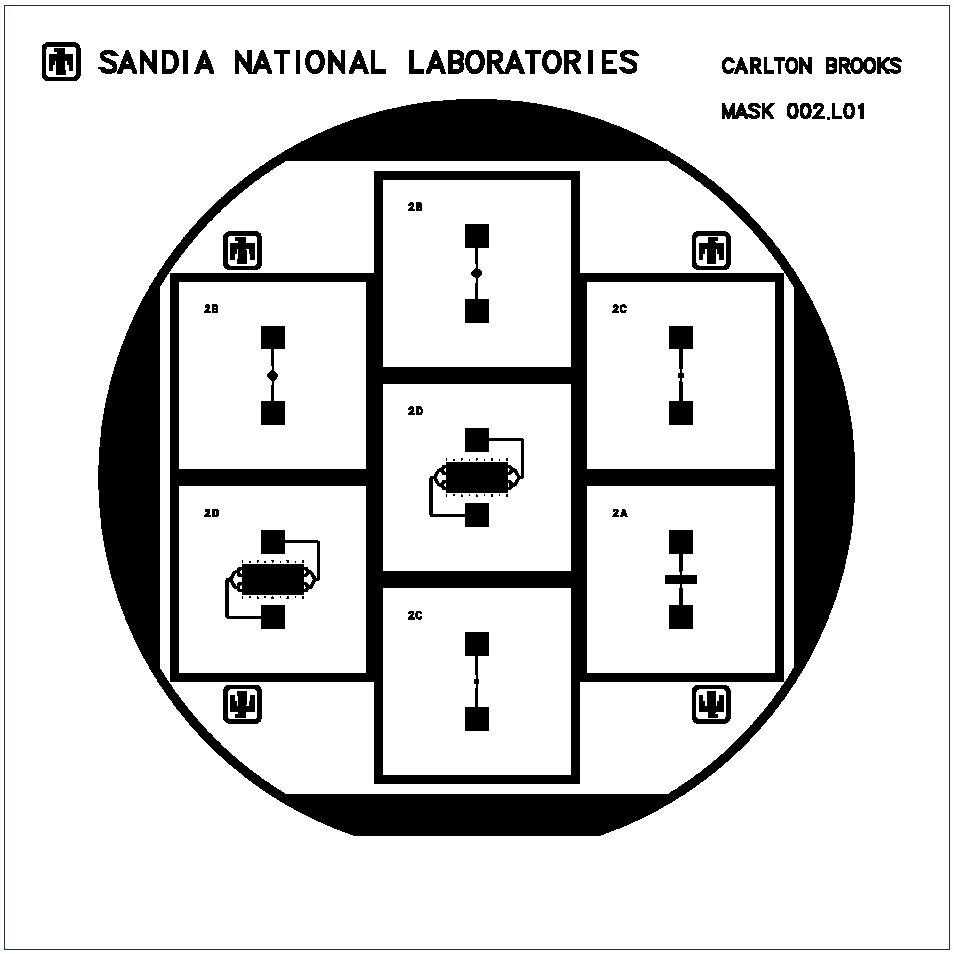

Figure 3.6: Mask design used for fabricating molds on 100 mm diameter silicon wafers. Each micromodel is a 25 mm square. Dark regions are transparent to permit crosslinking of the SU-8 photoresist. These regions will become the channels after casting with the elastomer.

After coating the wafer, it was subjected to a 2-step soft-bake process using two hotplates, 4 min at 65ºC followed by 6 min at 95ºC. This removes a majority of the carrier solvent in the photoresist. The wafer is then removed from the hotplate and allowed to cool (~5 min). Next the wafer is loaded into a mask aligner (Süss MA-6) for exposure to near UV light (i-line or 350-400 nm) with the channel mask pattern (Figure 3.6). Total exposure is 156 mJ/cm^2 (typically 12 s exposure at an intensity of 13 mW/cm^2). After exposure, the wafer is baked again to allow the progression of the crosslinking reaction in the UV exposed regions (1 min at 65ºC followed by 6 min at 95ºC). During this step, the exposed pattern appears on the wafer as the SU-8 is crosslinked. The wafer is then developed by soaking it in a crystallization dish filled with SU-8 developer and manually swirling the solution for 5 min. The wafer is then removed and rinsed using an SU-8 filled squirt bottle to remove any residual uncrosslinked SU-8. The wafer is then additionally cleaned using isopropyl alcohol, dried using a stream of nitrogen and hard-baked in an oven at 175ºC for 15 min.

3.2.2. Mold Replication

Once the master was fabricated, it was then treated with a silane before each use using vapor phase self-assembled monolayers (SAMS) to assist in the removal of the silicone molds from the master [Tripathi, 2006]. The organosilane precursor (heptadecafluoro-1,1,2,2-tetrahydrocecyl)trichlorosilane (FDTS) (Gelest) was used. The master was placed in a vacuum chamber along with 200 μL of FDTS. Once under vacuum, the FDTS vaporized and deposited onto the surface of the master. This layer created a very hydrophobic surface which allowed for easy removal of the silicone mold after curing.

The silicone elastomer used for this work was Sylgard® 184 (Dow Corning), which can be ordered as a kit containing curing agent and the elastomer base. The base and curing agent were mixed using a 10:1 ratio by mass. Once the components were thoroughly mixed, the amount of mixture to achieve the desired thickness was poured out over the silicon master in a 150 mm disposable petri dish. It was then placed under vacuum to degas the PDMS until no more air bubbles were apparent, approximately one hour. The sample was then placed in an oven at 60^{o}C to cure overnight.

To ensure a solid support, the PDMS mixture was also spin-coated onto 25 mm square glass slides 1 mm thick to form the bottom of the micromodels. Spin-coating was done at 3000 rpm for 60 s, resulting in a thickness of ~40 μm. These samples were then placed in the oven to cure at 60^{o}C overnight.

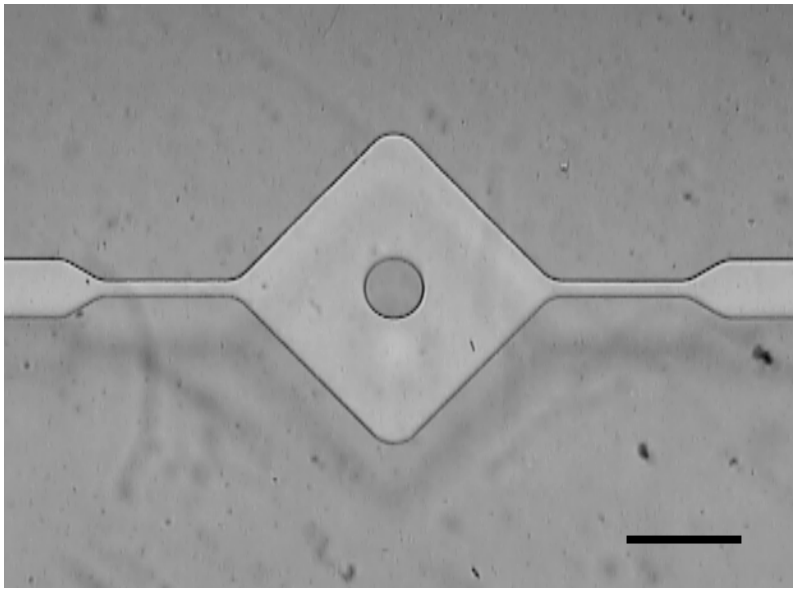

Figure 3.7: Microscope image of micromodel design B (Figure 3.2) made in PDMS using the mold replication process. No liquid is in the channels. Scale bar is 500 μm.

Once cured, the mold was peeled away from the master. The PDMS was then diced to separate the individual micromodels. Using a blunt tip needle, holes were punched through the top of the PDMS into the wells. The micromodels and the PDMS coated glass slides were then cleaned by

rinsing with acetone, isopropanol and methanol in series and then dried under nitrogen. This was done to remove any contaminants before bonding. The PDMS coated glass slides and micromodels were then plasma cleaned under an air plasma for 5 s. Immediately, the micromodels were placed onto the PDMS coated glass slides and pressed together, forming a sealed microfluidic device. Figure 3.7 shows an optical micrograph of an unfilled micromodel made from PDMS.

3.3. Pressure Sealed SU-8 Layers

One of the challenges with the fully cured SU-8 structures made by Purdue was the inability to get a pressure seal between the top and bottom halves of the micromodel. The breach was caused by the unevenness of the layers arising from edge effects when spin coating the SU-8 onto 25 mm squares. To avoid this we fabricated devices by patterning SU-8 onto 150 mm diameter x 0.5 mm thick Pyrex wafers. Presumably a flatter surface can be achieved with a larger circular substrate, and any unevenness would be confined to the circumferential region of the wafer. An outline of the basic processing steps we used to make SU-8 micromodels is provided in Figure 3.8, with details provided in the next subsection.

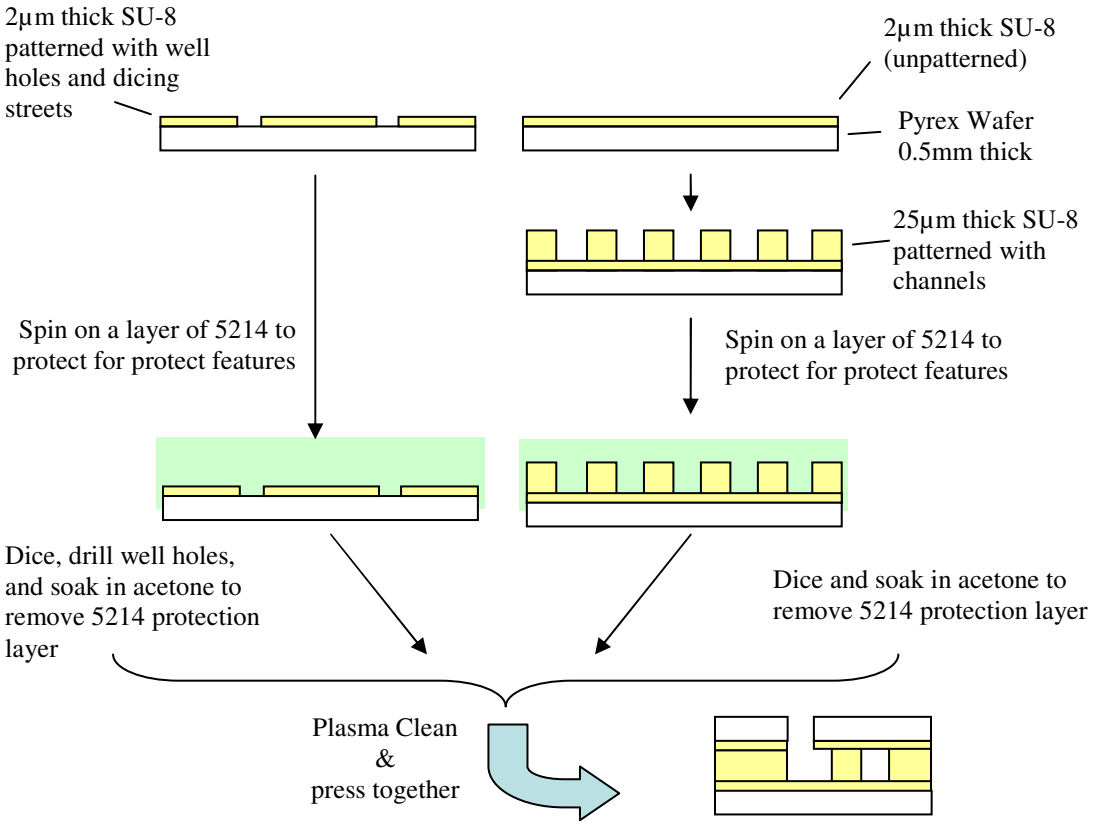

Figure 3.8: Schematic overview of the processing steps for making micromodels from SU-8. The process in the left column outlines the creation of the well plate and the right column describes the two layer SU-8 process to make the channel patterns. This three layer approach was chosen to ensure that all channel walls were made of SU-8.

3.3.1. Fabrication of Channel and Well Plates in SU-8

All 150 mm diameter Pyrex wafers were cleaned using the following procedure: rinse in acetone, isopropyl alcohol, and deionized water; dry with a stream of nitrogen gas followed by baking in an oven at 200ºC for at least 15 min; plasma clean using an oxygen plasma in downstream mode for 15 min at 150 W.

After cleaning, SU-8 2002 photoresist (Microchem) was spin-coated onto two Pyrex wafers. The SU-8 2002 is less viscous than the SU-8 2025 and is easier to work with. Similar to the previous description above, the photoresist was dispensed during a 10 s period where the wafer was rotating at 150 rpm. At the end of this hold period, the rotation was accelerated from 150 to 500 rpm at 100 rpm/s, and then immediately accelerated from 500 to 3000 rpm at 300 rpm/s. The rotation was held at 3000 rpm for 30 s and then rotation was stopped at a deceleration rate of 1000 rpm/s. After coating both wafers, they were subjected to a 2-step soft-bake process using two hotplates, 4 min at 65ºC followed by 6 min at 95ºC. The wafers are then removed from the hotplate and allowed to cool (~5 min). Next the wafers are loaded into a mask aligner (Süss MA-6) for exposure to near UV light (i-line or 350-400 nm). The well wafer is exposed to the well mask (Figure 3.9b) while the channel wafer is flood exposed (no mask). Both plates are then post-exposure baked for 1 min at 65ºC followed by 6 min at 95ºC. The well plate is set aside while the channel plate is further processed.

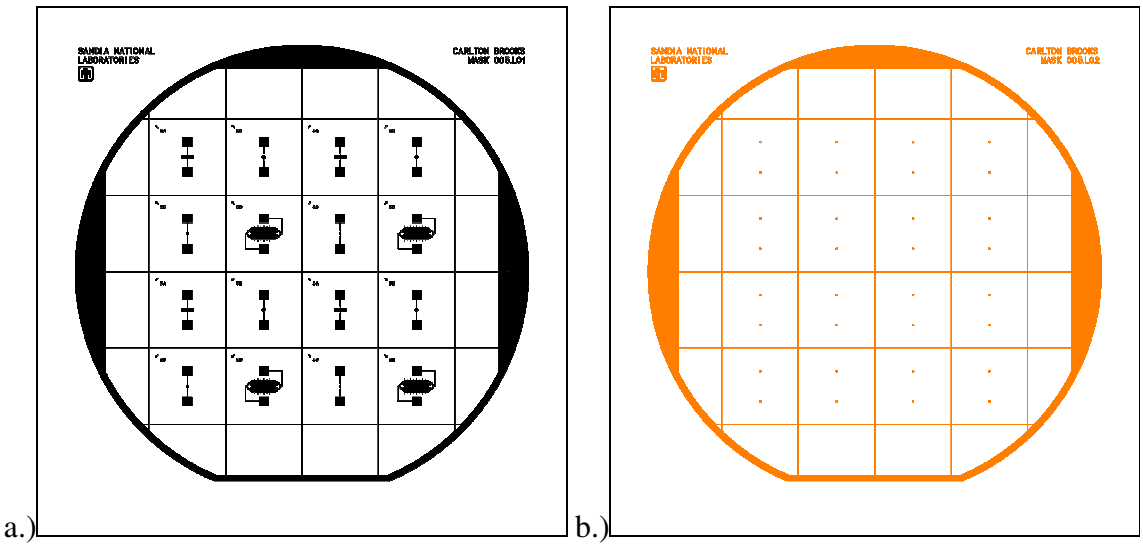

Figure 3.9: Masks used for patterning SU-8 on 150 mm diameter Pyrex wafers (0.5 mm thick). The left mask defines the channel features used for the channel plate, and the right mask is used to identify the hole drilling pattern for the well plate. Each micromodel is a 25 mm square. White regions are transparent to permit crosslinking of the SU-8 photoresist.

The channel plate is then hard-baked at 175ºC for 15 min. After allowing to cool, SU-8 2025 photoresist was spin-coated onto the wafer over the first thin layer of SU-8, soft-baked, and

exposed to the channel mask (Figure 3.9a). The channel plate was post-exposure baked and then, along with the well plate, developed in SU-8 developer, rinsed, and dried.

Both plates are then hard-baked at 175ºC for 15 min, coated with a protective layer of 5214 to avoid damage and debris from getting in the channels, and diced into 25 mm squares. The well plate is then drilled using a diamond burr drill bit (DiamondBurs.net) attached to rigidly mounted rotary tool (Dremel). Once dicing and drilling were completed, the 5214 protective layer was removed by soaking 1 min in acetone. The top and bottom layers are sandwiched together to create the channels.

Figure 3.10 shows a microscope image of an unfilled channel made from SU-8.

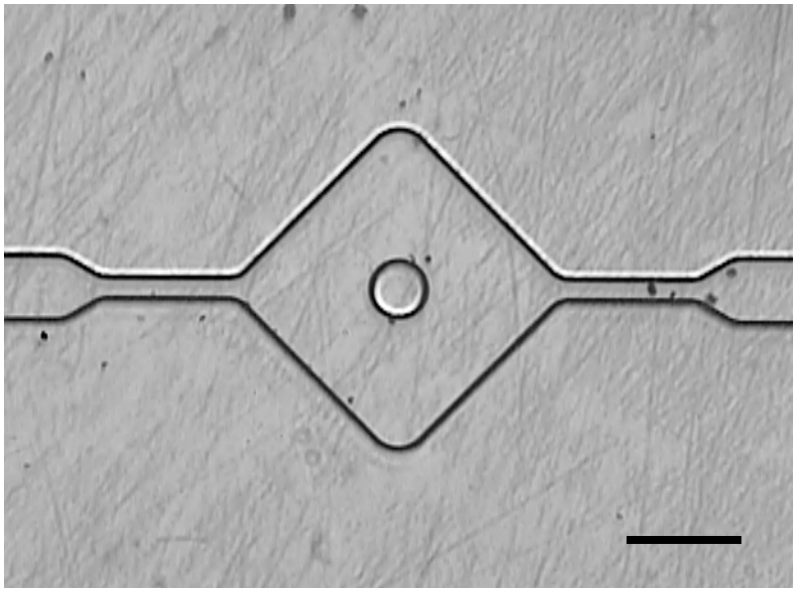

Figure 3.10: Microscope image of micromodel design B (Figure 3.2) made in SU-8 and pressure sealed. No liquid is in the channels. Scale bar is 500 μm.

3.4. Isotropically Etched Glass

A third material for fabrication of micromodels was glass, which has also been used extensively by others [Manz 1992 and Jacobson 1994]. Glass offers many benefits over the other approaches, such as solvent compatibility and re-usability. Some disadvantages are the technical challenges involved in fabrication, such as bonding the two glass layers together with high yield, and the dedicated infrastructure needed to make them. We had the devices fabricated at Washington Technology Center (WTC) (Seattle, WA). Another important thing to note is that the isotropic etching process used to make the channels produces channels with rectangular cross-sections, with two corners on the long side rounded with a radius of curvature equal to the channel depth (see Figure 3.11).

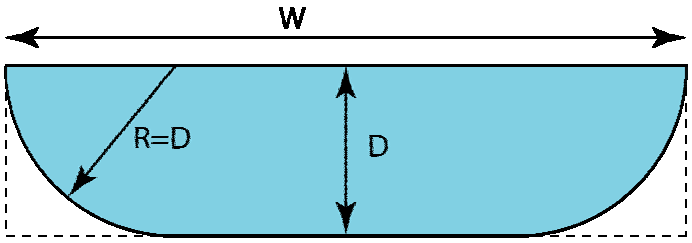

Figure 3.11: Schematic of cross-section of glass channels from isotropic etching. The etch mask has a width of (W-2D). During the etching process the glass is removed equally in all directions. After etching, in addition to etching to a depth D, the channel is also expanded relative to the mask by 2D.

3.4.1. Fabrication of Channel and Well Plates in Glass

An overview of the process used to make the devices is provided here based on the traveler sheet provided by WTC. The channel plate was made on 100 mm diameter borofloat glass 0.3 mm thick. A 300 Å Ti/W followed by a 2000 Å Au layer was deposited followed by spin coating on AZ1512 photoresist. The photoresist was patterned with the channel mask, followed by etching of the exposed Au/Ti/W metal layer. The exposed borosilicate glass was then etched in a 10:1 H_20:HF solution to reach a target depth of 30 µm. After etching the glass, the remaining photoresist was stripped and the Au mask etched from the surface.

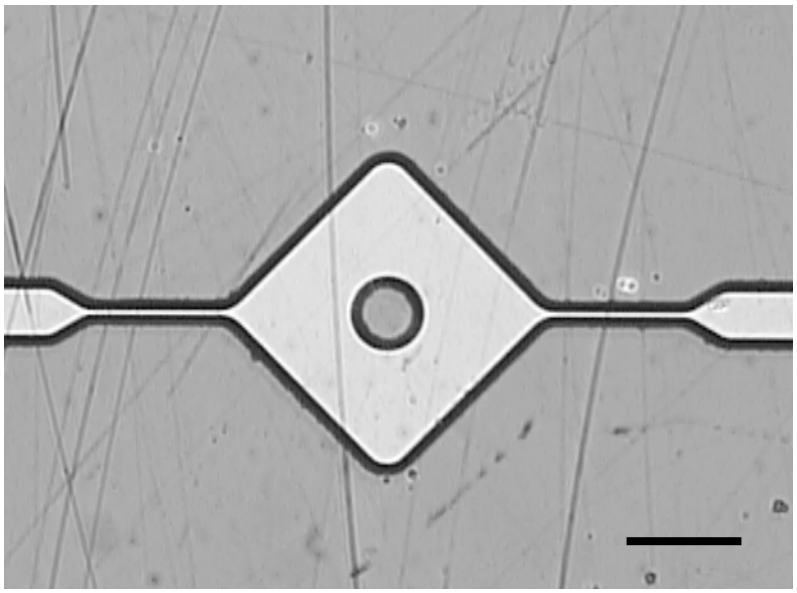

Figure 3.12: Microscope image of micromodel design B (Figure 3.2) made in glass. No liquid is in the channels. The shading on the edges of the channel is due to the rounded corners from the isotropic etching process. Scale bar is 500 µm.

The well plate was made on 100 mm diameter borofloat glass 1.0 mm thick. Amorphous silicon (~500 Å) was deposited via plasma enhanced chemical vapor deposition (PECVD). This silicon acts as a bond interface and gave the finished devices an amber looking color. A High Tack

Rapid Mask (Ikonics) was applied to both sides and exposed to the well plate mask. The plate was then grit blasted with SiC media until all ports are through the wafer. The mask was removed with water.

Both the channel and well plates were then cleaned in piranha (4:1 H_2SO_4:H_2O_2) for 10 min at reaction temperature. The amorphous silicon side of the well plate was placed next to the channel side of the channel plate, pressure applied and subjected to 365ºC and 600 V (anodic bonding process). The channels were then diced into 25 mm squares. A representative microscope image of the devices is shown in Figure 3.12.

3.5. References

Becker, H., Gärtner, C. "Polymer microfabrication methods for microfluidic analytical applications" *Electrophoresis* **2000**, *21*, 12-26.

Duffy, D.C., McDonald, J.C., Schueller, J.A., Whitesides, G.M. "Rapid Prototyping of Microfluidic Systems in Poly(dimethylsiloxane)" *Anal. Chem.* **1998**, *70*, 4974-4984.

Jacobson, S.C., Hergenröder, R., Koutny, L.B., Warmack, R.J., Ramsey, J.M. "Effects of Injection Schemes and Column Geometry on the Performance of Microchip Electrophoresis Devices" *Anal. Chem.* **1994**, *66*, 1107-1113.

Lee, J.N., Park, C., Whitesides, G.M. "Solvent Compatibility of Poly(dimethylsiloxane)-Based Microfluidic Devices" *Anal. Chem.* **2003**, *75*, 6544-6554.

Manz, A., Harrison, D.J., Verpoorte, E.M.J., Fettinger, J.C., Paulus, A., Lüdi, H., Widmer, H.M. "Planar chips technology for miniaturization and integration of separation techniques into monitoring systems" *J. Chromatography* **1992**, *593*, 253-258.

McDonald, J.C., Duffy, D.C., Anderson, J.R., Chiu, D.T., Wu, H., Schueller, O.J.A., Whitesides, G.M. "Fabrication of microfluidic systems in poly(dimethylsiloxane)" *Electrophoresis* **2000**, *21*, 27-40.

Rolland, J.P., Van Dam, R.M., Schorzman, D.A., Quake, S.R., DeSimone, J.M. "Solvent-Resistant Photcurable 'Liquid Teflon' for Microfluidic Device Fabrication" *J. Am. Chem. Soc.* **2004**, *126*, 2322-2323.

Tripathi, A. **2006**, personal communication.

Unger, M.A., Chou, H-P, Thorsen, T., Scherer, A., Quake, S.R. "Monolithic Microfabricated Valves and Pumps by Multilayer Soft Lithography" *Science* **2000**, *288*, 113-116.

4. CONFOCAL IMAGING OF TRANSIENT MULTIPHASE FLOW IN MICROMODELS

4.1. Imaging Setup

Confocal Laser Scanning Microscopy (CLSM) was the technique used to visualize the multiphase flow through the micromodels. The micromodels were placed in a custom built cartridge (see Figure 4.1) that could be placed on the microscope stage. The top part of the cartridge was made of acrylic with polished sides to make them transparent. The bottom of the cartridge was made from aluminum and had a recessed stage that was cut out where the micromodel was placed. The two parts were held together with screws to ensure a tight seal. In the acrylic, channels were drilled from the sides and down through the bottom where o-rings sealed the channels to the inlet/outlet holes in the micromodel. Barbed connectors were placed on the sides of the channels to allow for tubing to be connected up to the cartridge. The tubing was then connected to a syringe placed in a syringe pump (see Figure 4.2) to allow for constant flowing of the fluid through the micromodel during visualization.

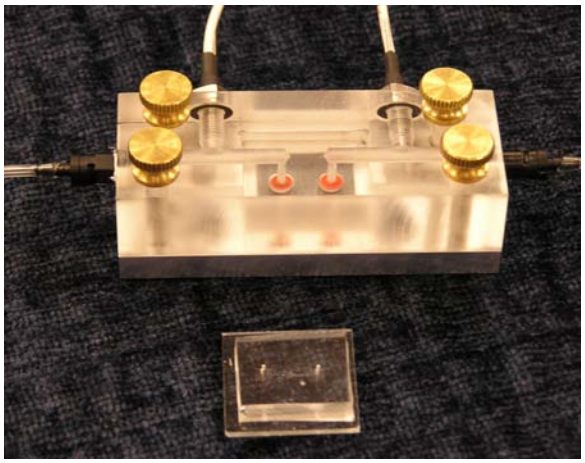

Figure 4.1. Sample cartridge that was used to hold micromodels during confocal imaging. The tubes going out of the left and right of the cartridge are the fluid inlet and outlet. The wires at the back of the cartridge are connected to the pressure transducers that are located inside the chamber. In front of the cartridge is a PDMS micromodel.

The objective of this study was to investigate the flow of a two-phase system through micropore-like structures to mimic water injection oil recovery in microporous media. Consequently, for this work we used decane to simulate the oil-phase and deionized water for the water phase. To visually differentiate the two fluids and clearly identify the decane-water interface using the confocal microscope, a pair of fluorescent dyes that favorably partitions into one phase over the other and emits at different wavelengths was needed. Three different dyes were investigated in the study (see Table 4.1). Alexa Fluor® 488 and 633 are water soluble dyes, while Nile Red is soluble in organics but nearly insoluble in water.

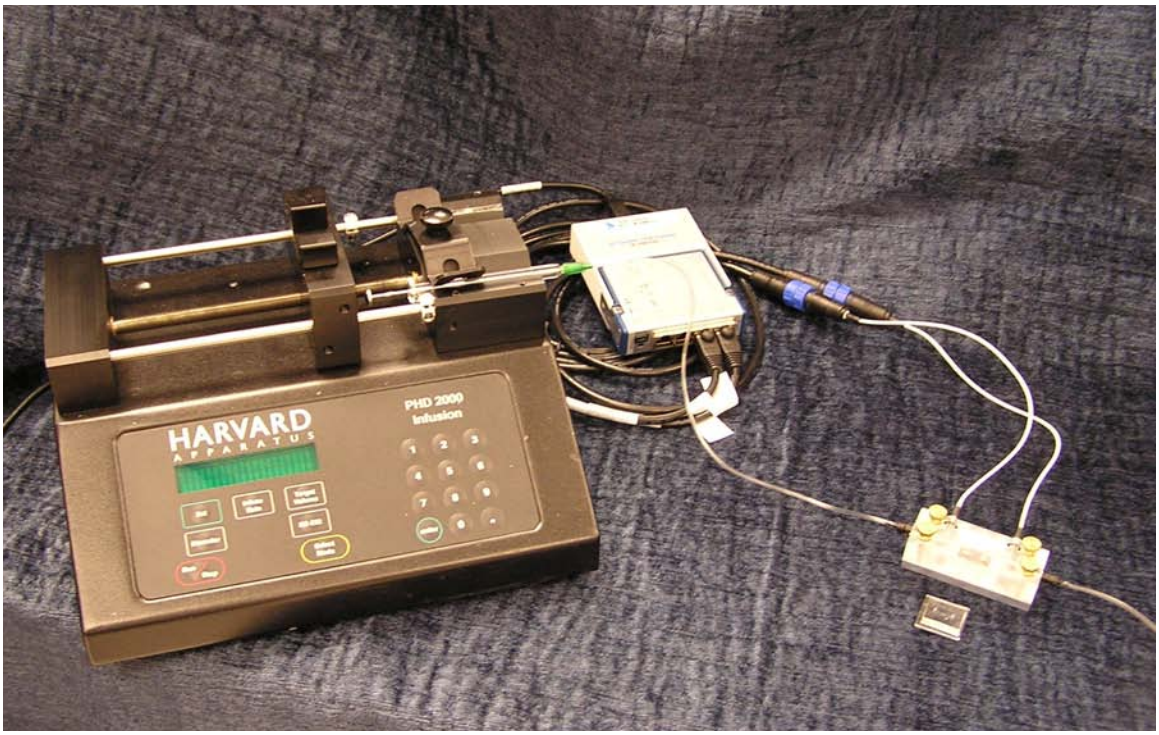

Figure 4.2. Pumping system used to flow liquids through the micromodels. A syringe pump constantly feeds liquid through a tube connected to the cartridge.

Table 4.1. Fluorescent properties of the dyes used for confocal imaging.[1]

Dye	Solvent	Excitation Maximum (nm)	Emission Maximum (nm)
Alexa Fluor® 488	Water	495	519
Alexa Fluor® 633	Water	632	647
Nile Red	Glyceryl Trioctanoate	509	583

It is well documented that the fluorescence properties of Nile Red are dependent upon the solvent that is used (Greenspan 1985), therefore the data listed in Table 4.1 may not be an accurate representation of the Nile Red/Decane system. To address this, initial experiments were performed to determine the appropriate excitation wavelengths needed for the selected dye-solvent pairs. Nile Red was mixed with decane at a concentration of 0.1 mg/ml. Once dissolved, the solution was injected with a syringe into a bonded SU-8 micromodel. The sample was then placed on the microscope stage and images were taken. Initially, the 543 nm HeNe laser line was used to try to excite the Nile Red solution with higher wavelength filters to collect the emission signal. However, the signal collected was of very low intensity. Once the laser line was switched to the 488 nm Argon line, a much more intense signal was observed at a lower emission wavelength, that between 505 and 545 nm. Because the emission of the Nile Red in oil when excited with 488 nm is very similar to Alexa Fluor® 488, it was determined that the appropriate water-soluble dye to be used in the two-phase experiments would be Alexa Fluor® 633 due to its higher emission maximum in water when excited at 633 nm. To verify this was the correct

[1] Data obtained from Invitrogen Corporation website, www.invitrogen.com.

system, a validation experiment was conducted using Alexa Fluor® 633 dissolved in water and Nile Red dissolved in decane, both at concentrations of 0.1 mg/ml. The two fluids were put in a capillary tube and the interface was imaged, as shown in Figure 4.3, using the configuration listed in Table 4.2. From Figure 4.3, it is clear that there is a significant difference in the emission from the water with Alexa Fluor® 633 (pink) and the decane with Nile Red (teal). This will ensure that we will be able to accurately image and discern the interface between the two liquids as it traverses through the micromodels.

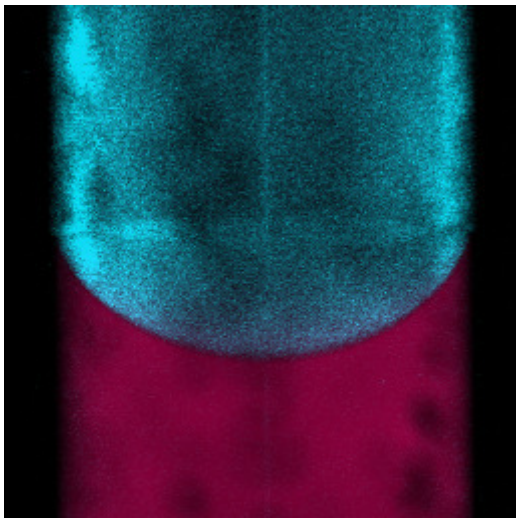

Figure 4.3. Confocal micrograph of a glass capillary tube with decane dyed with Nile Red (teal) and water dyed with Alexa Fluor® 633 (pink).

Table 4.2. Configuration of the confocal microscope for imaging Nile Red/decane and Alexa Fluor® 633/water.

Laser 1	Argon 488 at 85% power
Laser 2	Helium Neon 633 at 85% power
Main Dichroic Beam Splitter	HFT UV/488/543/633
Secondary Dichroic Beam Splitter	NFT 545
Channel 2 Emission Filter	LP 505
Channel 3 Emission Filter	LP 650

4.2. Micromodels Made from SU-8

Initially, our intention was to have the micromodels fabricated at Purdue University using the method described previously in Chapter 2. However, difficulties arose due to the bonding process that was being used during fabrication. While the patterned side of the micromodel was fabricated with fully cured and crosslinked SU-8, the top of the micromodel was pressed to the bottom while the SU-8 was still in a liquid phase, allowing for the material to spread and refill the patterned channels. An optical micrograph of a micromodel fabricated using this process is shown in Figure 4.4. One can see that this micromodel does not have the straight, uniform channels and features that were desired (see Chapter 3). Additionally, confocal microscopy

shows that the channels are partially blocked from the SU-8 reflowing into them, as shown in Figure 4.5, where the micromodel is filled with Nile Red/decane.

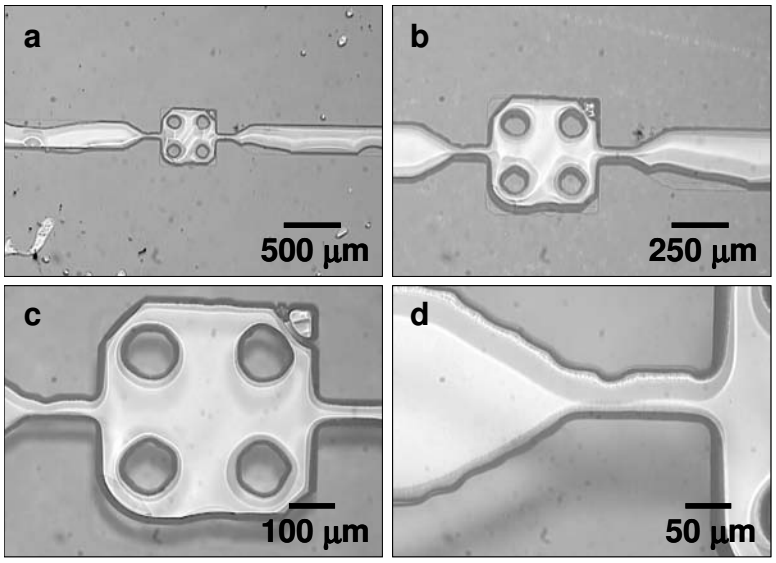

Figure 4.4. Optical micrographs of bonded SU-8 samples made at Purdue University with magnifications of a) 2.5X, b) 5X, c) 10X and d) 20X.

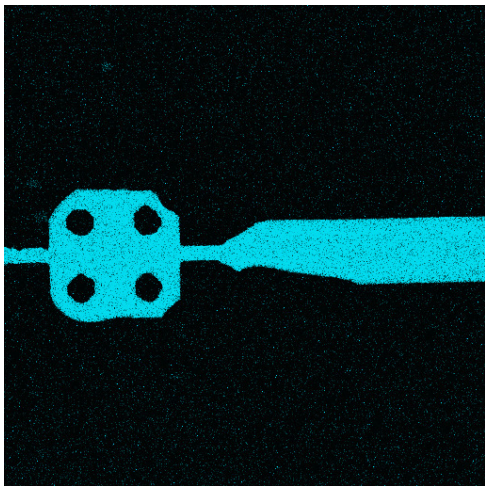

Figure 4.5. Confocal micrograph of the bonded SU-8 sample shown in Figure 4.4 filled with Nile Red/decane.

Since the bonding process proved to be a problem in the fabrication of the SU-8 micromodels, it was hypothesized that we may be able to use samples that are not chemically bonded, but ones that are physically bonded by pressing the two layers together to make a seal. Assuming the samples are microscopically flat, if they are pressed together with uniform pressure, the channels should be sealed and no leaks should be possible. This process would allow for both the top and bottom of the micromodel to be baked and therefore there should be no refilling of the channels, giving us uniform channels and features, as shown in Figure 4.6 where one can see the patterned side of the micromodel. However, when this was placed in the cartridge and water with Alexa Fluor® 488 was pumped in at a rate of 0.1 µl/min, the water leaked out of the channels, as shown

in Figure 4.7. Presumably the leaking occurs because the SU-8 is not microscopically flat, resulting in its inability to form a leak-proof seal between the two sides. This lack of flatness probably happens since the SU-8 is spin-coated onto a 25 mm square coverslip – edge effects that result in slight curvature of the top surface of SU-8 are difficult to avoid. In an attempt to avoid these edge effects, SU-8 patterned wafers were processed at Sandia National Laboratories on 150 mm diameter Pyrex glass wafers. It was believed that spin-coating the SU-8 onto the larger wafer with the micromodel patterns in the middle would lead to a flatter surface. However, these samples also leaked upon inspection with the confocal, just as the samples from Purdue University did.

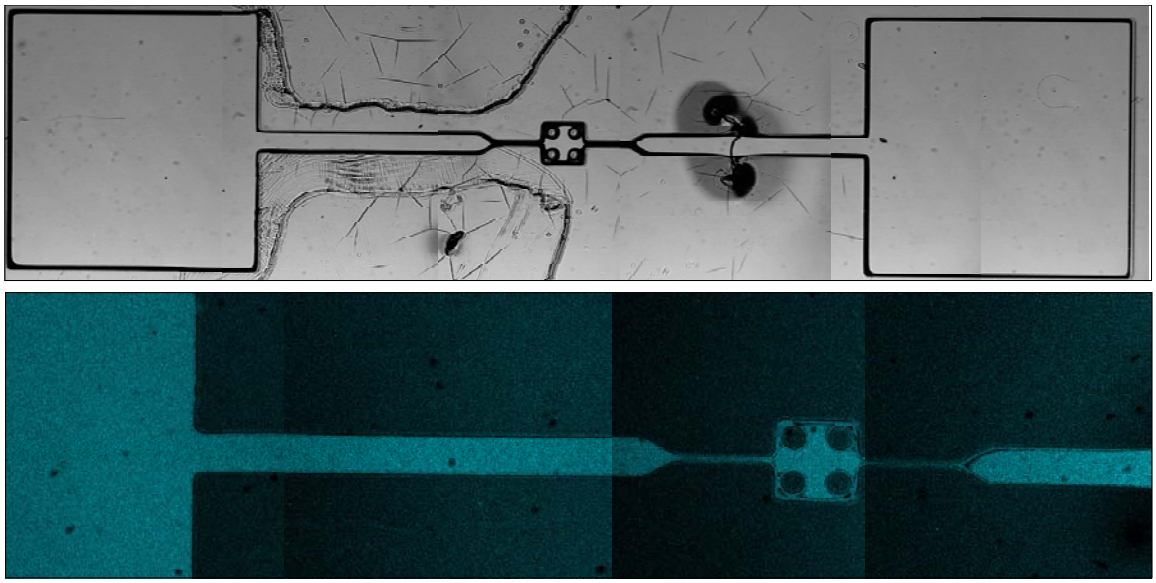

Figure 4.6. Top: Tiled optical micrographs of an unbonded SU-8 sample made at Purdue University. Bottom: Tiled confocal images of the unbonded SU-8 sample filled with Alexa Fluor® 488/water.

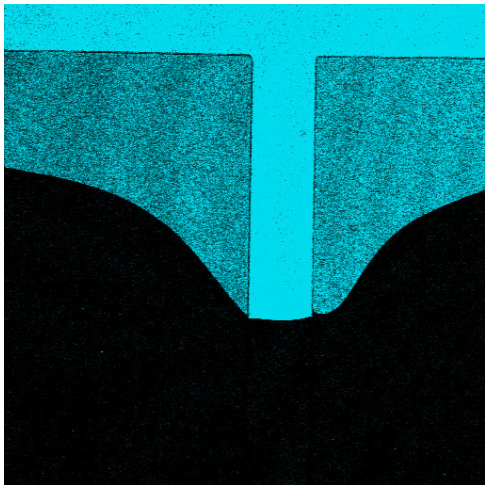

Figure 4.7. Confocal micrograph of an unbonded SU-8 micromodel from Purdue in the cartridge as Alexa Fluor® 488/water is flowing into it.

4.3. Micromodels Made from Silicone Elastomer (Water Displacing Air)

In an attempt to fabricate alternative micromodels that would not leak while still having the uniform channels and features that were needed, the replica molding process described previously using PDMS was investigated. However, one disadvantage to using PDMS is that the material swells in the presence of organic liquids, consequently attempts to use decane or any other oil phase resulted in the channels swelling shut. Therefore, experiments were performed where water with Alexa Fluor® 488 displaced air in the micromodels. In Figure 4.8, one can see water (teal) displacing air as it flows through the PDMS micromodel over time. Here, the water is being pumped into the micromodel with a volumetric flow rate of 0.1 µl/min. One observation is that the water seems to stop at the inlet to the micromodel for a long period of time before it bursts through quickly. This phenomenon is known as Haines' jump (Haines 1930, Miller 1956). Because the water does not wet the PDMS surface (equilibrium contact angle of water on PDMS was measured to be approximately 102^{o}, surface tension of water is 72.8 mN/m), the water must overcome a threshold pressure before it will move into the open feature of the micromodel. Once this threshold pressure is reached, the liquid quickly passes through the feature.

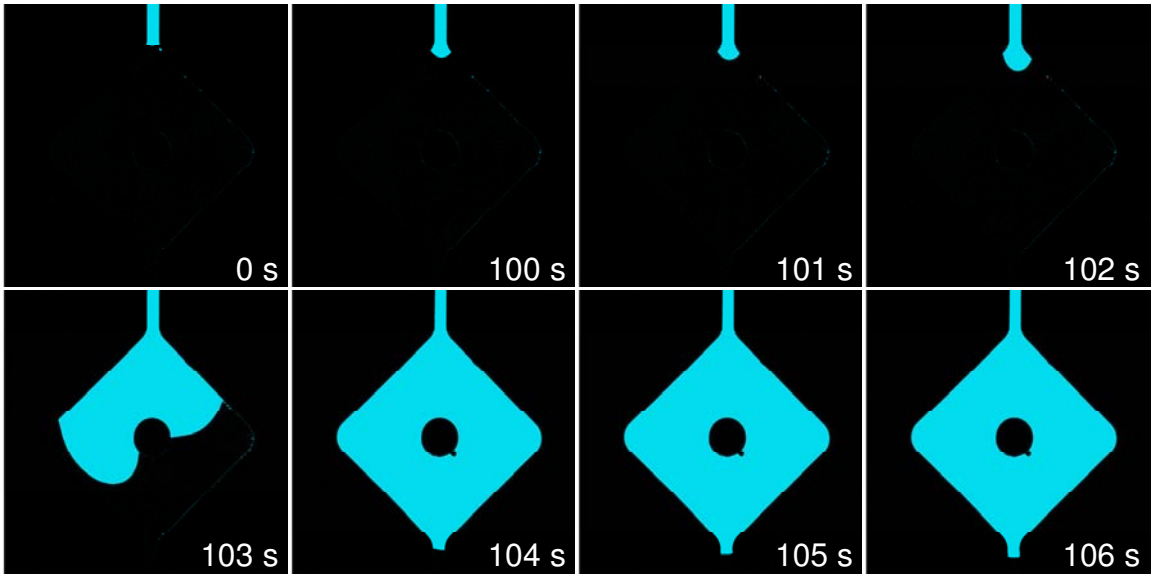

Figure 4.8. Time lapsed confocal images taken of a PDMS micromodel where Alexa Fluor® 488/water (teal) is displacing air. (Pressure driven flow of a non-wetting fluid.)

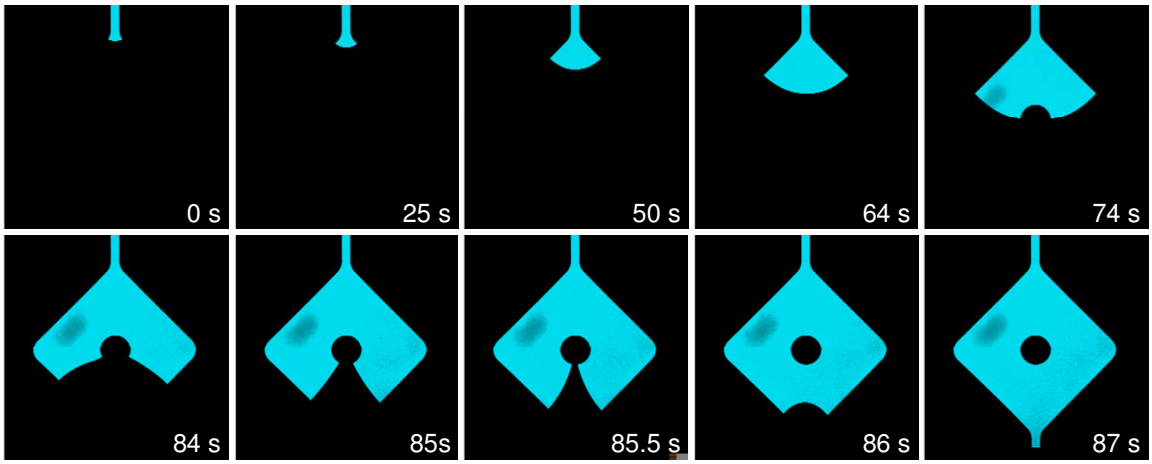

Figure 4.9. Time lapsed confocal images taken of a PDMS micromodel where an aqueous solution of sodium dodecyl sulfate dyed with Alexa Fluor® 488 (teal) is displacing air. (Capillary driven flow of a wetting fluid.)

In order have a static contact angle less than 90°, a surfactant was added to the water. A 10 mM aqueous solution of sodium dodecyl sulfate with 0.1 mg/ml of Alexa Fluor® 488 (teal) displaced air through a PDMS single post micromodel (see Figure 4.9), just as in the previous case with no surfactant. Here, the equilibrium contact angle of the fluid on PDMS was approximately 69° with a surface tension of 39.5 mN/m. Because the water wets the PDMS in this case, the liquid is not pumped through the model; instead it wicks into the model via capillary forces. In this case, the threshold pressure to enter the wide open feature is zero since the equilibrium contact angle is less than 90º. The liquid does not hesitate to enter the channel and does not burst through as quickly, as seen in Figure 4.9. One can also see that the surfactant solution wets the PDMS micromodel more so in this case than pure water, as expected.

4.4. Micromodels Made from Glass

The ultimate goal of this work is to observe liquid-liquid multiphase flow, therefore glass micromodels were fabricated so that a decane/water system could be studied. Upon inspection of these micromodels, it was found that the amorphous silicon layer that was used in bonding the two sides together (as described earlier) made the glass discolored. This discoloration is also believed to influence the fluorescence properties of the Nile Red/decane solution. Initial experiments performed using the glass micromodel samples found that the emission of Nile Red/decane and Alexa Fluor® 633/water were too close to distinguish with the confocal microscope, contrary to what we determined earlier when investigated in a glass capillary. Therefore, so that the two phases could be seen, the water phase was dyed with Alexa Fluor® 488 as shown in Figure 4.10. In this figure, the water dyed with Alexa Fluor® 488 (teal) is displaced by decane dyed with Nile Red (purple) in the entrance well of the micromodel. The configuration of the confocal microscope used for the glass samples is listed in Table 4.3. In this case, the Argon 488 laser line was able to excite both dyes while their emission spectra was separated enough to obtain two distinct signals.

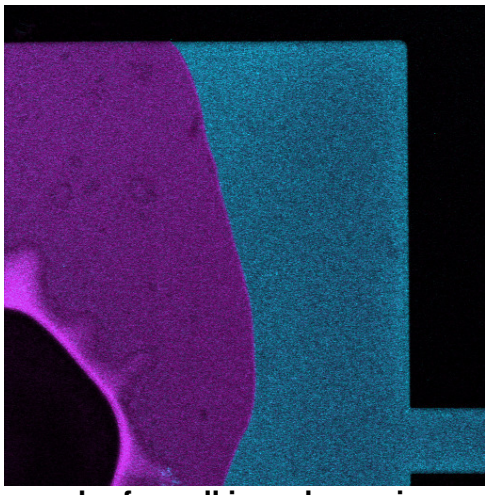

Figure 4.10. Confocal micrograph of a well in a glass micromodel that is filled with Alexa Fluor® 488/water (teal) and Nile Red/decane (purple).

Table 4.3. Configuration of the confocal microscope for imaging Nile Red/decane and Alexa Fluor® 488/water in the glass

Laser 1	Argon 488 at 30% power
Main Dichroic Beam Splitter	HFT 488
Secondary Dichroic Beam Splitter	NFT 545
Channel 2 Emission Filter	BP 505-530
Channel 3 Emission Filter	LP 650

4.4.1. Decane Displacing Water

Initial experiments performed with the glass micromodels involved decane displacing water. The micromodel was flooded with Alexa Fluor® 488/water and inspected to make sure that no air bubbles were present. Next, Nile Red/decane was introduced into the micromodel with the syringe pump pumping at a volumetric flow rate of 0.1 μl/min. An example of decane displacing water in the open rectangular micromodel with no posts is shown in Figure 4.11. In this image, water is initially in the micromodel (teal) and the decane (purple) is forced in. From this image, it appears that decane is the non-wetting phase while water is the wetting phase since the contact angle of decane against the glass micromodel is greater than 90^{o}. This same procedure was used in other micromodel geometries as well. In Figure 4.12 one can see decane (purple) push water (teal) out of the single post micromodel over time. Interestingly, there is a small amount of water that is left behind in the feature. This is a very thin strip of water that bridges between the post and the wall that remains stable over time. Another example of decane displacing water over time is shown in Figure 4.13 for the multipost geometry. Again, there are thin strips of water left behind as the decane fills in the micromodel.

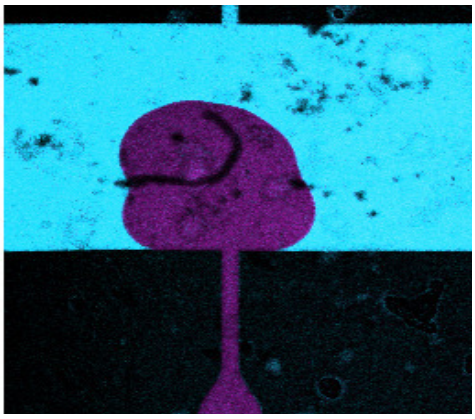

Figure 4.11. Confocal micrograph of Nile Red/decane displacing Alexa Fluor® 488/water in a micromodel. The debris and speckle patterns in the image are fabrication artifacts.

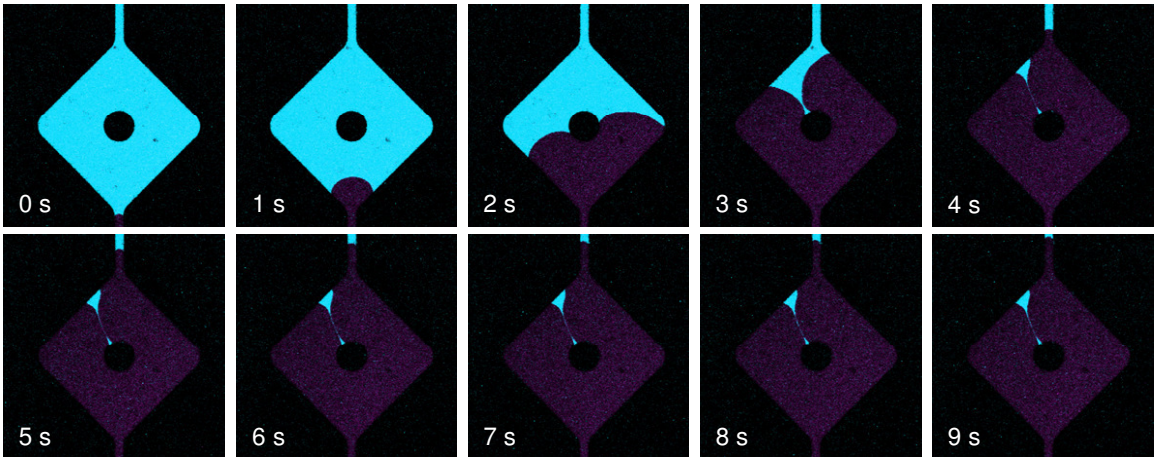

Figure 4.12. Time lapsed confocal images taken of a glass micromodel where Nile Red/decane (purple) is displacing Alexa Fluor® 488/water (teal).

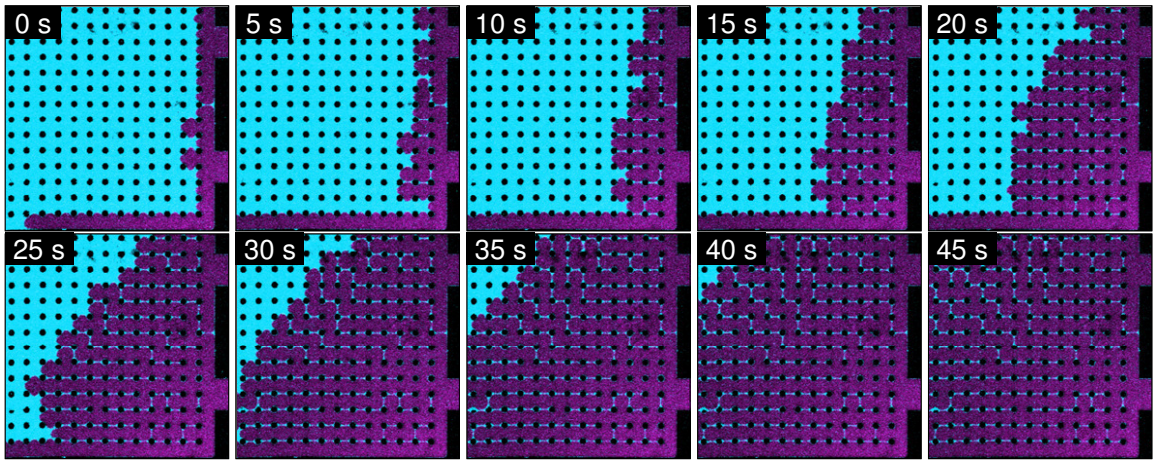

Figure 4.13. Time lapsed confocal images taken of a glass micromodel where Nile Red/decane (purple) is displacing Alexa Fluor® 488/water (teal).

4.4.2. Water Displacing Decane

The opposite experiments were also performed, where water displaced decane in the micromodels. This system is similar to efforts to understand oil recovery in porous media, such as rocks. In this case, the micromodels were initially filled with decane carefully to make sure that no air bubbles were present. Then, water was introduced into the system where it was fed to the micromodels with the use of the syringe pump set to a volumetric flow rate of 0.1 µl/min. In Figure 4.14, Alexa Fluor® 488/water is displacing Nile Red/decane in the single post micromodel, with the same conditions as that in Figure 4.12. In comparing the two examples, one sees that in both it appears that the fluid being introduced is the non wetting fluid due to the fact that the water does not appear to want to coat the glass. Another example of water displacing decane is shown in Figure 4.15. Here, in the four post geometry, the water (teal) flushes through the middle of the feature where there are no obstructions. In the corners of the feature there are drops of decane (purple) left behind. Again, it appears as though the decane is the wetting phase as the water is pushed through. However, there was an interesting observation that was made upon imaging water displacing decane in the rectangular geometry with no posts. As shown in Figure 4.16, as the water enters the feature, it appears to wet the left wall and moves along the edge of the feature until it finally reaches the outlet. This example would lead us to believe that water is the wetting phase in this case.

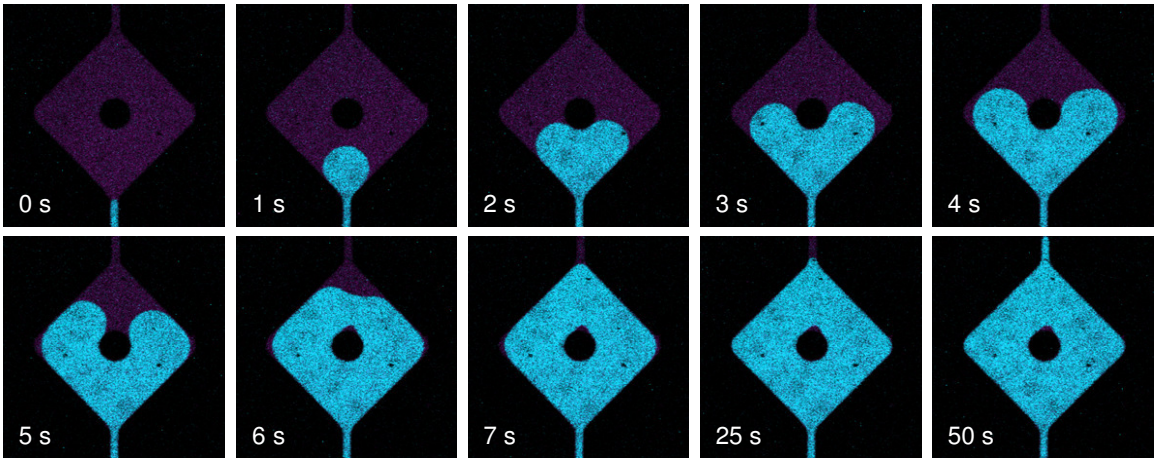

Figure 4.14. Time lapsed confocal images taken of a glass micromodel where Alexa Fluor® 488/water (teal) is displacing Nile Red/decane (purple).

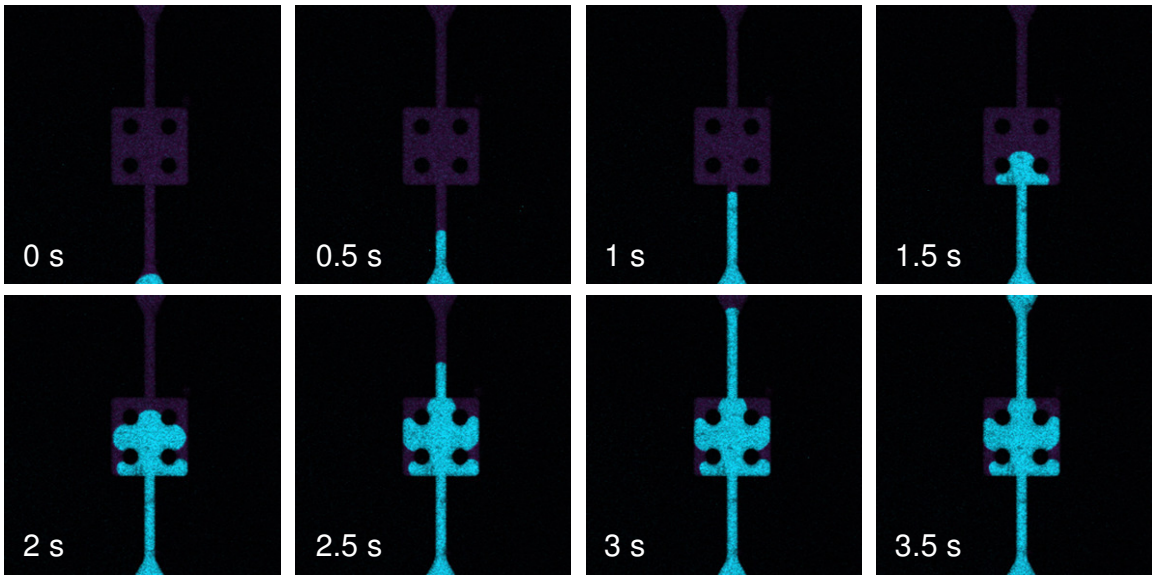

Figure 4.15. Time lapsed confocal images taken of a glass micromodel where Alexa Fluor® 488/water (teal) is displacing Nile Red/decane (purple).

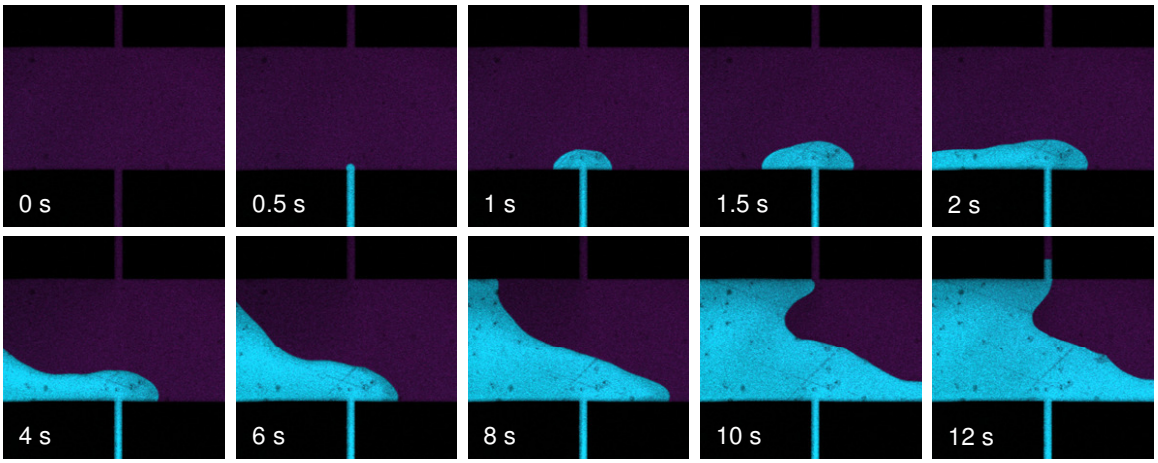

Figure 4.16. Time lapsed confocal images taken of a glass micromodel where Alexa Fluor® 488/water (teal) is displacing Nile Red/decane (purple).

In order to try to determine which liquid phases is the wetting phase in the glass micromodels, confocal images were taken of samples that had previously been used and had been sitting with both liquids present, giving the system time to equilibrate. In Figure 4.17 one can see two different confocal images of decane (purple) and water (teal) in glass micromodels. In Figure 4.17a, the multipost micromodel had initially been filled with water which was displaced by decane. From this image, it appears that the static contact angle of decane is much greater than 90^{o}, meaning that water was the wetting phase. However, in Figure 4.17b, where the single post micromodel had initially been filled with decane and was displaced by water, the water contact angle appears to be much greater than 90^{o}, indicating that decane is the wetting phase. From our data, it seems that the liquid used to initially fill the micromodel, whether it was water or decane, was the wetting liquid. One possible explanation of this is that there may be a thin layer of the

initial fluid coating the walls of the micromodel that is still present once the imbibing liquid is introduced. This may explain why we see inconsistent data in Figure 4.17.

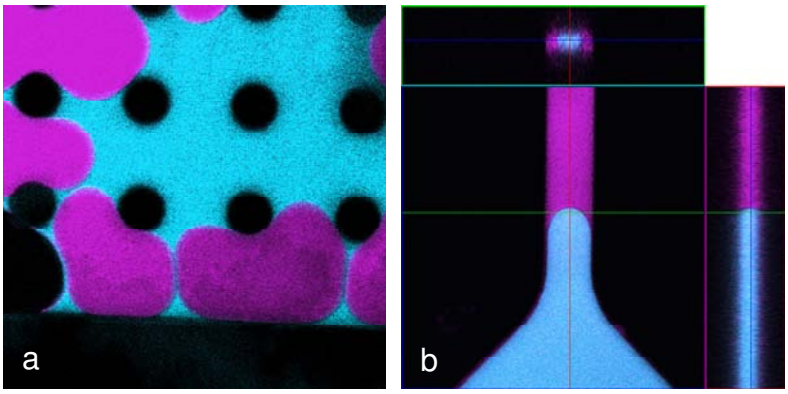

Figure 4.17. Static confocal micrographs of micromodels filled with water (teal) and decane (purple). a) Multipost micromodel that was initially filled with water and was displaced with decane. b) Single post micromodel that was initially filled with decane and displaced with water.

Due to the inconsistency of the data, the surface and interfacial properties of the liquid-liquid system were investigated. The contact angles of decane on glass in a water environment and water on glass in a decane environment were measured. For these experiments, actual micromodels were used to make sure that the glass was the same material as in the confocal experiments. For the water contact angle on glass in a decane environment, a quartz cuvette was filled with decane dyed with Nile Red. An unused micromodel was dropped into the cuvette and rested flat on the bottom. Using a pipette, a single drop of water dyed with Alexa Fluor® 488 was dispensed onto the glass surface and allowed to sit to reach equilibrium. An optical micrograph (see Figure 4.18a) of the drop was taken from the side to allow for the contact angle to be measured. It was found that the water contact angle on the micromodel glass in decane was approximately 80^{o}.

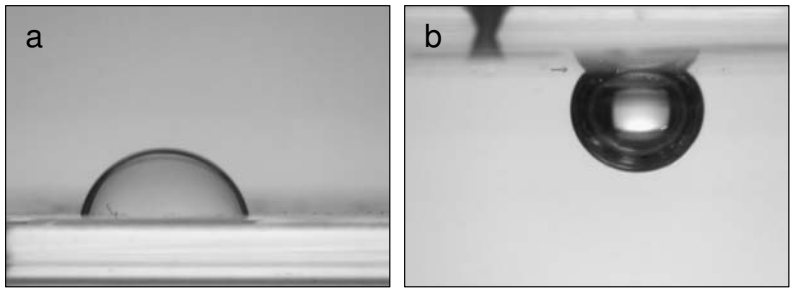

Figure 4.18. a) A water drop sitting on a glass micromodel with decane as the surrounding fluid. b) A decane droplet against a glass mircomodel with water as the surrounding fluid.

For the decane contact angle on glass in a water environment, the cuvette was filled with water dyed with Alexa Fluor® 488. Because decane is less dense than water, a drop of decane will float to the surface. Therefore, an unused micromodel was held just beneath the top surface of the water with the use of a vacuum chuck. A single drop of decane dyed with Nile Red was then injected under the micromodel. An optical micrograph (see Figure 4.18b) of the decane droplet

was taken to determine the contact angle, which was found to be approximately 140^{o}. In theory, these two angles should add up to 180^{o}, however, there may be an inconsistency because two different substrates were used. From these contact angle measurements, it would suggest that water should always be the wetting fluid. However, our results seem to contradict this. This may be explained by the fact that the inside of the micromodels may have different surface properties which we are unable to measure. An amorphous silicon layer is used in the bonding process, which may affect the surface properties of the inside of the micromodels that would not be apparent on the outside surfaces, which is what was used to measure the contact angles. Also, it is possible that when the micromodels were fabricated, they were not uniformly cleaned, which may explain why we see different results in different micromodels. It is suggested that for any future work with glass micromodels such as these, a cleaning process be instituted which will give uniformly clean surfaces and give repeatable consistent data as to which phase is the wetting phase. It is also recommended that the amorphous layer be applied to both the channel and well plates prior to bonding to ensure that all channel surfaces are the same.

4.5. References

Greenspan, P. and S.D. Fowler *J. Lipid Res.* **1985**, *26*, 781-789.

Haines, W.B. *J. Agr. Sci.* **1930**, *20***,** 97–116.

Miller, E.E. and R.D. Miller *J. Appl. Phys.* **1956,** *27*, 324-332.

5. SIMULATING DYNAMIC WETTING OF AN AXISYMMETRIC DROP USING LEVEL-SET METHOD

5.1. Background

In this chapter, we report our efforts in simulating the dynamic wetting of an axisymmetric drop on an aluminum surface using the level-set method or approach. Conventionally, processes such as encapsulation, mold filling, laser welding, brazing, corrosion, and materials processing (e.g., crystal growth, electrodeposition) have been modeled using the ALE (Arbitrary Lagrangian-Eulerian) method (Schunk et al. 2002) coupled with re-meshing to avoid unacceptable mesh distortion (Chen and Evans 2004, and Chen 2004). Though the ALE method can track the interface precisely or sharply, the need for re-meshing when an interface undergoes large deformation significantly increases the computational cost and degrades the accuracy. On the other hand, the level-set approach can handle processes involving large deformation without re-meshing. For example, the level-set method can simulate the dynamic phase-breakup and coalescence processes without any re-meshing at all. Moreover, the level-set method can easily treat moderate surface discontinuities involving surface tension, latent heat, and surface reactions.

As a check of the level set implementation in Goma, a comparison was done between simulation results for a spreading axisymmetric drop and the Blake model input. Figure 5.1 shows the results of this comparison (Mody et al. 2007). The Blake model input into the simulation had a static contact angle of 18.8º, whereas the Blake model fit to the simulation predicted a static contact angle of 32.4º. The error in the static contact angle is ~13.6º or 72.3%.

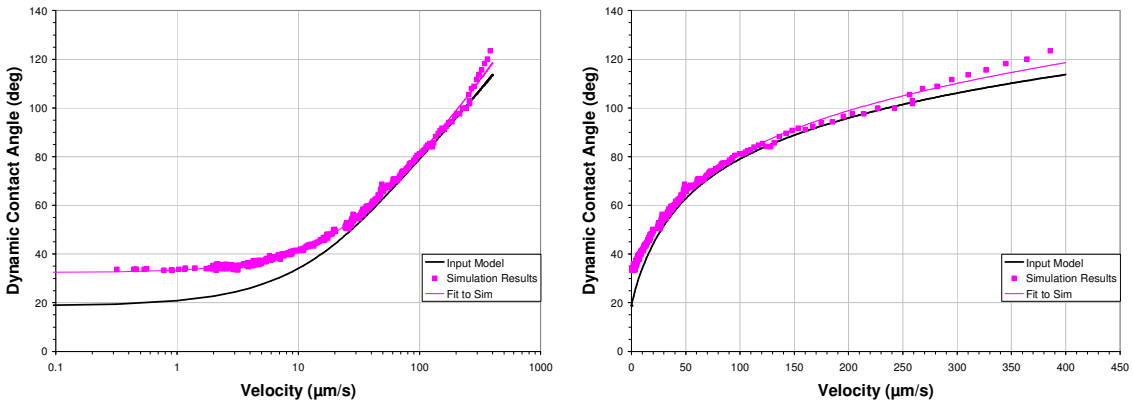

Figure 5.1. Plots comparing the Blake model input parameters input into the drop simulation (dark blue) and what was measured from the simulation (pink). The left plot represents velocity on a logarithmic scale and the right plot represents velocity on a linear scale.

The goal of this work is to strengthen Sandia's multiphase codes by achieving self-consistency between the Blake model input into the simulation and the resulting Blake model extracted from the simulation. First the standard level set method is described in the context of finite elements. Next a method is proposed for reducing the errors in the level set function in the proximity of the

contact line. Finally simulation results are presented for the spreading axi-symmetric sessile drop.

5.2. Methodology

Much of this methodology discussion comes from a recent report by Rao et al. 2008, where the level set method is applied to foam modeling. Here we examine a non-reacting flow of two immiscible fluids, but the techniques are largely the same.

5.2.1. Interface Tracking via the Level Set Method

The level set is a signed distance function, which is a function of space and time, $\phi(x, y, z, t)$. The magnitude of the level set function is the shortest distance from x to any point on the free surface, where the free surface is defined by the level set zero. The sign of level set is used to indicate whether the point x lies inside the material. It should be noted that φ should scale as a distance function, that is, the magnitude of its gradient is unity.

$$\left|\nabla\phi\right| = 1 \tag{5.1}$$

This level set representation of the interface presents numerous advantages. The location of the interfacial curve can be determined exactly from interpolation of the finite element shape functions. In addition, the level set representing function provides immediate information about the normal, *n*, and curvature, *H*, of the interfacial surface via these relations:

$$\begin{aligned} \mathbf{n}_{ls} &= \frac{\nabla\phi}{\left|\nabla\phi\right|} \\ \mathcal{H} &= -\frac{\nabla^2\phi}{\left|\nabla\phi\right|} \end{aligned} \tag{5.2}$$

Because the level set zero

$$\phi(x, y, z, t) = 0 \tag{5.3}$$

is a material surface, it advects with the fluid velocity whereas elsewhere it is unclear how the level set equation evolves. For this reason, we use an advection equation for the entire level set function.

$$\frac{\partial\phi}{\partial t} + \mathbf{u}\cdot\nabla\phi = 0 \tag{5.4}$$

Because advection is only truly applicable at the interface, equation (5.4) distorts the distance function. This necessitates the use of a renormalizing algorithm, which must be run periodically to correct the distance function. Details of the renormalization algorithm can be found below.

5.2.2. Property Evaluation

Notationally, we denote these two sides of the interface as “phase A” and “phase B” and often use “A” and “B” as subscripts on mathematical quantities that are specific to a phase.

The level set method uses continuous equations for both the air and liquid phases, but modulates the material properties based on the level set function. This property modulation occurs via a numerical Heaviside function defined for phase A and B, where the Heaviside functions sum to one.

$$H_A(\phi) + H_B(\phi) = 1 \tag{5.5}$$

In the diffuse interface approach, Heaviside function is regularized so that there is a smooth transition from one phase to another. In this work, we use

$$H_B(\phi) = \frac{1}{2}\left(1 + \frac{\phi}{2} + \frac{\sin\left(\frac{\pi\phi}{\alpha}\right)}{\pi}\right), \quad -\alpha < \phi < \alpha \tag{5.6}$$

where α is defined as the half of the width of the diffuse interface, which is usually taken as about six elements across. Here H_B is zero in phase A, 1 in phase B, and follows equation (5.6) in the diffuse region.

Another useful function related to the Heaviside function is the regularized Dirac delta function, which is defined as

$$\delta_\alpha(\phi) = \frac{dH(\phi)}{d\phi} = \frac{|\phi|}{2\alpha}\left(1 + \cos\left(\frac{\pi\phi}{\alpha}\right)\right), \quad -\alpha < \phi < \alpha \tag{5.7}$$

Where $\delta_\alpha(\phi)$ is large in the diffuse interface zone, and zero elsewhere.

In this problem both phases are incompressible and the continuity equation is given by,

$$\nabla \cdot \mathbf{u} = 0 \tag{5.8}$$

The momentum equation including property modulation is given by,

$$(H_A\rho_A + H_B\rho_B)\left(\frac{\partial \mathbf{u}}{\partial t} + \mathbf{u}\cdot\nabla\mathbf{u}\right) = H_A\nabla\cdot\boldsymbol{\pi}_A + H_B\nabla\cdot\boldsymbol{\pi}_B + (H_A\rho_A + H_B\rho_B)\mathbf{g} \tag{5.9}$$

where both phases are assumed to have a constant viscosity:

$$\begin{aligned}\underline{\underline{\pi_A}} &= \underline{\underline{\tau_A}} + p\underline{\underline{I}} = H_A\eta_A(\nabla u + \nabla u^t)) + p\underline{\underline{I}} \\ \underline{\underline{\pi_B}} &= \underline{\underline{\tau_B}} + p\underline{\underline{I}} = H_B\eta_B(\nabla u + \nabla u^t)) + p\underline{\underline{I}}\end{aligned} \tag{5.10}$$

Additionally there is an additional component of the stress due to the interface. The general form of this capillary boundary condition for constant surface tension, σ, is

$$\mathbf{n}\cdot(\boldsymbol{\pi}_A - \boldsymbol{\pi}_B) = -2\mathcal{H}\sigma\mathbf{n} \tag{5.11}$$

5.2.3. Finite Element Discretization

The phase modulated equations of motion, together with the level set equation, are discretized with the well-known Galerkin finite element method. The unknowns of interest are the velocity vector, pressure, and level set. These fields are approximated with finite element basis function, $N_i(x,y,z)$, and nodal variables, $\mathbf{u}_i$, p_i, and ϕ_i. Bilinear Lagrangian, C_0-continuous, basis functions are used for pressure, while biquadratic basis functions are used for velocity and level set. The velocity vector is expressed in the following manner,

$$\mathbf{u} = \sum_{i=1}^{n} \mathbf{u}_i N_i(x, y, z) \tag{5.12}$$

and pressure and level set are

$$p = \sum_{i=1}^{n} p_i N_i(x, y, z)\ \phi = \sum_{i=1}^{n} \phi_i N_i(x, y, z)\,. \tag{5.13}$$

The approximate variables are substituted in the conservation equation, multiplied by a weighting function, and integrated over the domain. Any second derivatives, such as the divergence of the stress tensor, are integrated by parts, to improve the accuracy of the discretization as shown below. The integration by parts on the momentum equation provides a surface terms that serves as a natural boundary condition if no other conditions are applied at the domain boundaries.

$$R_i^{continuity} = \int_V N_i\left[\nabla\cdot\mathbf{u}\right]dV = 0 \tag{5.14}$$

$$R_i^{momentum} = \int_V (N_i(\rho\frac{\partial\mathbf{u}}{\partial t} + \rho\mathbf{u}\nabla\mathbf{u} - \rho\mathbf{g}) - \nabla N_i\cdot\boldsymbol{\pi})dV + \int_S \mathbf{n}\cdot\boldsymbol{\pi}N_i dS = 0 \tag{5.15}$$

$$R_i^{levelset} = \int_V N_i(\frac{\partial\phi}{\partial t} + \mathbf{u}\cdot\nabla\phi)dV = 0 \tag{5.16}$$

Time derivative are discretized using a first-order backward Euler finite difference method. The resulting weighted residual equations are integrated numerically using Gaussian quadrature.

There exist and inf-sup condition constraining the pressure space to be one order lower than the velocity space, which is termed the LBB condition [Hughes, 2000]. Here, we use quadratic velocity basis functions coupled to linear or bilinear pressure interpolation to satisfy this requirement. This is a computational intensive pair, however, because high order Gaussian quadrature must be used and nodal summations per element increase from four for bilinear to nine for biquadratic. In addition, due to the fact that the continuity equation is the equation for the pressure unknown and contains no pressure, a saddle point problem is created when the discretized matrices are formed. For this reason, direct Gaussian elimination is needed to invert the matrix and solve the unknowns of interest. This approach is taken here, but even for this axisymmetric problem, the resulting cpu times are quite large. An alternate approach is taken in the next chapter where equal order elements and pressure stabilization are used to reduce the computational cost.

5.2.4. Redistancing Algorithm

One distinct aspect of the level set method is that while the level set function might initially have the smooth properties of a distance function, this is not a necessarily preserved by the evolution scheme. It is almost certainly the case that as evolution proceeds it will deviate away from a pure distance function. Indeed sharp gradients might occur at some points in the flow, while very shallow gradients occur in others. A necessary aspect of any level set method, therefore, is a periodic need to redistance or renormalize the level set function back to a distance function. Our decision to renormalize is based upon monitoring the average gradient magnitude of the level function over the interfacial zone. In general, this average gradient is only allowed to vary between 1.25 and 0.75. Outside of this range it will trigger a redistancing procedure.

There are several methods by which this can be done. Sussman and Fatemi [1999] described a redistancing step based upon a separate evolution of the level set field subject to a mass conserving constraint. The Goma algorithm is a more algorithmic approach. The elements that contain the interface can be quickly identified as those whose nodal level set values have differing signs. On these elements, a piecewise linear representation of the interface is constructed. For each node i in the mesh, it is possible to find a minimum distance D_i to this set of facets. Renormalization of the level set nodal unknown is made by the simple assignment:

$$\phi_j^* = sign(\phi_j^0) D_j \tag{5.17}$$

where ϕ_j^0 is the value of the level set function prior to renormalization. Given a sufficient density of facets, this procedure will yield good results as well as being fast and robust. However, it does present the potential for slight, systemic motion of the zero level set contour and a consequent loss of mass. This is especially a problem for lower order (trilinear) interpolation of the level set function. This can be avoided however by introducing a volume constraint. This is accomplished by finding a small change to the distance function, ε, such that the initial and final volumes are the same. The distance function at the end of the renormalization is thus given by,

$$\phi_j = \phi_j^* + \varepsilon \tag{5.18}$$

where ε is found by solving the equation,

$$\int_V H_A^0\left(\phi^* + \varepsilon\right)dV = \int_V H_A^0\left(\phi^0\right)dV \tag{5.19}$$

The superscript on the Heaviside is used here to denote that this is the sharp Heaviside function, that is unity where its argument is positive and zero else where. The left hand side of this equation is the volume of the phase A following the renormalization and the right hand side is the volume before renormalization. By using this adjustment to the nearest point distance, we guarantee that the volume of the phase A after renormalization will be the same as it was before renormalization.

5.3. Modification of the Level-Set Function Near the Contact Line

Other issues, however, may arise from renormalization, however. In fact, the errors shown in Figure 5.1 are due to subtleties in the renormalization procedure. This was first noted by Noble et al. 2001, and can occur any time the contact angle differs significantly from 90˚. This is shown in Figure 5.2.

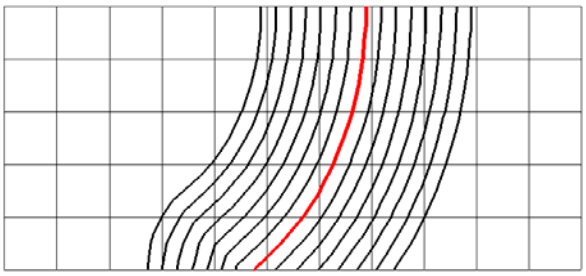

Figure 5.2. A 2-D example of level-set curves without interface extension

The red curve represents the zero level set, indicating the location of the movable interface. Other level curves of the distance function are shown in black. The exact distance from each node in the mesh to the nearest point on the interface was computed. Then the isocontours of the finite element interpolant was rendered for several values of the distance function. It is apparent that the level curves to the right of the zero level set contact the lower boundary with a contact angle that is similar to the contact angle of the interface. The level-set curves to the left the zero level set, however, are significantly different. The contact angles of these curves are all approximately 90º. This is caused by the fact that there is a finite segment of the domain for which the nearest point on the interface is the contact line (or point in this 2D example). In theory, all of these curves have exactly a 90º contact angle. The deviation in Figure 5.2 results from the polynomial basis of the finite element interpolant. The conclusion, however, is that even the exact distance function gives a poor approximation of the contact angle for level-set curves on the non-wetted side (on the left) of the interface. The consequence of this poor approximation is that the calculation of the wetting speed is inaccurate in this region. The Blake boundary condition is applied in the vicinity of the interface along the domain boundary, where the locality is defined by the slip length as part of the Blake model implementation in Goma/Aria. It is directly a function of the dynamic contact angle, which in turn, is a function of the level set along the boundary. Therefore, the inaccurate contact angle in this non-wetted

region corrupts the wetting speed, and results in poor agreement for static contact angles that deviate significantly from 90º.

This issue may be alleviated by computing the distance function differently in the segment of the domain that is nearest to the contact line or point. The goal of this modification is to provide a distance function that more accurately represents the contact angle of the interface on both sides of the interface. Conceptually, we seek a distance function that is consistent with the interface being extended beyond the meshed domain instead of abruptly truncating at the domain boundary. If such an extension were performed the resulting distance function would be modified wherever the nearest point on the interface would lie on this extension. The results of this interface extension is shown in Figure 5.3 below. By comparing these figures we see that the distance function is the same except for the points that are closest to the contact line. Here the level curves no longer contact the boundary at 90º but instead at an angle that is more consistent with the contact angle of the interface. This is expected to result in a more accurate calculation of the wetting speed from the Blake model in this region.

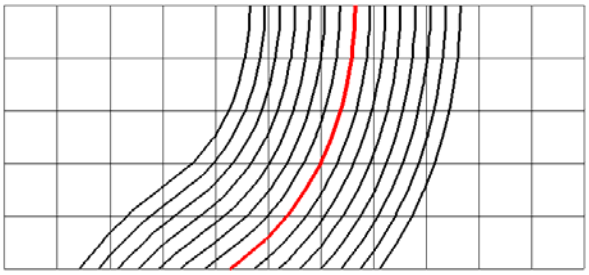

Figure 5.3. A 2-D example of level-set curves with interface extension.

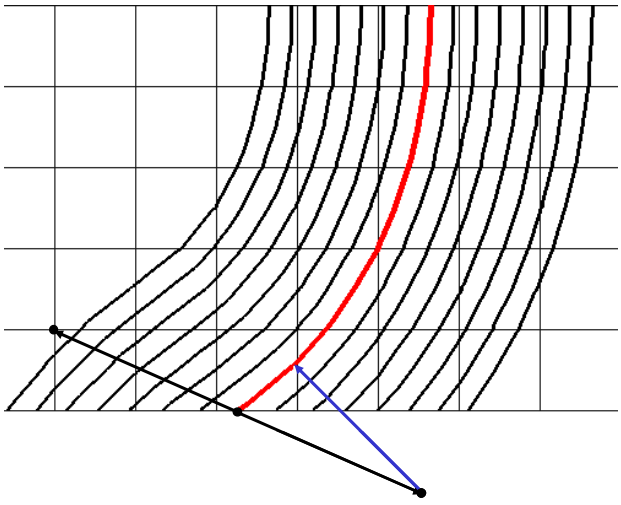

Figure 5.4. Calculation of the modified distance function using interface extension

In practice the modified distance function is calculated as follows. First the traditional nearest point calculation is made, where the distance at every node is found to the nearest point on the interface. If this nearest point, however, lies on the domain boundary, the calculation is

modified. The nodal location is reflected about the contact line or point, and the distance from this reflected point to the nearest point on the interface is then computed. This is shown in Figure 5.4. The resultant distance function value at the marked node is given by the length of the blue line instead of the distance from the node to the contact point. In this way, the explicit extension of the interface is avoided.

This capability was put in Goma to provide better accuracy of the wetting line speed after redistancing the level-set function. This capability has not yet been put into Krino in SIERRA. Care has to be taken near corners in the domain when using this contact extension capability. If the reflected point lies inside the domain, the resulting distance function is likely to be inaccurate. This issue warrants further examination.

5.3. Case Study

To check on (or verify) the correctness of the interface-extension implementation, we simulate the dynamic wetting of an axisymmetric drop of a silicone fluid on an aluminum surface surface to a relatively long time (360 s) and obtain the "equilibrium" (as approximated by the relatively long time of 360 s) contact angle and compare the simulated value with that we input into the Blake wetting model.

5.3.1. Geometry

Figure 5.5 shows the geometry of dynamic wetting of an axisymmetric liquid drop on a surface. Here, the wetting liquid is forced out of a 800 μm diameter pore and then spread onto the aluminum surface.

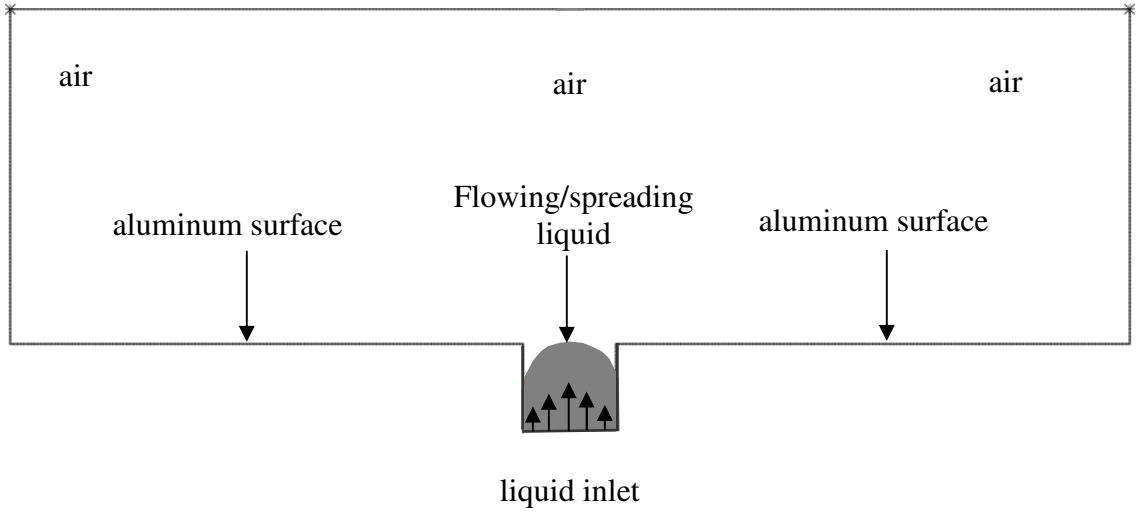

Figure 5.5. Case study geometry – dynamic wetting of an axisymmetric liquid drop on an aluminum surface (liquid is supplied through a 300 μm pore).

5.3.2. Boundary Conditions

The boundary conditions are specified as follows. At the liquid inlet plane, a fully developed parabolic velocity profile is specified. Along the wall of the pore and the mold surface, no slip condition is imposed away from the contact or wetting line. In the vicinity of the contact line, the

following Blake model is employed to specify the contact angle as a function of static contact angle, surface tension, width of the interface wetting region or slip length, and wetting velocity (Blake and De Coninck 2002):

$$V_w(\phi) = f(\phi) V_0 \sinh\{g[\cos\theta_s - \cos\theta_d(\phi)]\} \tag{5.20}$$

or solving for $\cos\theta_d$:

$$\cos\theta_d = \cos\theta_s - \frac{1}{g}\sinh^{-1}\left[\frac{V_w}{fV_0}\right] \tag{5.21}$$

where θ_d and θ_s are, respectively, dynamic and static contact angles; g is a thermally scaled dimensionless surface tension (i.e., $\sigma/2nkT$); V_w is slip velocity at the wall; V_0 is a pre-exponential velocity factor; and f is a localized slip function as defined by

$$U = f(\phi; L) V_W \sinh\left[g\left(\cos\theta_{equil} - \cos\theta\right)\right]$$
$$f(\phi; L) = \begin{cases} 0 & \text{when } |\phi| > L/2 \\ 1 - \dfrac{|\phi|}{L/2} & \text{when } |\phi| \le L/2 \end{cases} \tag{5.22}$$

In Equation 5.22, L is the width of the interface wetting region or simply slip length.

5.3.3. Results and Discussion

Figure 5.6 shows a series of snap shots of shapes of liquid-drop spreading on a surface at various times as computed by level-set method. In this base-case study, the following parameters were used: μ = 3100 mPa-s; ρ = 1.03 g/mL, σ = 21.7 mN/m, V_0=36.5 μm, g = 2.29, θ_s = 18.8°, and L = 198 μm. Numerically, a mesh with an element size of 66 μm and a total of 3717 elements was employed in the computation. With this mesh on a HP xw8400 Workstation, it took approximately 6 days to simulate 30 s of drop spreading on the mold surface. It took approximately 72 days (or 2.4 months) to simulate 360 s of drop spreading. It is interesting and informative to see from Figure 5.6 that the liquid appears to be non-wetting shortly after emerging from the pore (Figure 5.6a) at 0.13 s. However, at about 2.43 s (Figure 5.6b), the drop achieves a neutral position – that is, neither non-wetting nor wetting with a contact angle about 90°. At about 5 s (Figure 5.6c), the liquid is clearly wetting. So, the liquid spreading dynamics changes from non-wetting to wetting, depending on the speed of the contact line. This transition from non-wetting to wetting indicates the flow switching from inertia and viscous force dominating to surface tension dominating.

Figure 5.7 shows the computed dynamic contact angle as a function of wetting speed. The transition from non-wetting to wetting (θ_d = 90°) occurs at a wetting speed of ~ 118 μm/s ($Ca=\mu*V/\sigma$ = 0.017). As expected, the dynamic contact angle increases slowly with wetting

speed in the non-wetting ($\theta_d > 90°$) regime whereas in the wetting ($\theta_d < 90°$) regime, θ_d decreases rapidly with V_w, and indeed precipitously as V_w approaches zero or vanishes.

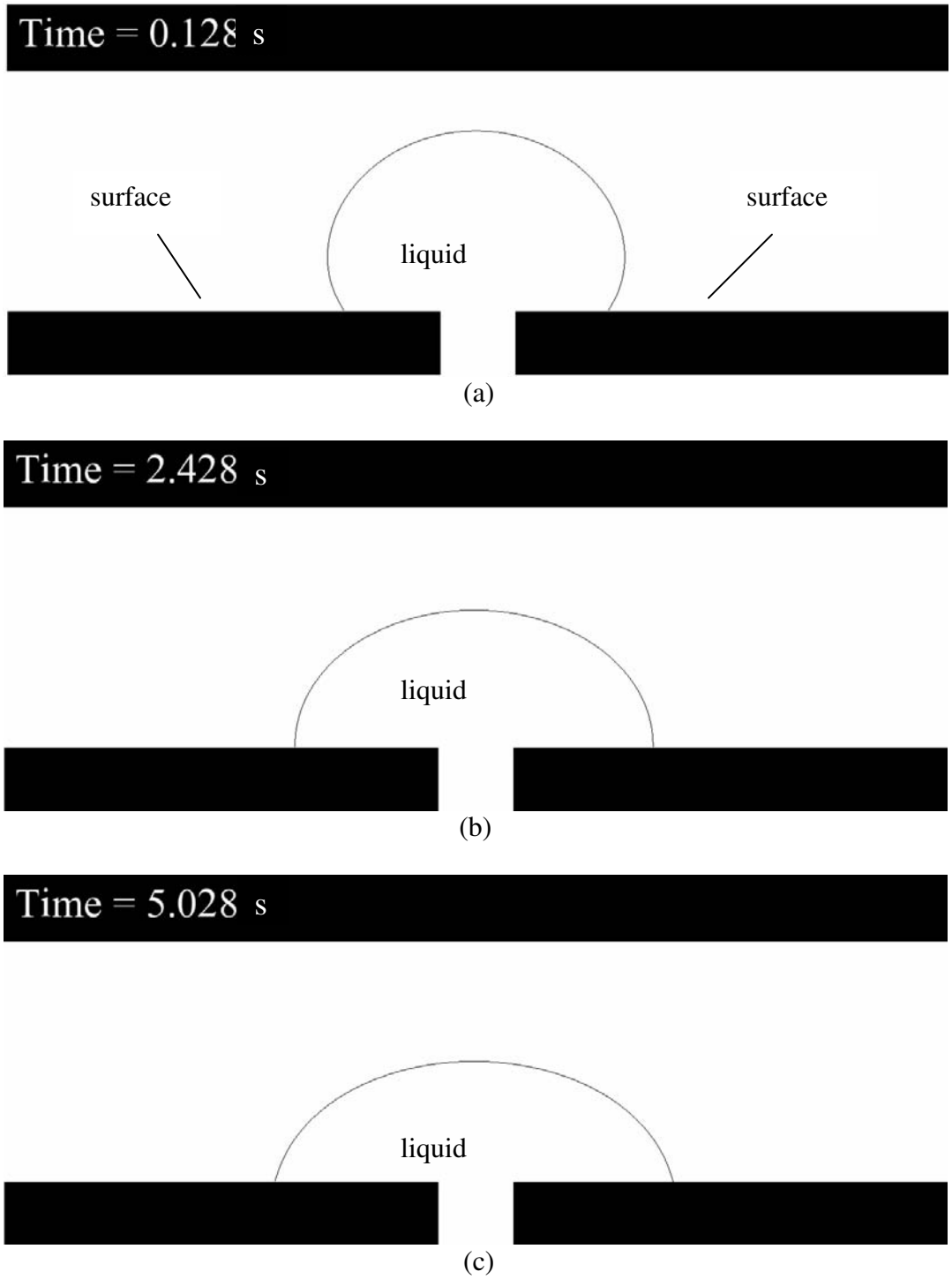

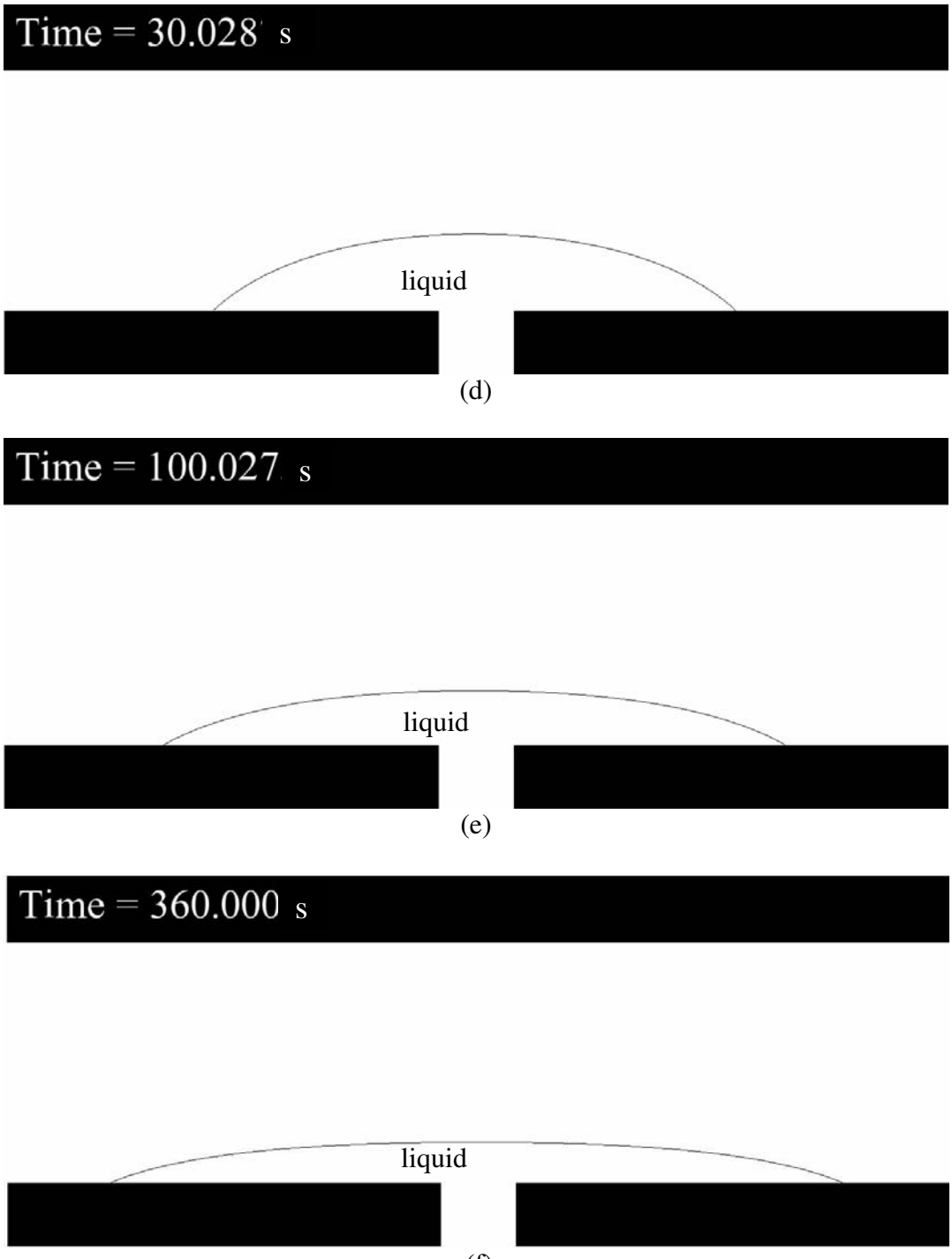

Figure 5.6. Liquid drop spreading on a surface computed by level-set method (a) t = 0.13 s; (b) t = 2.43 s; (c) t = 5 s; (d) t = 30 s; (e) t = 100 s; (f) t = 360s.

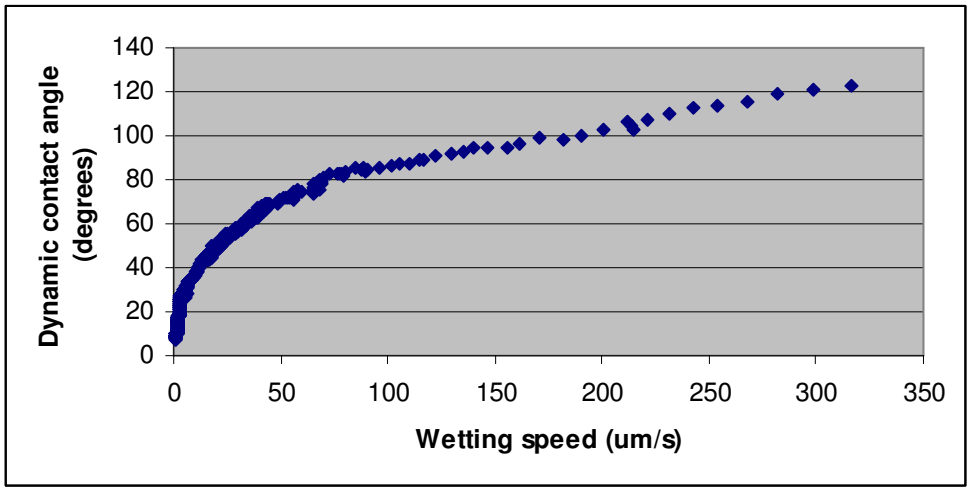

Figure 5.7. Computed dynamic contact angle as a function of wetting speed (conditions are those of the base case).

Figure 5.8 shows sample image analyses for contact-angle determination from the computed drop shapes for the non-wetting, neutral, and wetting regimes. The image analyses were automated by software developed in the present work. The slight differences between the left and right contact angles are mostly likely due to precision limitation in the software.

As can be seen from Equations 5.5 and 5.6, slip length or the width of the interface wetting region has a direct effect on the computed dynamic contact angle as shown in Figure 5.9. As expected, the dynamic contact angle converges (i.e., variation becomes indiscernible) when the slip length is sufficiently long. Specifically, when the slip length is 10-elements long (or about 660 μm) or longer, the difference in computed dynamic contact appears to be very small. Similarly, Figure 5.10 shows effect of slip length on computed long-time or "equilibrium" contact angle, determined from the static contact angle parameter when fitting to a Blake model. Table 5.1 further quantifies the effect of slip length. As in the case of dynamic contact angle, when the slip length is 10-elements long or longer (> 660 μm), the computed long-time or "static" contact angle reaches an equilibrium value of about 21°.

As compared with the static contact angle of 18.8° input to the Blake model used in our simulation, the computed value of 21° (which gives a mere 11.7% discrepancy, down from 72.3% prior to the level-set correction near the contact line) indicates that the level-set approach coupled with an interface or contact extension scheme can accurately simulate processes involving dynamic wetting lines such as an axisymmetric drop spreading on a solid surface. This is a significant improvement over what simulations predicted prior to this change, lending more accuracy to simulation predictions.

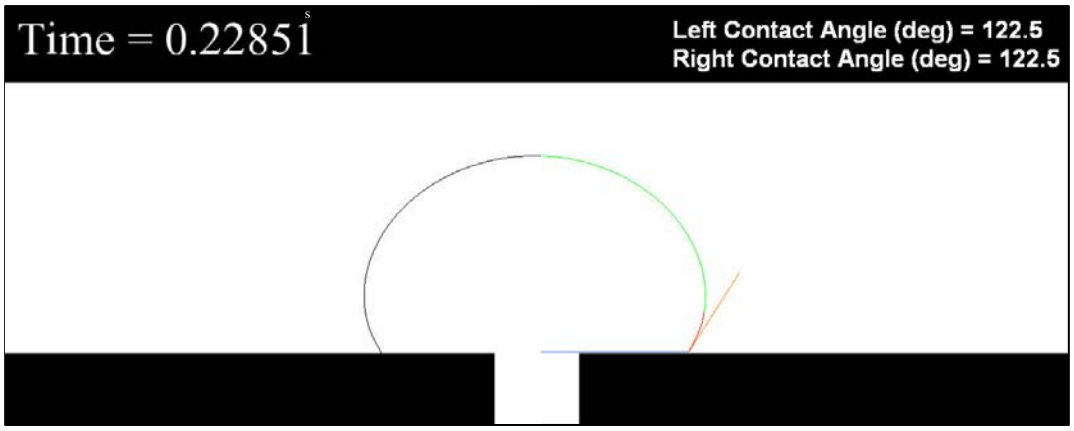

(a)

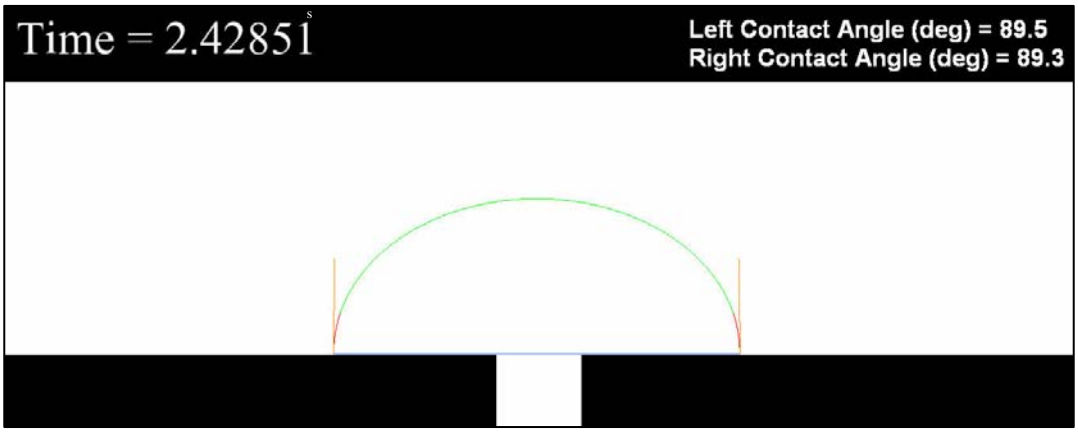

(b)

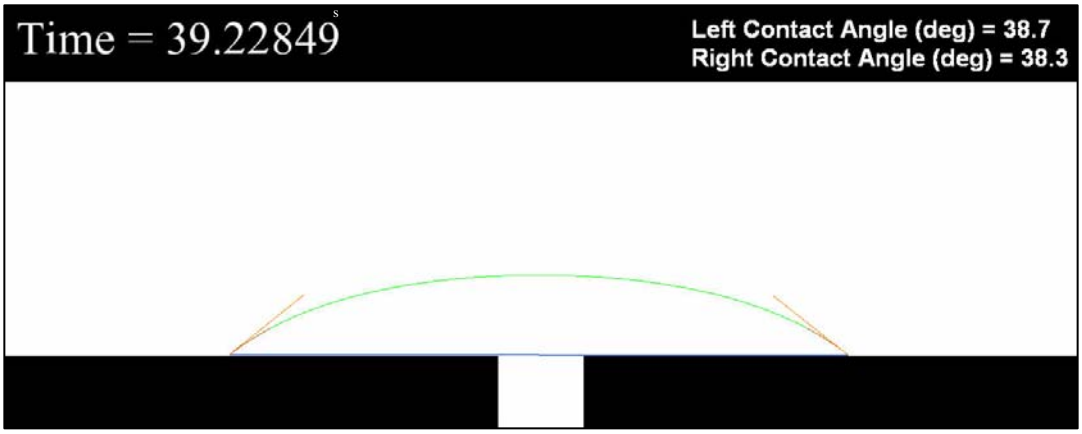

(c)

Figure 5.8. Sample image analyses for contact-angle determination (a) non-wetting drop; (b) neutral drop; and (c) wetting drop.

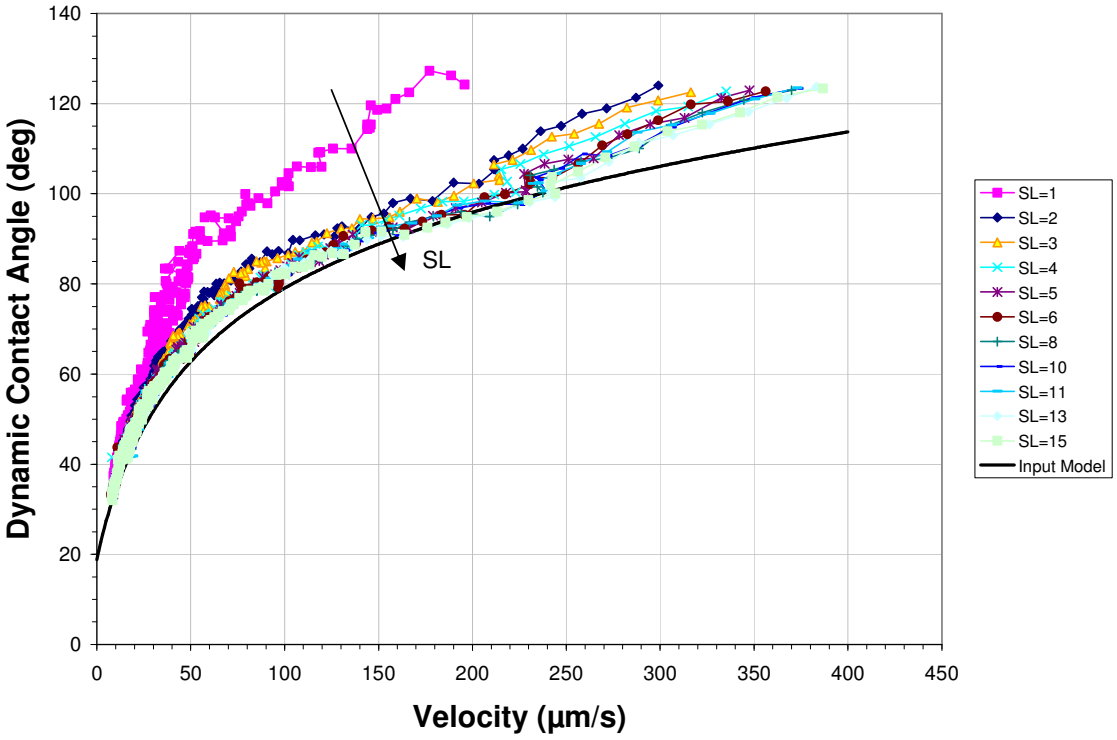

Figure 5.9. Dynamic contact angle versus velocity – effect of slip length.

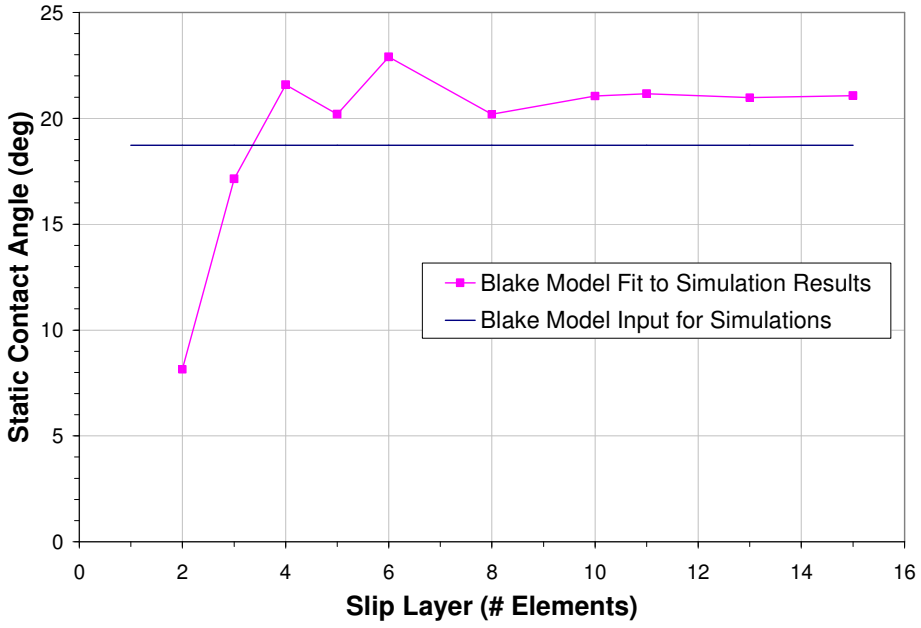

Figure 5.10. Effect of slip length on computed long-time or "equilibrium" contact angle.

Table 5.1: Effect of slip length on computed long-time or "static" contact angle.

Slip Length	Static Contact Angle from Blake Model Fit (deg)
2	8.14
3	17.14
4	21.58
5	20.20
6	22.90
8	20.19
10	21.05
11	21.17
13	20.97
15	21.07

5.4. References

T. J. Blake and J. De Coninck, "The influence of solid-liquid interactions on dynamic wetting", *Advances in Colloid and Interface Science*, **96**, p. 21 – 36 (2002).

K. S. Chen, "Multi-dimensional modeling of atmospheric copper-sulfidation corrosion on non-Planar substrates", *Sandia Technical Report*, SAND2004-5878 (2004).

K. S. Chen and G. H. Evans, "Multi-dimensional multi-species modeling of transient electrodeposition in LIGA microfabrication", *Sandia Technical Report*, SAND2004-2864 (2004).

T. J. R. Hughes. *The Finite Element Method*. Dover Publications, New York, USA, 2000.

D., Jacqmin, (1995) "Three Dimensional Computations of Droplet Collisions, Coalescence, and Droplet/Wall Interactions Using a Continuum Surface-Tension Method," AIAA-95-0883.

D. R. Noble, T. A. Baer, and R. R. Rao, "Contact angle specification in level set simulations", presentation at APS-DFD Meeting (November 2001).

R. R. Rao, L. A. Mondy, H. K. Moffat, D. R. Noble, P. K. Notz, D. B. Adolf, and T. A. Baer, "Foam process models", Sandia Report, SAND 2008-6094 (2008).

L. Mondy, R. Rao, C. Brooks, D. Noble, R. Givler, A. Sun, A. Kraynik, T. Baer, E. Wilkes, P. Notz, M. Hopkins, A. Grillet, R. O. Cote, J. N. Castañeda, D. Adolf, J. Mahoney, K. Berchtold, M. Brooks, A. Graham, "Wetting and Free Surface Flow Modeling for Potting and Encapsulation," Sandia Report, SAND2007-3316 (2007).

P. R. Schunk, P. A. Sackinger, R. R. Rao, K. S. Chen, T. A. Baer, D. A. Labreche, A. C. Sun, M. M. Hopkins, S. R. Subia, H. K. Moffat, R. B. Secor, R. A. Roach, E. D. Wilkes, D. R. Noble, P. L. Hopkins, and P. K. Notz, "GOMA 4.0 - a full-Newton finite element program for free and moving boundary problems with coupled fluid/solid momentum, energy, mass, and chemical species transport: user's guide", *Sandia Technical Report*, SAND2002-3204 (2002).

Chapter 6

Reduced Order Modeling of Two Fluids in a Micromodel

6.1 Background

The focus of this work is simulating two-phase flow in micromodels. The micromodels used for experiments are thin and uniform with depth except for the presence of top and bottom walls. Full 3D simulations of two phase flow are computationally intensive, so we were motivated to consider reduced order simulations.

The thin depth of the micromodel is similar to the well-studied Hele Shaw cell. By averaging pressure and velocity over the depth of a Hele Shaw cell, analytical expressions for the displacement of a wetting fluid with a nonwetting fluid may be determined (3). In the micromodel case, analytical expression are much more difficult to obtain. The fluids of interest do not perfectly wet the micromodel surfaces, and the geometry is much more complex. However, analyses of the Hele Shaw cell do provide methods for reducing the order of two phase flow simulations in micromodels.

In this work, a finite element model is developed that captures the forces acting with depth while doing calculations in only two dimensions. The parameter space is explored to determine the dynamics of a wetting fluid displacing a nonwetting fluid within a micromodel. Simulations are compared to experimental results in order to validate the model and determine values of unknown parameters.

6.2 Methodology

This section contains a description of the methods used to model the flow in thin micromodels using Aria. Much is in common with the methodology presented in chapter 5, but that work was performed in goma using mildly different techniques.

6.2.1 Level set method for interface tracking

The level set (LS) method is used to track the location of the interface between two fluids. The LS method uses a signed distance function ϕ that evolves with time to define the interface and the regions of each fluid. In Aria, the two phases, A and B, are denoted by negative and positive values of ϕ, respectively, and the interface is defined by zero values of ϕ. The motion of the level set is given by

$$\frac{\partial \phi}{\partial t} + \vec{v} \cdot \nabla \phi = 0 \ , \tag{6.1}$$

where $\vec{v}$ is the fluid velocity. The normal of the interface is determined from

$$\vec{n}_{ls} = \frac{\nabla \phi}{|\nabla \phi|} \ , \tag{6.2}$$

and the curvature is

$$\mathrm{H} = -\nabla \cdot \vec{n}_{ls} \ . \tag{6.3}$$

The interface region spans a finite width across which the the fluid phases smoothly transition. This transition is controlled by a heaviside function which is given by

$$\mathrm{H}_B(\phi) = \frac{1}{2}\left(1 + \frac{\phi}{2} + \frac{\sin\left(\pi\phi/\alpha\right)}{\pi}\right), -\alpha < \phi < \alpha \ , \tag{6.4}$$

where the subscript B refers to phase B, and α is the half-width of the interface. The value of α is typically set equal to 6 times the element length. The heaviside functions for phase A and B sum to unity.

6.2.2 Finite element discretization

The continuity equation for the fluid is given by

$$\left(\mathrm{H}_A\rho_A + \mathrm{H}_B\rho_B\right)\nabla \cdot \vec{v} = -\mathrm{H}_A\left(\frac{\partial \rho_A}{\partial t} + \vec{v} \cdot \nabla \rho_A\right) - \mathrm{H}_B\left(\frac{\partial \rho_B}{\partial t} + \vec{v} \cdot \nabla \rho_B\right) \ , \tag{6.5}$$

For simulations in this work, the densities of each phase are constant, so the continuity equation simplifies to $\nabla \cdot \vec{v} = 0$.

The momentum equation for the level set formulation is given by

$$\left(\mathrm{H}_A\rho_A + \mathrm{H}_B\rho_B\right)\left(\frac{\partial \vec{v}}{\partial t} + \vec{v} \cdot \nabla \vec{v}\right) = \mathrm{H}_A\nabla \cdot \pi_A + \mathrm{H}_B\nabla \cdot \pi_B \ , \tag{6.6}$$

where $\pi_{\mathbf{i}}$ is the stress tensor of phase i.

The jump in stresses across the interface is proportional to the surface tension σ, which is given by

$$\vec{n} \cdot (\pi_{\mathbf{A}} - \pi_{\mathbf{B}}) = -2\mathrm{H}\sigma\vec{n} \,, \tag{6.7}$$

where H is calculated from the level set function from Equation 6.3 and $\vec{n}$ is the level set normal determined by Equation 6.2.

The continuity, momentum, and level set equations are discretized with the Galerkin finite element method (4). The basis functions and weighting functions, which are chosen to be equal to the basis functions, are bilinear langrangian and C_0-continuous. The weak formulation of the continuity, momentum, and level set equations are then given by

$$R_i^{cont} = \int_V N_i \left[\rho \nabla \cdot \vec{v} + \left(\frac{\partial \rho}{\partial t} + \vec{v} \cdot \nabla \rho \right) \right] dV = 0 \,, \tag{6.8}$$

$$R_i^{mom} = \int_V N_i \left(\rho \frac{\partial \vec{v}}{\partial t} + \rho \vec{v} \cdot \nabla \vec{v} - \nabla \left(\vec{e} N_i \right) : \pi \right) dV + \int_S \vec{n} \cdot \pi \cdot \vec{e} N_i dS = 0 \,, \tag{6.9}$$

and

$$R_i^{LS} = \int_V N_i \left(\frac{\partial \phi}{\partial t} + \vec{v} \cdot \nabla \phi \right) dV = 0 \,. \tag{6.10}$$

Terms with second derivatives are integrated by parts. The first-order backward Euler method is used to discretized time derivatives. The resulting set of equations is numerically integrated by Gaussian quadrature.

The LBB condition requires that the basis functions for the pressure be one order less than those for the velocity. However, this constraint can be avoided by using a suitable pressure stabilization. In simulations for this work, a modified PSPP stabilization method is used for the continuity equation (2). The stabilized residual for the continuity equation is given by

$$R_i^{cont,PSPP} = R_i^{cont} + \sum_{elem} \tau_{PSPP} \Delta t \left(N_i - \pi N_i \right) \left(\frac{\partial p}{\partial t} - \pi \frac{\partial p}{\partial t} \right) dV \,, \tag{6.11}$$

where

$$\pi \frac{\partial p}{\partial t} = \int_{V_e} \frac{\partial p}{\partial t} dV \Big/ \int_{V_e} dV \,. \tag{6.12}$$

Time derivatives of the pressure are used so that the method works with two phase simulations that have a jump in pressure across the interface due to surface tension. This method is suitable for large scale problems because of its computationally efficiency and simple implementation. Also, no special treatment is necessary at boundaries.

For the momentum equation, the streamline upwinding Petrov-Galerkin (SUPG) stabilization method is employed to reduce pressure oscillations for cases when the

Reynolds number is larger than 10. The basis functions for the momentum equations are modified to

$$W_i = N_i + \sum_{elem}^{M} \tau_{SUPG}\left(h_{elem}\right) \frac{\vec{v} \cdot \nabla N_i}{|\vec{v}|} \ , \tag{6.13}$$

where h_{elem} is the element size. The modified weight functions are applied to terms in the momentum equation with derivatives less than two. This may lead to errors for simulations where the stresses are the dominant forces, as is the case for Stokes flow. However, the errors vanish as the element size goes to zero.

The transport equation for the LS is hyperbolic. To improve computational efficiency, a Taylor-Galerkin upwinding term is included in the weak form of the LS equation. The modified weak form is given by

$$\int_V N_i \frac{\phi_i^{n+1} = \phi_i^n}{\Delta t} dV = -\int_V N_i \left(\vec{v}^{n+1} \cdot \nabla \phi_i^{n+1}\right) dV - \frac{\Delta t}{2} \int_V \left(\vec{v}^n \cdot \nabla N_i\right) \left(\vec{v}^n \cdot \nabla \phi_i^n\right) dV \ . \tag{6.14}$$

The effect of the upwinding term is to improve LS function behavior away from the interface.

As the LS function evolves due to fluid motion, it may deviate from a true distance function, and inaccurate solutions may result. Sharp gradients of the function lead to inaccurate computations, and shallow gradients increase the width of the interfacial region. The LS function is renormalized during simulations when the average value of $\nabla\phi$ within the interface region is outside the range of 0.75 to 1.25.

The renormalization algorithm is straightforward and robust. The first step of the algorithm is to locate the interface by identifying elements that contains at least one node with a negative value of ϕ and one node with a positive value of ϕ. The interface location is estimated from these nodes using a piecewise linear construction. For the rest of the mesh, the minimum distance to the interface D_i is found for each node. The renormalized LS function nodal value is specified from

$$\phi_i^* = \text{sign}(\phi_i^0) D_i \ , \tag{6.15}$$

where ϕ_i^0 is the previous value of the LS function at node i.

The final step of the renormalization process is to ensure that mass is conserved. A constant correction term is added to each ϕ_i^* that is specified from the mass conservation equation

$$\int_V H_A^0 \left(\phi^* + \epsilon\right) dV = \int_V H_A^0 \left(\phi^0\right) dV \ . \tag{6.16}$$

The renormalized values of the LS function are given by $\phi_i = \phi_i^* + \epsilon$.

6.2.3 Numerical mesh and boundary conditions

Meshes are generated by Cubit using the trimesh feature to create triangles for 2D finite element simulations. The element size is set so that there are approximately 6 elements across the narrowest channel of the micromodel.

During the micromodel experiment, a syringe pump was used to push water into the micromodel. When the interface reached the narrow channel just upstream of the main region, the pump was turned off but remained connected. Thus, the upstream pressure may have decreased as water filled the micromodel. Because the exact boundary condition at the inlet is unknown, we examine two different sets of boundary conditions. The first is fixed pressure, and the second is a slip boundary condition. The slip boundary adjusts the pressure so that a specified inlet velocity is approached. Along the walls the Blake boundary condition is applied. Away from the interface, the no-slip boundary condition holds. At the interface, the slip velocity is given by

$$v = -v_w \sinh(g(\cos\theta_{static} - \cos\theta) \ , \tag{6.17}$$

where v is the velocity of the contact line, v_w and g are empirical parameters, and θ_{static} is the static contact angle.

6.2.4 Solvers

The finite element formulation for continuity, momentum, and level sets results in a set of coupled, nonlinear equations. The continuity and momentum equations are solved simultaneously, but the LS equations are solved independently. The equations are linearized by the Newton-Raphson method. The matrix problems are solved using one of the Krylov based solvers available in Trilinos (5).

6.2.5 Reduced order model development

The micromodels used for this project are uniform with depth except for the top and bottom surfaces. They share a similar geometry with Hele-Shaw cells where the in-plane dimensions are much greater than the depth. To mesh the geometry in three dimensions, a very fine grid spacing is required because of the small depth. Thus, we were motivated to consider two dimensional meshes where the forces due to the vertical dimension are included as depth-averaged terms.

As an example, consider the dynamics of two fluids located between a pair of infinite plates with length L, depth h, and infinite width. The only forces acting on the fluids are the capillary force acting on the interface and the viscous force. The capillary force per unit width is given by

$$F_{capillary} = 2\sigma\cos\theta \ , \tag{6.18}$$

where σ is the interfacial tension between the two fluids and θ is the moving contact angle. Assume that the Blake model (Equation 6.17) applies to the motion of the interface along the walls. If Equation 6.17 is rearranged to give the value of θ, the capillary force per width is then

$$F_{capillary} = 2\sigma(-\frac{1}{g}\text{arcsinh}(\frac{v}{v_w}) + \cos\theta_{static}) \ . \tag{6.19}$$

Assuming that fluid motion can be described by Poiseuille flow, the velocity averaged over the depth is given by

$$v = \frac{h}{12\mu}\frac{F_{viscous}}{L} \tag{6.20}$$

where $F_{viscous}$ is the viscous force per width (1).

The capillary and viscous forces are implemented in Aria simulations. The viscous force is simply a body force acting everywhere in the void space. The capillary force is applied within a narrow region where the level set function is equal to zero in much the same way that the Blake condition is applied along specified walls.

6.3 Results

6.3.1 Validation of reduced order model

To test the validity of the reduced order model, a simulation of two fluids in a 1D slot was performed in Aria. Model parameters were set so that the viscous and capillary forces are of the same magnitude for a large range of contact angles. The length of the slot is 0.05 cm, the gap height is 0.003 cm, surface tension is 0.5 dyn/cm, viscosities are 0.0089 and 0.000181 g/(cm sec) with densities 0.997 and 0.0012 g/mL. Blake parameters are given by g =1, v_w = 0.4 cm/s, and static contact angle equal to 69 degrees.

By setting the capillary (Equation 6.19) and viscous (6.20) forces equal the predicted average velocity in the slot is determined. The viscous force due to the less dense fluid is neglected. The average velocity decreases as water fills the slot because the viscous force increases. The predicted velocities at interface location equal to 0.01 and 0.05 cm are 0.13 and 0.084 cm/s, respectively.

Figure 6.1 shows the average velocity over time for the slot flow, as the interface moves along the slot. The velocity fluctuates considerably, but the time averaged velocity is very close to the predicted value. This suggests that approximating the entire flow field as Poiseuille is reasonable, despite the nearly uniform flow field near the interface.

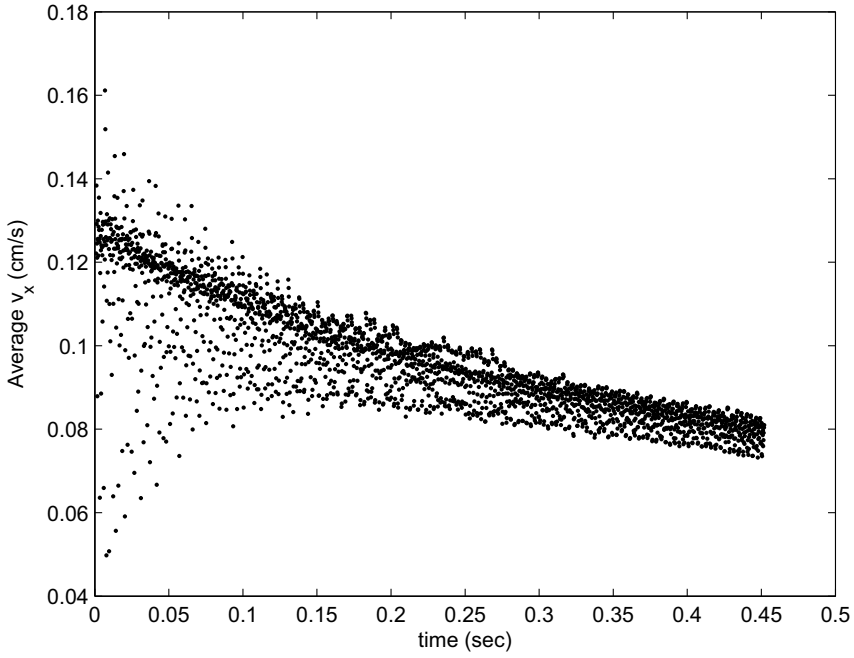

Figure 6.1. Average velocity in a slot for g=1 and v_w=0.4 cm/s in a slot with gap height equal to 0.003 cm. The two fluids are water and air with a static contact angle of 69 degrees.

6.3.2 Comparison with micromodel experiments

Slip boundary conditions

Experimental conditions are difficult to implement numerically because the boundary conditions are not well understood. Water was pumped by a syringe pump through plastic tubing until it reached the micromodel. Once the air/water interface line reached the inlet for the micromodel, the pumped was turned off but remained connected to the micromodel. In simulations, we examine the effects of two different sets of boundary conditions: zero pressure gradient across the system and a slip velocity condition at the inlet.

Figure 6.2 shows the velocity and interfacial area over time for the experiment. Interfacial area is determined by assuming 90 degree contact angles along the top and bottom walls. The flow rate of water into the micromodel is very slow for the first 40 seconds of the experiment. From 40 to 80 seconds, the rate increases approximately linearly, and then jumps to very large values between 80 and 85 seconds. Water is filling the downstream side of the post where the side walls are converging during this time. Finally, the flow rate slows dramatically as the interface approaches the outlet

channel. The interfacial area and the flow rate are not directly proportional with constant value, as would be expected if the flow was driven primarily by capillary action.

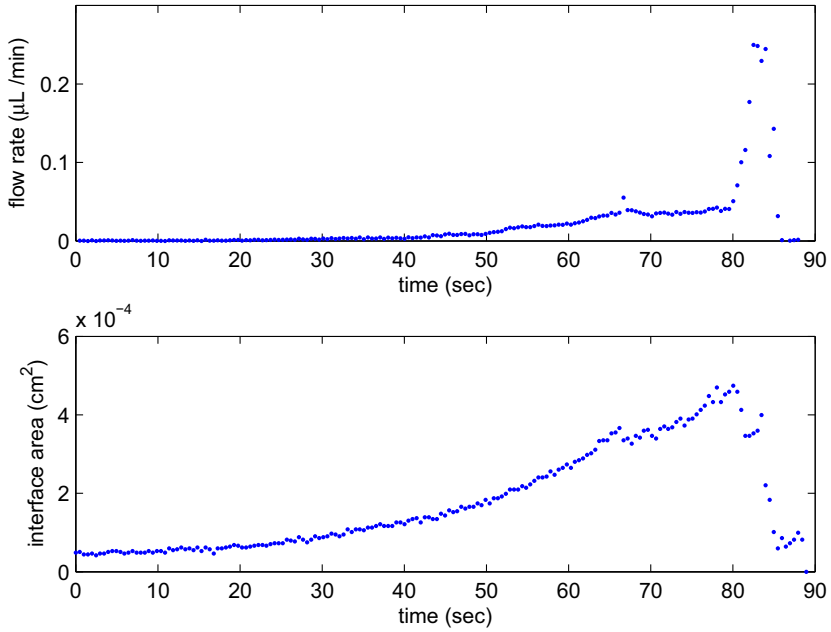

Figure 6.2. Flow rate of water (upper) and interfacial area (lower) in single post experiment determined from 2D images of water in the micromodel.

For simulations using the slip velocity boundary condition, the slip velocity is set so that the flow rate is 0.1 microL/min (the pumping rate before the pump was turned off). Figure 6.3 shows the flow rate of water into the single post system using a slip boundary condition of the form $\frac{1}{\beta}(v - v_{slip})$. The value of β is adjusted to observe its affect on the flow rate during filling. As β decreases, the pressure boundary condition is more strongly imposed to drive force the specified inlet velocity, or the flow rate. For the smaller values of β, the flow rate approaches the specified flow rate, and the flow rate is more steady with time. Water starts to fill the downstream half of the system between interface locations 4 and 5, and a jump in flow rate is observed for all values of β. The greatest relative jump in flow rate occurs for larger values of β, suggesting that a fixed pressure value at the inlet may achieve better agreement with the experiment.

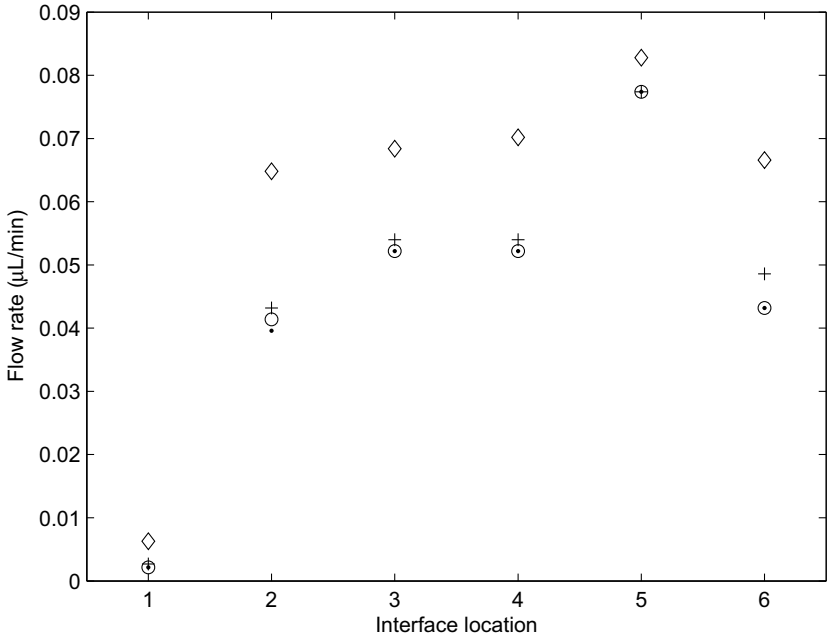

Figure 6.3. Flow rate calculated at the inlet for the single post as water fills the micromodel for beta = 0.1, 0.01, 0.001, and 0.0001 (point, circle, plus, and diamond, respectively).

Analysis of Blake parameters

The Blake model is assumed to hold along the walls of the micromodel, but not all model parameters are known. The values of σ and θ_{static} were measured experimentally. Because of the rapid rate of relaxation of a water droplet on PDMS, experiments to determine Blake parameters are not feasible. Thus, comparisons of simulations to the micromodel filling experiment are used both to validate the model and to infer the values of g and v_w in Equation 6.17. The experimental results used as the basis of comparison are the filling time of the experiment and the maximum contact line velocity.

Figure 6.4 shows the time to fill the micromodel chamber for series of simulations using different values of v_w. For these results, the value of g is set equal to one. Thus, the physical meaning of v_w is clear; it is the maximum contact line velocity. For v_w equal to 0.006, the fill time approaches the experimentally measured time of approximately 90 seconds.

The capillary force along the depth direction appears to be the dominant driving forces in the experiment because the flow rate increases as the interfacial area increases. Using Equation 6.19, we can estimate the magnitude of this force. The simulation

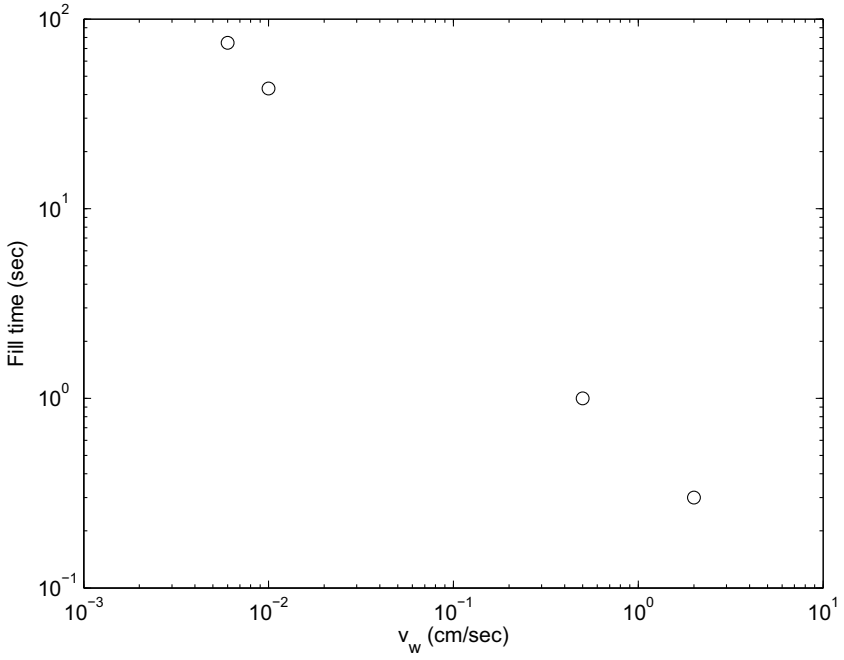

Figure 6.4. Time to fill the micromodel as a function of v_w for g=1.

using $v_w = 0.006$ and $g = 1$. shows reasonable agreement with the experimental time to fill the micromodel. We also assume that the velocity at zero capillary force should be kept constant. Several pairs of values of g and v_w that produce zero force at the same velocity are used for simulations. Figure 6.5 shows the magnitude of the capillary force as a function of the contact line velocity for three pairs of values of g and v_w. Away from the static contact angle, the magnitude of the force diverges for different parameter values. This divergence may lead to large changes in flow rates as the fluids try to return to static contact angles.

In the experiment, the velocity near the outer walls when the contact line reaches the converging walls of the channel increases significantly. We estimate that the maximum velocity reaches 0.03 cm/s, and from Figure 6.2 the flow rate exceeds 0.2 μL/min. Table 6.1 shows some results from varying the values of g and v_w in the simulations. The maximum flow rate increases slightly with increasing values of g, but it is much smaller than the experimentally observed value. The merge y-location is the distance from the centerline of the post in the flow direction to the interface along the left wall at the time step just before the left and right interfaces merge at the downstream side of the post. The differences again are small and much less than observed experimentally (approximately 0.06 cm), see Figure 6.6.

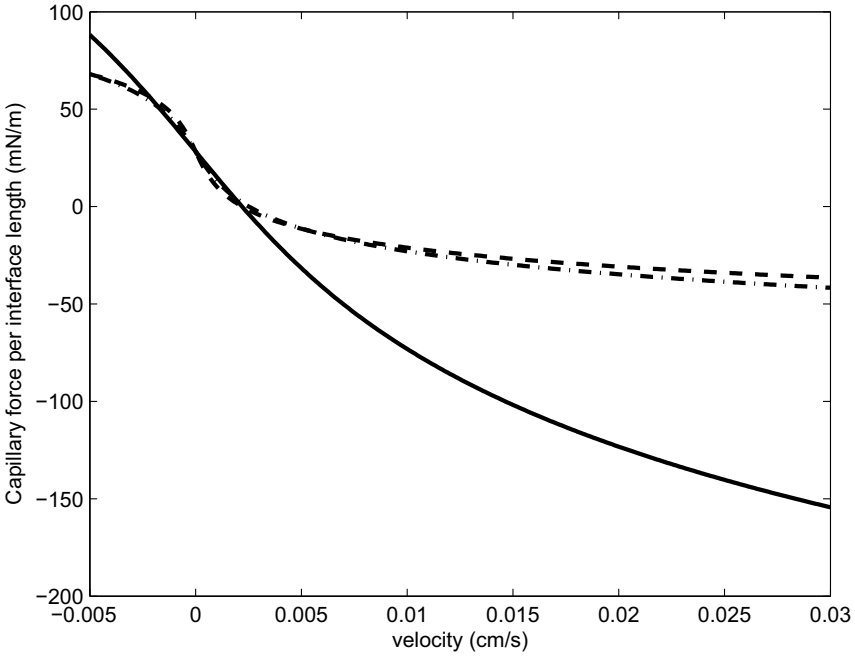

Figure 6.5. Capillary force as a function of contact line velocity for g and v_w equal to 1 and 0.006 (solid), 4.26 and 0.001 (dash-dot), and 5.61 and 0.0006 cm/s (dash).

Micromodel depth

Two observations suggest that in-plane (x-y plane) capillary forces are of nearly the same magnitude as the depth capillary force (z-direction). First, there is a large difference between the ratio of flow rate to interfacial area for the diverging (upstream of the post) and converging (downstream of the post) walls; 10 and 1000, respectively. Second, the interface is essentially pinned on the downstream side of the post as water fills the converging wall area. In the results of the previous section, no set of Blake parameters was able to accurately match the experimentally observed filling pattern, shown in Figure 6.6. Thus, we consider the effect of the gap height, the distance

Table 6.1. Results from varying g and v_w. *sets 22, 21, and 23, respectively.*

case	g	v_w (cm/s)	max flow rate (μL/min)	merge y-location (cm)
1	1.0	0.006	0.046	0.013
2	2.0	0.003	0.050	0.017
3	4.26	0.001	0.050	0.012

between the top and bottom walls. The micromodel is constructed from PDMS, a flexible material that could have a larger depth than specified or could possibly expand during the experiment.

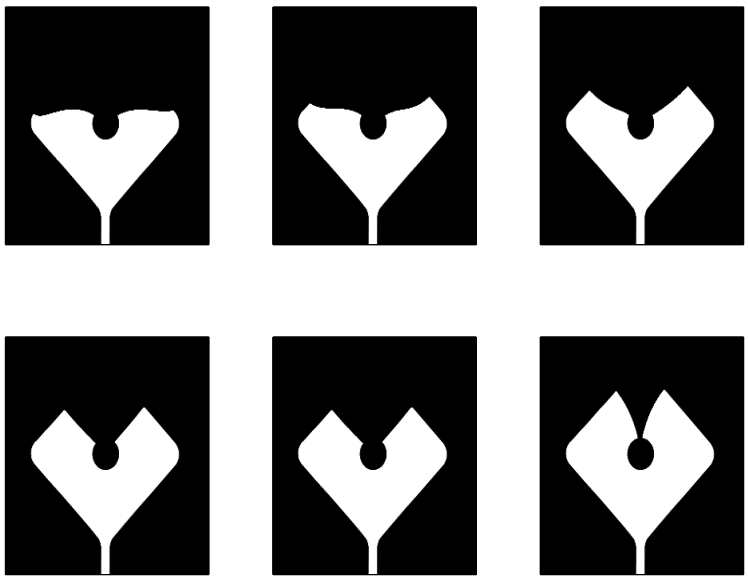

Figure 6.6. Experimental images from times 82, 82.5, 83, 83.5, 84, and 84.5 seconds.

Simulations were performed with gap heights equal to the specified value 2 and 3 times the specified value. The Blake parameter values were $g = 1$ and $v_w = 0.006$. Figure 6.7 shows the shape of the interface just before the post is completely wetted for gap heights equal to 0.003 and 0.006 cm, respectively. Note that for gap height = 0.009 cm, water was not able to enter the main chamber due to insufficient capillary force. If the Blake parameters were adjusted, water would be able to enter the chamber, but additional simulations were not performed.

The flow rate for the simulation in the right side of Figure 6.7 is shown in Figure 6.8. The flow rate does not match the experiment very well, but the trends of the flow rate are present. The flow rate increases with time until the interface first reaches the post. Then the flow rate plateaus until the interface reaches the corners at the side of the micromodel. After this, the flow rate increases rapidly until the interface reaches the outlet channel and it nearly stops.

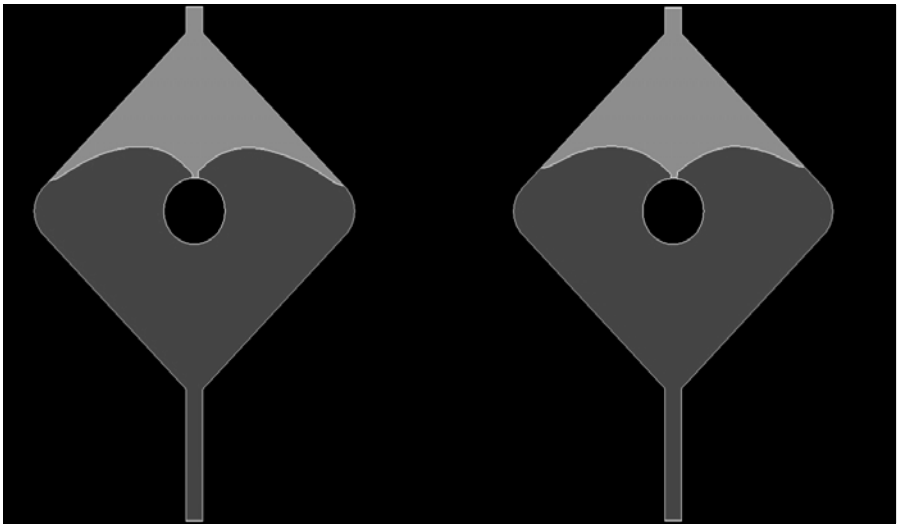

Figure 6.7. Interface shape just before completely wetting the post for g=1 and v_w = 0.006 cm/s and for gap height equal to 0.003 cm (left) and 0.006 cm (right).

6.4 Conclusions

A reduced order finite element model has been developed for simulating two-phase flow in thin micromodels. The reduced order model was compared to a full 2D simulation and the results demonstrate the accuracy of the new model. The parameter space of the model was investigated to understand the impacts of the unknown parameters.

Results were compared to a single experiment. More than one experimental data set would be helpful for comparison to simulation. Also a more full characterization of the experimental conditions including upstream and downstream pressure and accurate measurements of the micromodel depth during filling would enable more focused comparisons to simulations. Experimentally measuring values of Blake parameters would be helpful in order to determine the validity of the model. It may be possible to find a set of values for Blake parameters such that the experimental observations are matched. However, we run into numerical problems with extreme values of g. Finally, a more thorough analysis of the inlet boundary condition including transient pressure will be performed to better understand the experimental conditions.

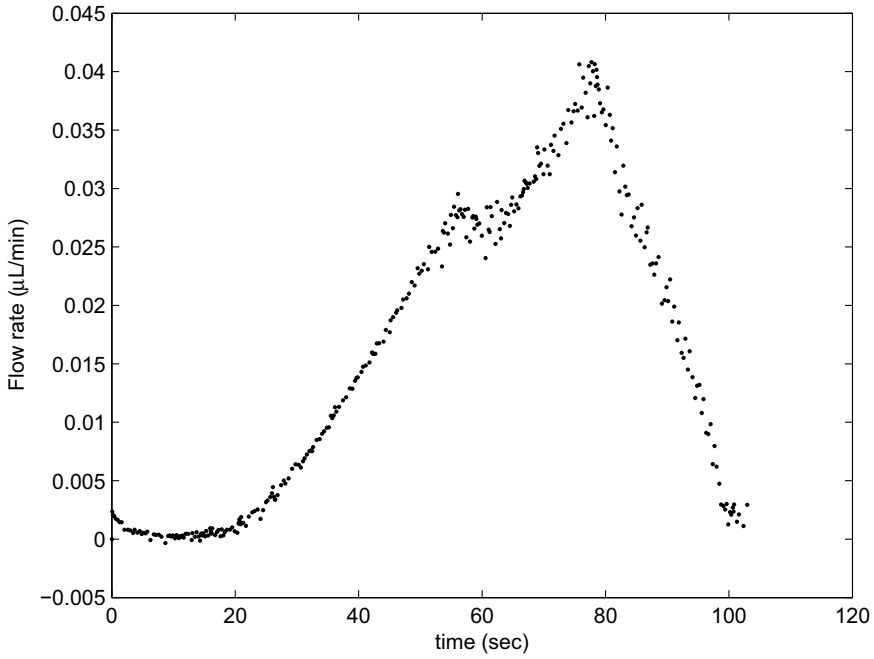

Figure 6.8. Flow rate over time for simulation with g=1, $v_w = 0.006$, and gap height equal to 0.006 cm. *set24.e*

References

[1] Bico, J. and Quere, D., "Self-propelling slugs", J. Fluid Mech. **467**, 101-127, 2002. 6.2.5

[2] Dohrmann, C.R. and P.B. Bochev, "A stabilized finite element method for the Stokes problem based on polynomial pressure projections" , Int. J. Num. Meth. Fluids, **46**, (2004), 183-201. 6.2.2

[3] Park, C.W. and G.M. Homsy, "Two-phase displacement in Hele Shaw cells: theory", J. Fluid Mech., **139** 291-208, 1984. 6.1

[4] Hughes, T.J.R. *The Finite Element Method*, Dover Publications, New York, USA, 2000. 6.2.2

[5] Trilinos, 2008. 6.2.4

Chapter 7

Full Newton Lattice Boltzmann Method for Time-Steady Flows Using a Direct Linear Solver

7.1 Background

The original LDRD proposal stated that lattice Boltzmann (LB) methods were to going to be used to model the multiphase flow in microporous media. This was later switched to the finite element method as described in the previous two chapters. Nonetheless significant enhancements to LB were achieved during the first two years of this project and are described in these last two chapters.

In lattice Boltzmann (LB) models, the evolution of fluid flows is formulated in terms of a discrete probability function, $f_j(\mathbf{x}, t)$, corresponding to the probability that there are particles at the nodal locations traveling with the discrete velocity $\mathbf{e}_j = c\,\mathbf{w}_j$, where the computational speed is c. This probability evolves according to the discrete Boltzmann equation, which can be expressed as

$$f_j(\mathbf{x} + \Delta x\,\mathbf{w}_j, t + \Delta t) = f_j(\mathbf{x}, t) - \frac{1}{\tau}\left[f_j(\mathbf{x}, t) - f_j^{eq}(\mathbf{x}, t)\right] + F_j, \tag{7.1}$$

when the standard BGK collision operator is introduced. This is the standard lattice BGK (LBGK) equation. Here, τ, is the non-dimensional relaxation time, F_j is the contribution due to the applied force, and f_j^{eq} is the equilibrium distribution. The fundamental, repeated steps in a LB code are: macroscopic quantities (such as velocity) are determined from moments of the arriving f_j, these quantities are used to calculate the associated equilibrium distributions, f_j^{eq}, and the discrete Boltzmann equation is used to perform the "collision" and subsequent "streaming" of the modified f_j to the neighboring nodes. Appropriate choices for F_j, f_j^{eq}, and even the collision operator can provide a variety of physics. See Ref. (1) for more background of the lattice Boltzmann method and its application.

While typical LB formulations operate by evolving the flow in time, there is no apparent reason why this approach should be taken in solving steady flows. In the work to follow we show how steady, single-phase flows can be solved directly from the steady

form of Eq. (7.1), using Newton's method. Similar methods were employed by Tolke et al.(2) and Mavriplis(3). In Ref. (3), Newton's method was also employed for the non-linear system of equations. A number of iterative schemes were examined, and it was determined that a multigrid solver was highly efficient. Ref. (2) also used a multigrid iterative solver. It was noted, however, that multigrid solvers involve prolongation and restriction on a geometrical basis, and therefore are not applicable, to problems with high complexity.

In the current work, a simpler, but equally effective method is used. The linear system of equations that are formed at each Newton iteration is solved using a general direct solver designed for sparse, banded matrices. The cost of the simulations is shown to scale super-linearly with the number of unknowns as compared to quadratically for the standard LB scheme. These results show that the time-steady LB equations can be solved efficiently using a "black box" direct solver. These methods are applicable to arbitrary geometries, in contrast to the nested mesh requirement of multigrid solvers. Thus, standard linear solver packages may be employed to improve the efficiency of time-steady LB simulations by multiple orders of magnitude.

7.2 Methodology

7.2.1 Newton's method for time-steady LBGK

We are interested in simulating steady, single-phase flow and consider the pressure and velocity to be the independent variables as proposed by He and Luo(4). These macroscopic quantities are determined from the following moments:

$$p(\mathbf{x}) = c_s^2 \sum_i f_i(\mathbf{x}) \tag{7.2}$$

and

$$\rho\, u_\alpha(\mathbf{x}) = c \sum_i f_i(\mathbf{x})\, w_{i\alpha}, \tag{7.3}$$

where c_s is the speed of sound, and ρ is a specified density. For this model, the equilibrium distribution can be expressed as

$$\begin{array}{rl} f_i^{eq}(\mathbf{x}) = & (1/c)^2\, A_{\sigma(i)}\, p(\mathbf{x}) + (1/c)\, B_{\sigma(i)} w_{i\alpha}\, \rho\, u_\alpha(\mathbf{x}) \\ & +(1/c)^2\, C_{\sigma(i)}\, w_{i\alpha} w_{i\beta}\, \rho\, u_\alpha(\mathbf{x}) u_\beta(\mathbf{x}) \\ & +(1/c)^2\, D_{\sigma(i)}\, \rho\, u_\alpha(\mathbf{x})\, u_\alpha(\mathbf{x}) \end{array} , \tag{7.4}$$

where the coefficients are classified based on the length of $\mathbf{w}_j$. Specifically, the classes are

$$\sigma(i) = \begin{cases} 0 & i = 0 \\ 1 & i = 1,3,5,7 \\ 2 & i = 2,4,6,8 \end{cases} , \tag{7.5}$$

and the associated coefficients are

$$\begin{array}{llll} A_0 = \varsigma^2 - \frac{5}{3} & & D_0 = -\frac{2}{3} & \\ A_1 = \frac{1}{3} & B_1 = \frac{1}{3} & C_1 = \frac{1}{2} & D_1 = -\frac{1}{6} \\ A_2 = \frac{1}{12} & B_2 = \frac{1}{12} & C_2 = \frac{1}{8} & D_2 = -\frac{1}{24} \end{array} , \tag{7.6}$$

where $\varsigma = c/c_s$, and the choice $\varsigma = \sqrt{3}$ is common in the literature. He and Luo(4) have shown how their model, using the unsteady form of the discrete Boltzmann equation, recovers the Navier-Stokes equations to leading order, with viscosity

$$\nu = \frac{(2\,\tau - 1)}{6}\frac{\Delta x^2}{\Delta t}. \tag{7.7}$$

Holdych et. al.(5) have additionally derived the leading truncation error of the model for unsteady flows and confirmed their results with benchmark flow simulations. This model formulation is well-suited for directly solving steady flows, as shown below.

To directly solve for a steady, single-phase flow, we employ Newton's method to solve for the discrete probability functions which satisfy the time-steady form of the discrete Boltzmann equation. To this end, it is convenient to express the nodal residual of the time-steady LBGK equation as

$$R_i(\mathbf{x}) = f_i(\mathbf{x}) - \frac{1}{\tau}\left[f_i(\mathbf{x}) - f_i^{eq}(\mathbf{x})\right] + F_i - f_i(\mathbf{x} + \Delta x\ \mathbf{w}_i). \tag{7.8}$$

This system of non-linear equations is solved via Newton's method by an iterative process. An improved approximation of the particle distribution function is obtained at each iteration according to,

$$f_i^{k+1}(\mathbf{x}) = f_i^k(\mathbf{x}) + \Delta f_i(\mathbf{x}), \tag{7.9}$$

where the update, $\Delta f_i(\mathbf{x})$ is found by solving the linear system of equations,

$$\left[\frac{\partial R_i(\mathbf{x})}{\partial f_j(\mathbf{x})}\right]\Delta f_i(\mathbf{x}) = -R_i(\mathbf{x}), \tag{7.10}$$

where $\frac{\partial R_i(\mathbf{x})}{\partial f_j(\mathbf{x})}$ is the Jacobian matrix. Forming the Jacobian matrix requires the partial derivatives of the equilibrium distribution with respect to each component of the particle distribution function:

$$\begin{array}{rl} \frac{\partial f_i^{eq}(\mathbf{x})}{\partial f_j(\mathbf{x})} = & (1/\varsigma)^2 A_{\sigma(i)} + B_{\sigma(i)}\, w_{i\alpha} w_{j\alpha} \\ & +(2/c)\, C_{\sigma(i)}\, w_{i\alpha} w_{i\beta} w_{j\alpha} u_\beta(\mathbf{x}) + (2/c)\, D_{\sigma(i)}\, w_{j\alpha} u_\alpha(\mathbf{x}) \end{array} . \tag{7.11}$$

The remaining contributions to the Jacobian matrix are found from

$$\frac{\partial R_i(\mathbf{x})}{\partial f_i(\mathbf{x} + \Delta x\ \mathbf{w}_i)} = -1 \tag{7.12}$$

and

$$\frac{\partial R_i(\mathbf{x})}{\partial f_j(\mathbf{x})} = \begin{cases} \frac{1}{\tau}\left(\frac{\partial f_i^{eq}(\mathbf{x})}{\partial f_j(\mathbf{x})} - 1\right) + 1 & j = i \\ \frac{1}{\tau}\frac{\partial f_i^{eq}(\mathbf{x})}{\partial f_j(\mathbf{x})} & j \neq i \end{cases} . \tag{7.13}$$

Boundary conditions at a fluid/solid interface are approximated with the "bounce-back" boundary condition. This condition is implemented at a fluid node at a location $\mathbf{x}$ near the solid interface by imposing that a streamed probability, $f_i(\mathbf{x} + \Delta x\ \mathbf{w}_i)$, traveling in the direction of the solid, $\mathbf{w}_i$, bounces back to the fluid node at $\mathbf{x}$, traveling in the opposite direction, $-\mathbf{w}_i$. By equating $f_i(\mathbf{x} + \Delta x\ \mathbf{w}_i)$ with the reflected probability $f_{-i}(\mathbf{x})$ associated with the direction, $-\mathbf{w}_i$, the residual is replaced with the bounce back residual:

$$R_i^{bb}(\mathbf{x}) = f_i(\mathbf{x}) - \frac{1}{\tau}\left[f_i(\mathbf{x}) - f_i^{eq}(\mathbf{x})\right] + \Delta t\, F_i - f_{-i}(\mathbf{x}) \quad (\mathbf{x} + \Delta x\ \mathbf{w}_i = solid). \tag{7.14}$$

The Jacobian for this residual is

$$\frac{\partial R_i^{bb}(\mathbf{x})}{\partial f_j(\mathbf{x})} = \begin{cases} \frac{1}{\tau}\left(\frac{\partial f_i^{eq}(\mathbf{x})}{\partial f_j(\mathbf{x})} - 1\right) + 1 & j = i \\ \frac{1}{\tau}\frac{\partial f_i^{eq}(\mathbf{x})}{\partial f_j(\mathbf{x})} - 1 & j = -i \\ \frac{1}{\tau}\frac{\partial f_i^{eq}(\mathbf{x})}{\partial f_j(\mathbf{x})} & j \neq i \quad j \neq -i \end{cases} . \tag{7.15}$$

In summary, Newton's method for time-steady LBGK involves iteratively applying Eq. (7.9), where the update is found by solving the linear system of equations given in Eq. (7.10). The RHS of the equations is based on the residual, $R_i(\mathbf{x})$, and is found from either Eq. (7.8) or Eq. (7.14), depending on the boundary conditions. The LHS matrix entries are found using Eqs. (7.11),(7.12), and (7.13), or (7.15).

7.3 Results

The full Newton method described in the previous section is applied to two-dimensional Stokes flow, $Re = 0$, and finite Reynolds number flow, $Re \approx 25$, past a periodic array of circular disks. The properties of the resulting Jacobian matrix are examined. The computational cost of the method is measured and compared against the cost of a standard implementation.

7.3.1 Flow past a periodic array of circular disks

The flow past a periodic array of disks is computed for two Reynolds numbers, specifically $Re = 0$ and $Re \approx 25$. The diameter of the disks is 1/4 times the center to center distance in the rectangular array. Periodic boundary conditions are applied

along each of the boundaries. The flow is driven by an applied forcing. Specifically, the forcing contribution in Eq. (7.8) is given by,

$$F_j = 337.5 \, \frac{\Delta x}{c^2} \, w_{jx}, \tag{7.16}$$

where w_{jx} is the x-component of the vector $\mathbf{w}_j$ and the coefficient 337.5 was empirically chosen such that the resulting Reynolds number is approximately 25. For the Stokes flow case, the same forcing is used, but the non-linear terms in the equilibrium distribution are removed to eliminate all inertial effects, even though the velocity is finite. As shown by Holdych et. al.(5), LBGK convergence is guaranteed if the viscosity, ν, and the relaxation time, τ, are held constant as the mesh is refined. In this study, these parameters are chosen as $\nu = 1$ and $\tau = 0.8$. From Eq. (7.7), we therefore have the relationship that $c = 10/\Delta x$.

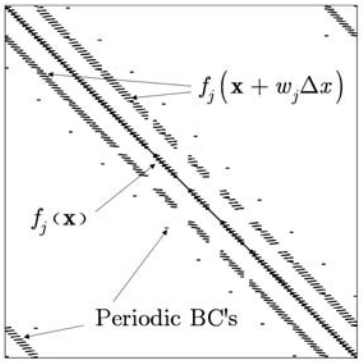

Figure 7.1. The matrix structure for time-steady flow about a periodic array of circular disks with a lattice size of 11x11

7.3.2 Matrix properties

It is interesting to examine the structure of the assembled matrix once the boundary conditions are applied including the bounce-back and periodic conditions. Figure 7.1 shows the matrix structure for a lattice size of 11x11. The figure was generated by MATLAB(6). The matrix clearly has a sparse, banded structure. The diagonal entries are from components of the particle distribution that are collocated with the node. Other near diagonal terms are from the nearest neighbor in the streaming contribution to the equation. Finally, there are some entries that are further off the diagonal that are the result of the periodic boundary conditions. The bounce-back boundary conditions do not significantly alter the structure of the matrix and have a simpler structure than the regular residual equation for internal nodes.

It is unclear, when looking at the structure of the matrix, whether it can be solved using a generic direct solver for sparse, banded matrices. While the overall structure is retained, the periodic BC's introduce significant off-diagonal terms that may not be readily handled by such a solver. In this work MATLAB(6) is used for the full Newton implementation. At each Newton iteration the linear system is assembled in a sparse matrix format. The built-in direct solver is then used to solve for the update to the solution vector. According to the MATLAB(6) documentation, this matrix structure is characterized as banded with low band density. In this case, the built-in solver uses the LAPACK(7) routine DGBTRF for the LU factorization and DGBTRS for the solution step. The performance of this full Newton method with direct linear solver is compared to that of the standard fully explicit LBGK method in the following section.

7.3.3 Performance

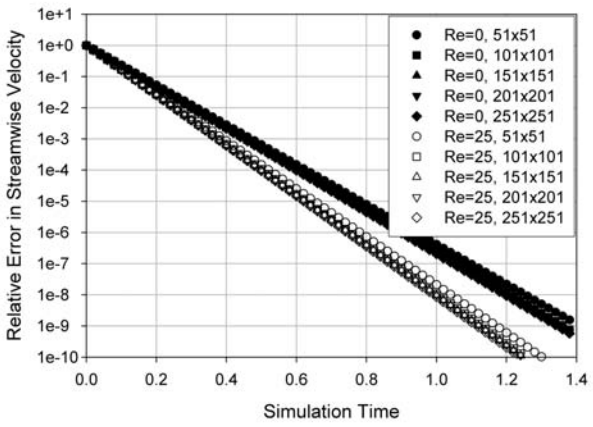

Figure 7.2. Convergence of the standard, fully explicit LBGK method as a function of simulation time for various grid sizes at $Re = 0$ and $Re \approx 25$.

The first step in comparing the proposed full Newton method to the fully explicit method is to establish a common convergence criterion. The fully explicit method is evolved forward in time from an initial state with the particle distribution equal to the equilibrium distribution at zero velocity. Using Eq. (7.7), with the parameters $\nu = 1$ and $\tau = 0.8$, the time step is given by $\Delta t = \Delta x^2/10$. The relative error in the maximum streamwise velocity component is monitored as a function of simulation time, t, and is plotted in Fig. 7.2. The relative error is computed as the relative difference between the evolving maximum velocity and that found at steady-state using the full Newton method. We observe that the relative error decreases nearly linearly with simulation time. The slope is moderately dependent on the Reynolds

number but nearly independent of mesh size. A relative error of approximately 10^{-8} is obtained at $t = 1.2$ for $Re = 0$ and $t = 1.0$ for $Re \approx 25$. It is noted that a simulation time of $t = 1.0$ requires a total number of time steps $NT = 1.0/\Delta t = 10 \times (NX - 1) \times (NY - 1)$ since $\Delta x = 1/(NX - 1)$ and $NX = NY$.

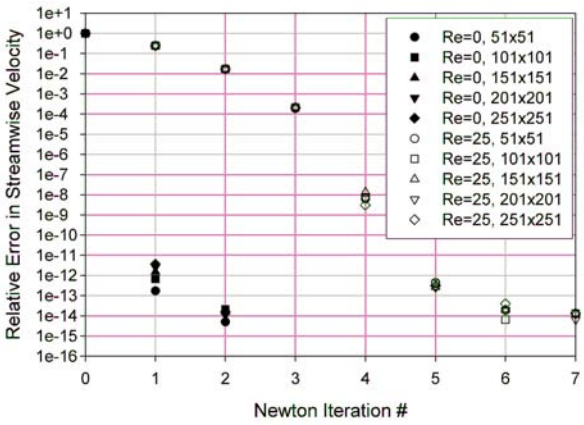

Figure 7.3. Convergence of the full Newton method as a function of Newton iteration for various grid sizes at $Re = 0$ and $Re \approx 25$.

The same level of convergence is sought for the full Newton simulations. Figure 7.3 shows the relative error in the maximum streamwise velocity as a function of Newton iteration. We observe that the relative error for the Stokes flow case is less than 10^{-11} after a single iteration, while an accuracy of approximately 10^{-8} is obtained after four Newton iterations for $Re \approx 25$. Because the Stokes problem is linear, we expected that the fully converged answer would be obtained on the first Newton iteration. We observe, however, a slight improvement of the solution after a second Newton iteration. This may be due to small round-off errors in the direct solver. Nonetheless, a highly accurate solution is obtained using just one Newton iteration.

The cost of obtaining a similar level of accuracy is now compared. Specifically the cpu time needed to obtain an accuracy of approximately 10^{-8} or better is evaluated for both the full Newton and fully explicit methods. Figure 7.4 shows the cpu times for a FORTRAN simulation using the fully explicit LBGK method. The flow was simulated until $t = 1.2$ for $Re = 0$ and $t = 1.0$ for $Re \approx 25$. It is noted that these cpu times correspond to approximately 4.1 million site updates per second using a single processor. Also plotted is the cpu times for the full Newton simulations performed in MATLAB(6). A single iteration is used for $Re = 0$ and four Newton iterations for $Re \approx 25$. The plot is given as a function of problem size, defined as the total number of nodes in the problem, $N = NX \times NY$. Also shown are two reference lines. The solid line on this log-log plot corresponds to N^2, and the dashed line is $N^{1.2}$.

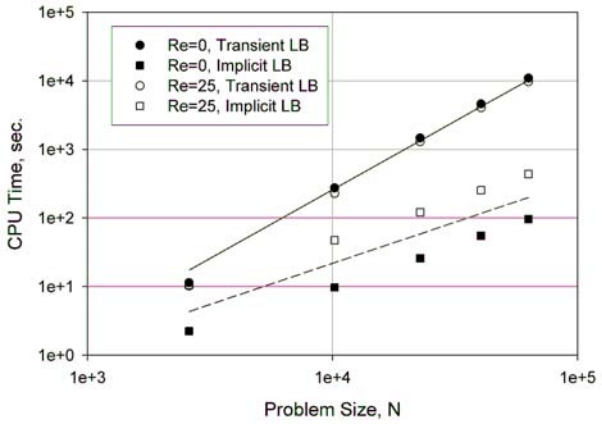

Figure 7.4. CPU cost as a function of problem size for various grid sizes at $Re = 0$ and $Re \approx 25$. The fully explicit simulations were performed until $t = 1.2$ for $Re = 0$ and $t = 1.0$ for $Re \approx 25$, and the full Newton simulations used one and four Newton iterations for $Re = 0$ and $Re \approx 25$, respectively. The solid reference line is N^2, and the dashed line is $N^{1.2}$.

The cost for the fully explicit simulations is nearly independent of Reynolds number. The cpu time scales as N^2. This is expected since the time step shrinks as $1/N$ and the cost of a single time step grows as N. The full Newton method, however, scales super-linearly, with cpu time scaling approximately as $N^{1.2}$. The cost for the case of $Re \approx 25$ is four times that for $Re = 0$ since four Newton iterations are required. The cpu time of the full Newton method is approximately 100 times smaller than that for the fully explicit simulations for the Stokes flow case at the finest resolution (251x251). Even at the coarsest mesh of 51x51 the cost for full Newton method is less than that for the standard fully explicit method, especially for Stokes flow.

7.4 Conclusions

A full Newton method has been developed for the time-steady LBGK equations that is amenable to fast direct solvers. The method has been shown to scale super-linearly with the number of nodes in the problem. Unlike earlier methods that used multigrid solvers, this method appears to be generally applicable to complex geometries with bounce-back boundary conditions. Despite the use of general boundary conditions including periodic conditions, the general purpose direct solver designed for sparse banded matrices showed excellent performance. Future work will examine parallel implementations of full Newton methods for LBGK models.

References

[1] S. Chen and G. D. Doolen, Lattice Boltzmann method for fluid flows, *Ann. Rev. Fluid Mech.*, **30**, 329 (1998). 7.1

[2] J. Tolke, M. Krafczyk, and E. Rank, A multigrid-solver for the discrete Boltzmann equation, *J. Stat. Phys.*, **107**, 107 (2002). 7.1

[3] D.J. Mavriplis, Multigrid solution of the steady-state lattice Boltzmann equation, *Computers & Fluids*, **35**, 793 (2006). 7.1

[4] X. He, and L.S. Luo, Lattice Boltzmann model for the incompressible Navier-Stokes equation, *J. Stat. Phys.*, **88**, 927 (1997). 7.2.1, 7.2.1

[5] D.J. Holdych, D.R Noble, J.G Georgiadis, R.O. Buckius, Truncation error analysis of lattice Boltzmann methods, *J. Comput. Phys.*, **193**, 595 (2004). 7.2.1, 7.3.1

[6] MATLAB version 7.2.0. Natick, Massachusetts: The MathWorks Inc., (2006). 7.3.2, 7.3.3

[7] E. Anderson, Z. Bai, C. Bischof, S. Blackford, J. Demmel, J. Dongarra, J. Du Croz, A. Greenbaum, S. Hammarling, A. McKenney, and D. Sorensen, *LAPACK Users' Guide*, (Society for Industrial and Applied Mathematics, Philadelphia, 1999). 7.3.2

Chapter 8

Embedding Sharp Interfaces within the Lattice Boltzmann Method for Fluids with Arbitrary Density Ratios

8.1 Background

Several lattice Boltzmann (LB) methods(1) have been introduced for non-ideal gases or binary fluids,(2; 3; 4; 5). A limitation of all of these early models, however, is that the density ratio must remain rather small (of order 10 or less) to obtain stable solutions. A number of newer models have been developed that yield stable solution for much larger density ratios (or order 10^3)(6; 7; 8). All current LB models, however, are characterized by a diffuse interface approach in which the the interface has a finite width of 3 or more lattice sites.

Diffuse interfaces may become problematic, however, for a number of flows. Flow through narrow pores becomes difficult to simulate with LB models as the pore width approaches the interface width. This would be true for simulations which have features with resolution comparable to the finite interface width. Also, flows with significant shear stresses may be incorrectly modeled by diffuse interface methods(9), which give rise to nonphysical instabilities. For these types of problems, diffuse interface methods are unable to capture the essential physics of the problem.

In this chapter, we introduce a novel method for implementing sharp interfaces between two fluids in the LB method. The interface does not have a finite width but rather exists as a sharp separation between the fluids. In this initial work, the interface is stationary. This helps in the development of interfacial conditions that preserve accuracy and stability across the sharp interface. An additional feature of this method is that arbitrarily large density ratios may be simulated.

8.2 Methodology

The objective of this work is to simulate two fluids of arbitrary density that are separated by an interface. It is assumed that the interface location is exactly known and has infinitesimal width. On the LB lattice, the interface will be located, in general, between pairs of nodes. The algorithm must be able to translate the information stored in the distribution functions as it is passed across the interface. We have studied two different methods that handle these challenges.

8.2.1 Moment method

As the particle distribution leaves one fluid, crosses the interface, and enters a fluid with very different properties, it must be transformed to match the material it is entering. This is complicated by the fact that the particle distribution is difficult to interpret physically. It contains a great deal of information including the density, momentum, and gradients of these quantities. This is the motivation for pursuing a method based on the moments of the distribution rather than the distribution itself. Physical insight can provide boundary conditions at the interface for the moments since these can be more easily related to the macroscopic variables.. The complete set of moments for distribution functions is described by Lallemand and Luo (10). The jump in some of these moments across the interface is obvious, including density and momentum. However, analytical investigation is required to better understand jumps in the higher order moments.

Jumps in distribution functions may be defined by comparing the values on either side of the interface. We compare the value in the receiving fluid to the post collision value of the sending fluid. For a distribution function f_j, the jump is defined by

$$\Delta f_j = f_j(x + \vec{w_{j,x}}\Delta x, y + \vec{w_{j,y}}\Delta x) - f_j^s(x, y) \ , \tag{8.1}$$

where $\vec{w_{j,\alpha}}$ is the α component of the normalized velocity vector that corresponds to the f_j direction. The superscript 's' denotes a post-collision value, given by

$$f_j^s(x, y) = f_j(x, y) - \frac{1}{\tau}(f_j(x, y) - f_j^{eq}(x, y)) \ . \tag{8.2}$$

For the D2Q9 grid, there are nine linearly independent moments, m_i. The jump for each moment is defined similarly to jumps in distribution functions

$$\Delta m_i = m_i(x + \vec{w_{j,x}}\Delta x, y + \vec{w_{j,y}}\Delta x) - m_i^s(x, y) \ , \tag{8.3}$$

where the post-collision moments are determined using the post-collision distribution functions.

To study the feasibility of this approach, the solution from an exact solution is employed to evaluate the moments. The exact moments are obtained by inserting the analytical solution for the distribution function for steady Poiseuille flow into the transformation equation, $\vec{m} = M\vec{f}$, where $\vec{m}$ and $\vec{f}$ are the column vectors containing the moments and distribution functions, respectively, and M is the transformation matrix. Streamed moments are obtained in the same way, $\vec{m^s} = M\vec{f^s}$, where Equation 8.2 is applied to the analytical expression for the distribution function to get $\vec{f^s}$. The interface between the two fluids is parallel to the walls and fixed at y_{int}, which is between nodes located at $y1$ and $y2$, with $y2 = y1 + \Delta x$. The densities are ρ_1 and ρ_2 below and above the interface, respectively. The velocity is C0 continuous across the interface, and the velocity gradient at the interface is specified by $\mu_1 u'(y_{int,-}) = \mu_2 u'(y_{int,+})$, where μ_1 and μ_2 are the dynamic viscosities of fluids 1 and 2, respectively, and the prime denotes differentiation in the y-direction. The values for all nine moment jumps from the node at y1 to the node at y2 are given below.

$$\Delta m_1 = -\rho_1 + \rho_2 \tag{8.4}$$

$$\begin{aligned}\Delta m_2 = &-\rho_1(3\,u(y1)^2 - 2c^2) + \rho_2(3\,u(y2)^2 - 2c^2) + \\ &\Delta x^2(-\rho_1(2\tau^2 - 3\tau + 1)(u'(y1)^2 + u(y1)\,u''(y1)) + \\ &\quad \rho_2(2\tau^2 - \tau)(u'(y2)^2 + u(y2)\,u''(y2)) + O(\Delta x^4)\end{aligned} \tag{8.5}$$

$$\begin{aligned}\Delta m_3 = &\,c^2(\rho_1(3\,u(y1)^2 - 2c^2) - \rho_2(3\,u(y2)^2 - 2c^2)) + \\ &\Delta x^2 c^2(-\rho_1(2\tau^2 - 3\tau + 1)(u'(y1)^2 + u(y1)\,u''(y1)) + \\ &\quad \rho_2(2\tau^2 - \tau)(u'(y2)^2 + u(y2)\,u''(y2)) + O(\Delta x^4)\end{aligned} \tag{8.6}$$

$$\begin{aligned}\Delta m_4 = &-\rho_1\,u(y1) + \rho_2\,u(y2) + 6c\,e2\tau(-F_1 + F_2) + \\ &\frac{\Delta x^2}{6}(-\rho_1(2\tau^2 - 3\tau + 1)\,u''(y1) + \rho_2(2\tau^2 - \tau)u''(y2)\end{aligned} \tag{8.7}$$

$$\begin{aligned}\Delta m_5 = &\,c^2(\rho_1\,u(y1) - \rho_2\,u(y2)) + \\ &\Delta x^2\frac{c^2}{6}(-\rho_1(2\tau^2 - 3\tau + 1)\,u''(y1) + \rho_2(2\tau^2 - \tau)u''(y2)\end{aligned} \tag{8.8}$$

$$\Delta m_6 = 0 \tag{8.9}$$

$$\Delta m_7 = 2\Delta x\, c(\rho_1(\tau-1)u(y1)\,u'(y1) - \rho_2\tau\, u(y2)\,u'(y2) + O(\Delta x^3) \tag{8.10}$$

$$\begin{aligned}\Delta m_8 = &-\rho_1\, u(y1)^2 + \rho_2\, u(y2)^2 + \\ &\frac{\Delta x^2}{3}(-\rho_1(2\tau^2-3\tau+1)(u'(y1)^2 + u''(y1)\,u(y1)) + \\ &\quad \rho_2(2\tau^2-\tau)(u'(y2)^2 + u(y2)\,u''(y2)) + O(\Delta x^4)\end{aligned} \tag{8.11}$$

$$\Delta m_9 = \Delta x\frac{c}{3}(\rho_1(\tau-1)u'(y1) - \rho_2\tau u'(y2)) \tag{8.12}$$

In the above equations, F is the body force for the respective fluids. For jumps in the opposite direction, the sign for each density is reversed and the polynomials of τ multiplying ρ_1 and ρ_2 are swapped in each jump. To apply these jumps, the velocity and its gradients at nodes on either side of the interface must be specified.

The above jumps in moments are established in terms of the density, velocity, and velocity gradients. The generality of these expressions is unknown, however, since they were derived for the specific case of steady Poiseuille flow. Once the jumps are evaluated, the unknown incoming component of the distribution function, $f_j(x + \vec{w_{j,x}}\Delta x, y + \vec{w_{j,y}}\Delta x)$, can be found using Equation 8.1 and the inverse of the transformation matrix:

$$f_j(x + \vec{w_{j,x}}\Delta x, y + \vec{w_{j,y}}\Delta x, t + \Delta t) = M_j^{-1}\vec{\Delta m} + f_j^s(x, y, t)\ , \tag{8.13}$$

where M_j^{-1} is the jth row of the inverse transformation matrix and $\vec{\Delta m}$ is the vector consisting of the jumps of the moments. The complete time stepping algorithm for the moment method is then as follows:

1. Collide
2. Stream
3. Calculate moments
4. Solve for distribution functions that cross the interface using Equations 8.4 - 8.12, 8.13

The moment method as derived here may be limited in its validity since the moment jumps are derived for a steady, unidirectional flow. There is no information about how time derivatives are transformed across the interface. Also no consideration is given to the velocity normal to the interface or gradients along the flow direction which are zero for this idealized flow. There is no obvious way to include these additional time and space gradients into the jumps without verifying them against analytical distribution functions. This is not possible in general since there are no known transient, fully two dimensional flows for which analytical distribution functions may be derived.

8.2.2 Expansion method

The expansion method is a more direct way to transform the values of distribution functions as they cross the interface. As an example, consider a steady two-dimensional flow with a horizontal interface parallel to the flow direction, with fluid 1 and fluid 2 below and above the interface, respectively. The distribution function f_2 at the first node below the interface must stream across the interface. The density and velocity gradients associated with f_2 are those of fluid 1, however, so this value cannot be streamed directly. The expansion method uses truncated expressions for the distribution function in terms of the equilibrium distribution and its gradients to send a corrected distribution function across the interface.

The expansion method uses the distribution function expansions derived by Holdych et al. (11) based on equilibrium distribution functions. In their work the distribution function is expressed as

$$f_j(\mathbf{x},t) = f_j^{eq}(\mathbf{x},t) + \tau \sum_{m=1}^{\infty} \frac{p[\tau;m]}{m!} [\Delta t \partial_t + \Delta x \mathbf{w}_j \cdot \nabla]^m f_j^{eq}(\mathbf{x},\mathbf{t}) \ , \tag{8.14}$$

where the first three terms of the parameterized function $p[\tau;m]$ are given by

$$p[\tau;1] = -1, p[\tau;2] = 2\tau - 1, p[\tau;3] = -6\tau^2 + 6\tau - 1 \ . \tag{8.15}$$

The equilibrium distribution functions are given by

$$f_j^{eq}(\mathbf{x},t) = w_\alpha \rho [1 + 3(\mathbf{e_j} \cdot \mathbf{u}) + \frac{9}{2}(\mathbf{e_j} \cdot \mathbf{u})^2 - \frac{3}{2}\mathbf{u}^2] \ . \tag{8.16}$$

By truncating Equation 8.14 to a fixed number of terms, the values of distribution functions that cross the interface can be obtained with a known order of error.

The expansion method obtains values for the unknown distribution functions in two steps. The first step scales the distribution functions by the density ratio of the target fluid to the source fluid. Because the approximate expansions are linear functions of the density, this step establishes the correct density for the distribution function. The

second step substitutes the correct velocity and velocity gradients into the approximated distribution functions. However, since the velocity and its gradients are not known, additional approximations are required, which are discussed in Section 8.2.3.

Returning to the example at the beginning of this section, the distribution function f_2 can be approximated by Equation 8.14. To order Δx, the distribution function can be approximated by

$$f_2 = \rho(\frac{1}{9} + \frac{1}{3c}v - \frac{3}{c^2}(u^2 + 2v^2) + \\ \Delta x \frac{\tau}{3c^2}(uu_y - (c + 2v)v_y) + O(\Delta x^2) \ , \tag{8.17}$$

where velocity and density are defined at the node in fluid 2. Further assuming that $v = 0$, the rescaling and substitution has the form

$$f_2^{em} \approx f_2 \frac{\rho_2}{\rho_1} + \\ -\frac{\rho_2}{6c^2}(u^2 - (u^*)^2) + \Delta x \rho_2 \frac{\tau}{3c^2}(uu_y - u^* u_y^*) \ , \tag{8.18}$$

where f_2^{em} refers to the approximate distribution function, f_2 is the streamed distribution function from below the interface, the starred velocity and velocity gradients refer approximated values from the source node, and the other velocity and velocity gradients refer to the approximated values at target nodes. The first line rescales the density, and the second line replaces the 'incorrect' velocities with 'correct' values. For simulations in this work, only replacements of up to first order in Δx have been attempted and time derivatives have been neglected. The higher order terms of the expansion are not adjusted and therefore would correspond to the higher order velocity gradients and time derivatives from the source fluid.

The time stepping algorithm for the expansion method is as follows:
1. collide
2. stream
3. calculate moments
4. solve for distribution functions that cross the interface (Equation 8.18) and determine moments

8.2.3 Estimating the unknown velocity profile

Whether the moment method or expansion method is used, there are multiple interfacial quantities that are needed to evaluate the transformation. The moment method requires the velocity and density values at the interface along with the velocity gradients to evaluate the moment jumps. Similarly these quantities are needed to evaluate the terms in the particle distribution expansions in the expansion method.

To obtain the needed quantities, a velocity and density profile is assumed in the vicinity of the interface. The density is assumed to be nearly constant on each side of the interface (with a sharp jump at the interface). For the velocity, an estimate is needed for the nodes on either side of the interface, and a velocity profile is assumed in order to estimate the velocity gradients.

The approximate velocity parallel to the interface from $f_1 - f_3$ is estimated from

$$u_{est} = \frac{3\,c}{2\,\rho}(f_1 - f_3)\ , \tag{8.19}$$

where values of f_1 and f_3 are known. The first moment of the approximate distribution functions was used by Holdych et al. (11) to derive the momentum equations. To second order, the momentum equations have the form

$$\frac{1}{\rho}\sum_j f_j e_{j,x} = u + \Delta t(-(u^2)_x - (uv)_y + \nu(3u_{xx} + u_{yy} + 2v_{xy})) + O(\Delta t^2)\ . \tag{8.20}$$

Using the estimate from Equation 8.19, the momentum equation has the form

$$(f_1 - f_3)\frac{3c}{2\rho} = u + \Delta t(-(u^2)_x + \frac{1}{2}(v^2)_x + 3\nu u_x x)\ . \tag{8.21}$$

The error in velocity obtained from Equation 8.19 is given by

$$u - u_{est} = \Delta t(-(uv)_y - \frac{1}{2}(v^2)_x - \nu(u_{yy} + 2v_{xy})) + O(\Delta t^2)\ . \tag{8.22}$$

When the velocity perpendicular to the interface is zero (v=0), the error is simplified to $\Delta t\nu u_{yy}$. For the flows simulated in this work, the estimate of velocity from Equation 8.19 are very good. The error is on the order of 0.1% for Poiseuille-Couette flow simulations.

Additional assumptions are needed to determine gradients of the velocity field at the interface. A useful approach is to assume linear velocity profile near the interface and specify that the gradient has a jump given by the jump in dynamic viscosity. This method allows us to apply macroscale jumps in fluid properties such as viscosity explicitly. Alternatively, the velocity profile can be assumed to be parabolic with a jump in velocity gradient at the interface. See Figure 8.1 to see the linear approximation. The values of u^* and u_y^* in Equation 8.18 are determined by extrapolating the fitted curves to the node on the other side of the interface. The extrapolations are the dashed part of the lines in Figure 8.1. These methods are used in the following section, and the effect on the accuracy is assessed.

8.3 Results

Both of the methods are tested using Poiseuille-Couette flow between walls at y=0 and y=1 cm, with an interface located at y=0.635 cm. The upper wall moves with

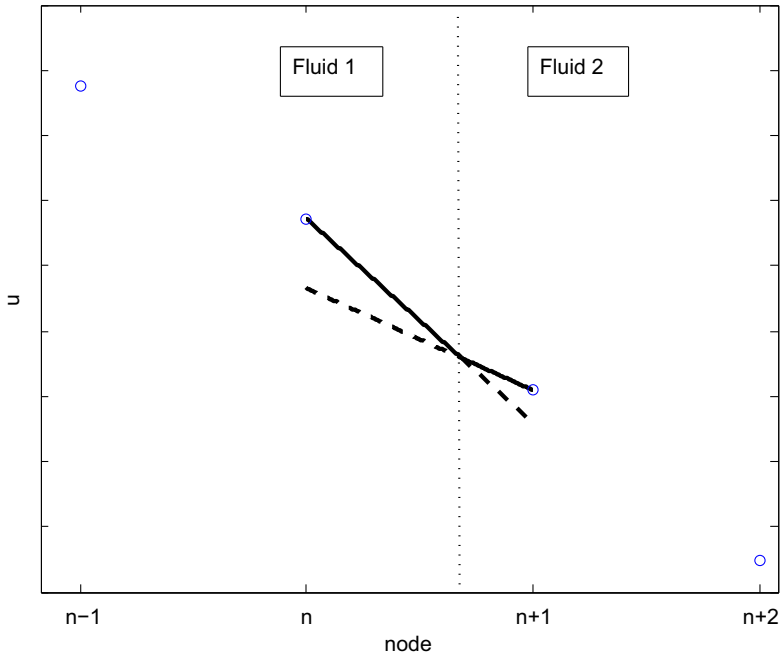

Figure 8.1. Linear approximation for estimating velocity gradients near the interface. Velocities at nodes n and n+1 are estimated from Equation 8.19. Linear velocity profiles are assumed between nodes n and the interface (dotted vertical line) and the interface and node n+1, with a jump in slope given by the dynamic viscosity ratio (equal to 2 for this case).

velocity = 0.05 cm/s and the body force driving the flow is -0.1 g/(cm^2 s^2). Kinematic viscosities of both fluids is 0.1 cm^2/s. The density of the fluid below the interface is 1 g/cm^3, and the upper fluid density is 100 g/cm^3. At the walls, the consistent hydrodynamic boundary condition is applied (12), and periodic conditions are imposed in the flow direction. Initially, the fluid velocity is set to zero. The relative error is given by

$$E1 = \frac{\sum_{x,y} |u - \hat{u}|}{\sum_{x,y} |\hat{u}|} + \frac{\sum_{x,y} |v - \hat{v}|}{\sum_{x,y} |\hat{v}|} \,, \tag{8.23}$$

where $\hat{u}$ and $\hat{v}$ are the analytical values of the velocity field.

8.3.1 Moment Method

The velocity field from the moment method at nodes on either side of the interface for the default case are shown in Figure 8.2. Good agreement is achieved for the velocity field, and the density jump is maintained. The accuracy of simulations appear to

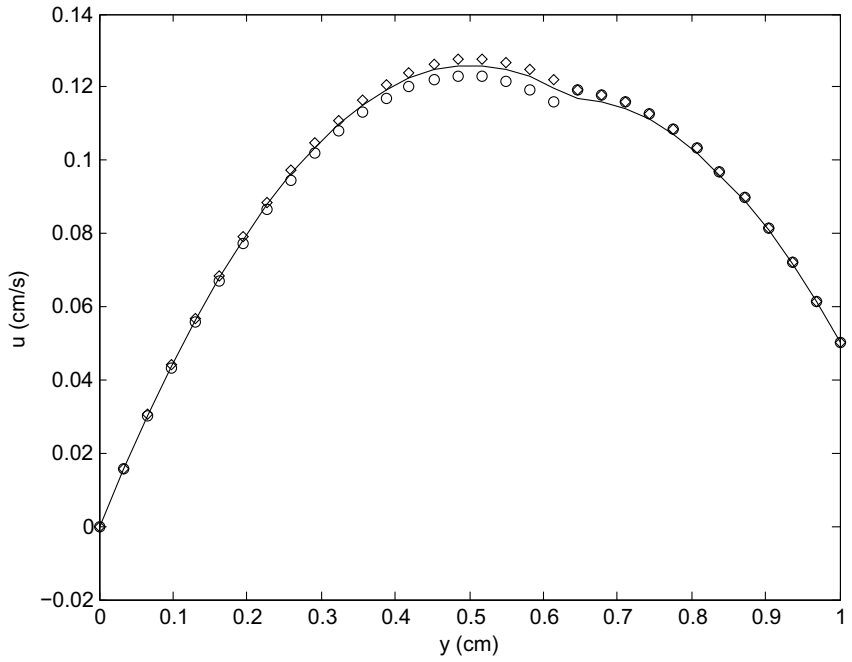

Figure 8.2. Velocity profile for default case using the moment method with jumps defined by nodes on either side of the interface (circles) and expansion method with linear velocity interpolation (diamonds) compared to analytical solution (line).

converge linearly with grid refinement for fixed relative position of the interface (θ), as Figure 8.3 shows. The relative distance is defined by

$$\theta = \frac{y_{int} - y1}{\Delta x} \ , \tag{8.24}$$

where y1 is the location of the node nearest the interface from below.

8.3.2 Expansion Method

The expansion method achieves good agreement with the analytical solution, as Figure 8.2 shows. The method is able to maintain both density and velocity gradient jumps across the interface.

The expansion method converges linearly with grid spacing as Figure 8.3 shows. The data indicates that convergence is linear for a fixed values of θ. For Poiseuille-Couette flow, the parabolic interpolation achieves better agreement than linear interpolation. However, for more general flows, linear interpolation may be a better choice due to its

simplicity. The order of accuracy of the two methods is the same. Obtaining second order accuracy may require using additional terms in the expansion. This will be examined in future work.

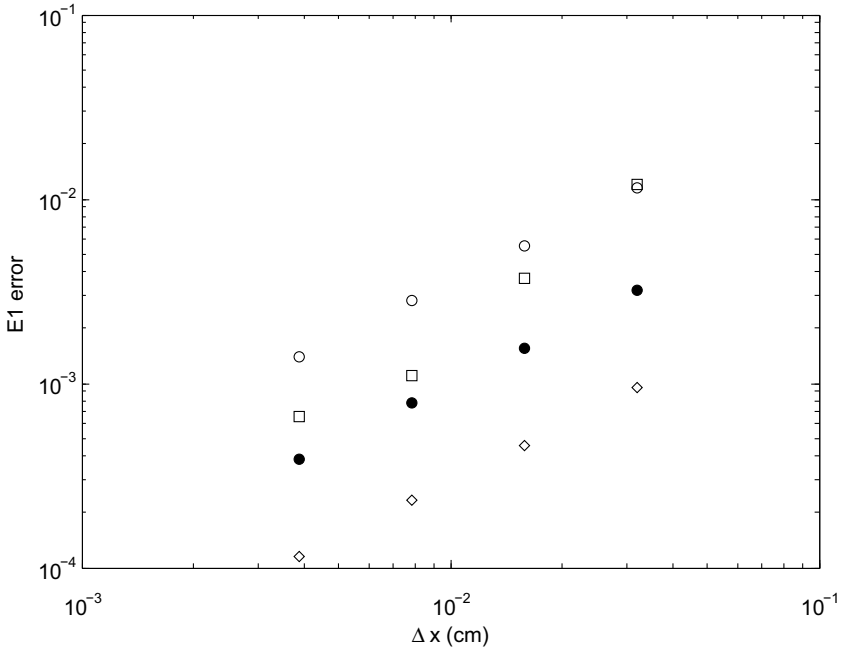

Figure 8.3. Error convergence for the default case with grid spacing for moment method using linear interpolation (squares), the expansion method using linear (circles), and parabolic (diamonds) interpolation. Open symbols indicate $\theta = 0.685$ and filled symbols indicate $\theta = 0.45$. For both methods, the convergence appears to be linear.

Figure 8.4 shows that the errors also depend on the location of the interface between the nodes. A minimum error is achieved when the interface is exactly in the middle between the two nodes. When the interface gets close to the node associated with the less dense fluid, the algorithm becomes unstable. For density ratio equal to 100, for values of θ less that 0.084, the algorithm is unstable. This will be investigated in a future work.

The algorithm is robust for a wide range of parameter space. For Poiseuille-Couette flows, the E1 error is independent of the value of τ. Also, the density ratio of the two fluids has only a small effect on E1 error. For density ratio approaching unity, the value of E1 goes to numerical precision. Values of E1 change by less than 2% for density ratios ranging from 100 to 10^9. This shows that the method is applicable to problems with arbitrarily high density ratios.

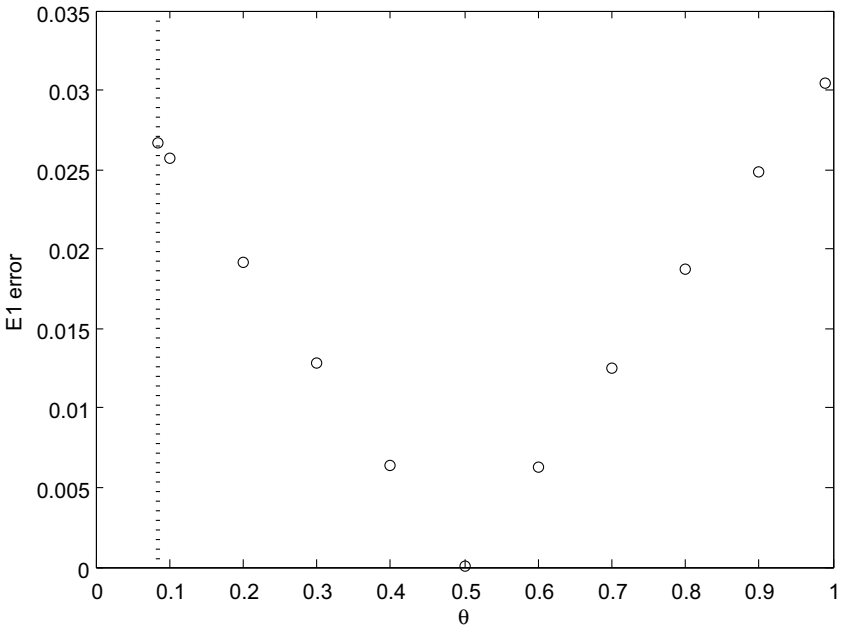

Figure 8.4. Errors for the default case using the expansion method with linear interpolation as a function of location of the interface, θ. For $\theta < 0.084$ simulations become unstable.

The expansion method gives good results even with nonzero velocity gradients parallel to the interface. Figure 8.5 shows the velocity field obtained from a simulation of flow around a cylinder. The interface between two fluids with density ratio equal to 100 corresponds to the centerline along the x-direction of the cylinder. Periodic boundary conditions are imposed along the external boundaries, and an external body force is used to drive the flow. Bounce back conditions were employed for the walls of the cylinder. Values for distribution functions that cross the interface are solved by the expansion method. There is no jump in shear stress across the interface because of the symmetry of the flow. More complex flows will be the topic of a future work.

8.4 Conclusions

Sharp interface techniques have been developed for the LB method, avoiding the interfacial smearing that occurs in traditional, finite width LB models. These techniques are shown to be stable for arbitrarily high density ratios. Two techniques for imposing the interfacial discontinuities are explored, the moment method and the expansion method. Both techniques capture the density jump and the discontinous velocity gradient that results from the jump in dynamic viscosity.

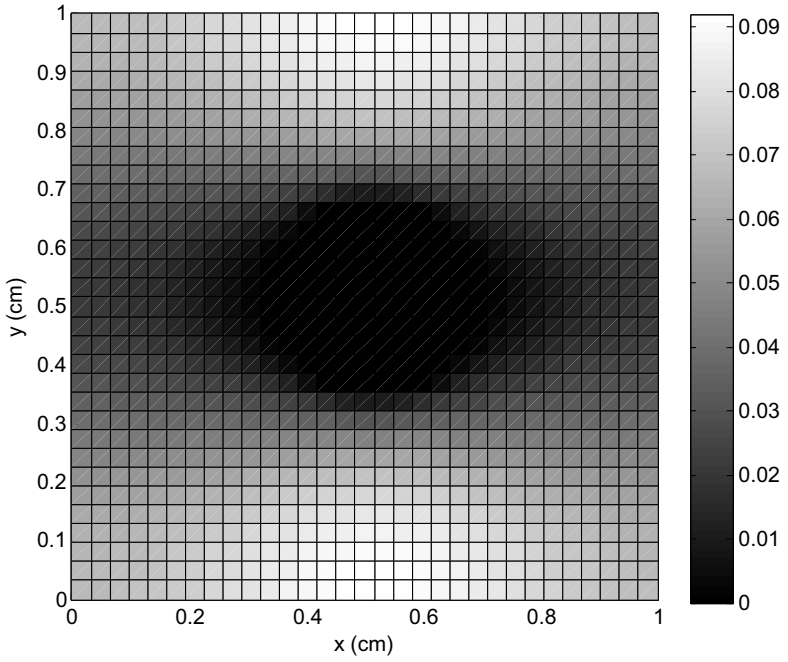

Figure 8.5. Velocity (cm/s) along the direction of flow (x-direction) for flow around a cylinder using the expansion method with interface along the centerline of the cylinder. Density ratio is equal to 100.

Future work will focus on developing the generality of the algorithm so that more complex flows may be simulated. For simulations in this work, the velocity perpendicular to the interface is identically equal to zero. For nonzero velocities perpendicular to the interface more care must be taken in the expansions of the distribution functions. This also implies that the boundary is moving, which will require a coupling between the LB method and a level set routine.

Another future development is to simulate more complex shapes of interfaces. For curved interfaces, more than 3 distribution functions may be streamed across the interface. Thus, approximating the local velocity with Equation 8.19 is not possible. More sophisticated algorithms must be developed to obtain sufficient equations to determine all of the unknowns. In addition, the order of accuracy and stability of the method will be explored further.

References

[1] Chen S. and G.D. Doolen, Rev. Fluid Mech., **30**, (1998) 329-364 8.1

[2] Gunstensen, A.K., D.H. Rothman, S. Zaleski, G. Zanetti, Phys. Rev. A, **43**, (1991) 4320-4327 8.1

[3] Shan, X. and H. Chen, Phys. Rev. E, **47** (1993) 1815-1819 8.1

[4] Swift, M.R., W.R. Osborn, J.M. Yeomans, Phys. Rev. Lett., **75** (1995) 830-833 8.1

[5] He, X., S. Chen, R. Zhang, J. Comp. Phys., **152**, (1999) 642-663 8.1

[6] Inamuro, T. and C-L Lin, J. Comp. Phys., **198**, (2004) 628-644 8.1

[7] Lee, T. and T. Ogata, S. Tajima, N. Konishi, J. Comp. Phys., **206**, (2005) 16-47 8.1

[8] Zheng, H.W., C. Shu, Y.T. Chew, J. Comp. Phys., **218**, (2006) 353-371 8.1

[9] Sushchikh, S.Yu., R.R. Nourgaliev, T.G. Theofanous, Int. J. of Multiphase Flow, (2007), submitted 8.1

[10] Lallemand, P. and L.S. Luo, Phys. Rev. E **61** (2000) 6546-6562 8.2.1

[11] Holdych, D.J., D.R. Noble, J.G. Georgiadis, R.O. Buckius, J. Comp. Phys., **193**, (2004) 595-619 8.2.2, 8.2.3

[12] Noble, D.R., S. Chen, J.G. Georgiadis, R.O. Buckius, Physics of Fluids, **7** (1995) 203-209. 8.3

9. SUMMARY AND CONCLUSIONS

This report contains the results from a 3 year LDRD project entitled "Interface Physics in Microporous Media". The project makes specific advances in the areas of micromodel fabrication, in-situ visualization of multiphase flows in micromodels, and in the lattice Boltzmann and finite element modeling of multiphase flows in microporous geometries. A summary of these accomplishments is given in the introduction. More details are given in each area in the subsequent chapters.

The experimental discoveries in this work, combined with algorithm development, significantly advance our ability to model interfacial physics in microporous media. This will enable us to provide critical help to our customers in areas ranging from energy with applications in enhanced oil recovery and fuel cell development, to water resources requiring advanced filtration technology, and to weapons systems in need of reliable encapsulation techniques for weapons components.

Future work in the area of finite element simulations for micro-capillarity will focus on sharp interface methods. An ESRF project is examining Conformal Decomposition Finite Element Methods (CDFEM) that seek to use the best features of Arbitrary Lagrangian Eulerian (ALE) methods and interface capturing methods including level set methods. These approaches are needed when the interface physics are the controlling phenomena.

Future work on experiments and modeling of micro-capillary flow could examine a variety of things. To improve time resolution beyond 2 frames per second, a standard fluorescence microscope (not a confocal) could be used. This would do a better job at capturing the rapid phenomena we observed, such as the Haines jumps, and provide additional data for comparing to simulation results. Alternate flow geometries, such as making modifications to the diameter, spacing, and orientation in the 4-post geometry or examining geometries from previous macro-scale work like notches, would increase the library of experimental results for model comparison. Furthermore, changes in material properties by applying surface coatings and/or addition of surfactants as well as different immiscible fluid-fluid pairs could be used to change the interfacial tension and viscosities in the experiment. Pressure measurements of the liquid could also be made to monitor fluctuations in the meniscus shape as the liquid is pumped through the micromodels.

The analysis performed in this project has suggested an interesting area to study in the future. Wetting in a microchannel could potentially be used as a means to measure Blake wetting parameters. As the liquid front progresses through a channel, the flow resistance from viscous flow behind the advancing front increases, slowing the advance of the liquid front. A range of wetting velocities could be captured and the contact angle could be determined from images of the advancing interface. This will be examined in future work.

DISTRIBUTION

1 Laura Pyrak-Nolte
Purdue University
Department of Physics
525 Northwestern Avenue
West Lafayette, Indiana 47907-2036 USA

1	MS0346	Carlton F. Brooks	1513
1	MS0346	Lisa A. Mondy	1514
1	MS0382	David R. Noble	1514
1	MS0734	Melissa A. Yaklin	6338
1	MS0751	Alicia R. Aragon	6315
1	MS0836	Chad E. Knutson	1514
1	MS0836	Terry L. Aselage	1514
2	MS0836	Ken S. Chen	1516
1	MS0346	Anne M. Grillet	1513
1	MS0346	Chris J. Bourdon	1513
1	MS0346	Dan J. Rader	1513

1	MS0899	Technical Library	9536
1	MS0123	D. Chavez, LDRD Office	1011


Sandia National Laboratories